OPERATIONAL EXPLOITATION OF SATELLITE-BASED SOUNDING DATA AND NUMERICAL WEATHER PREDICTION MODELS FOR DIRECTED ENERGY APPLICATIONS

DISSERTATION

David C. Meier, Lieutenant Colonel, USAF

AFIT-ENP-DS-15-D-009

DEPARTMENT OF THE AIR FORCE
AIR UNIVERSITY

AIR FORCE INSTITUTE OF TECHNOLOGY

Wright-Patterson Air Force Base, Ohio

AFIT-ENP-DS-15-D-009

OPERATIONAL EXPLOITATION OF SATELLITE-BASED SOUNDING DATA AND NUMERICAL WEATHER PREDICTION MODELS FOR DIRECTED ENERGY APPLICATIONS

DISSERTATION

Presented to the Faculty

Department of Engineering Physics

Graduate School of Engineering and Management

Air Force Institute of Technology

Air University

Air Education and Training Command

In Partial Fulfillment of the Requirements for the

Doctor of Philosophy in Applied Physics

David C. Meier, M.S.

Lieutenant Colonel, USAF

December 2015

AFIT-ENP-DS-15-D-009

OPERATIONAL EXPLOITATION OF SATELLITE-BASED SOUNDING DATA AND NUMERICAL WEATHER PREDICTION MODELS FOR DIRECTED ENERGY APPLICATIONS

David C. Meier, M.S.

Lieutenant Colonel, USAF

Committee Membership:

Steven T. Fiorino, Ph.D.
Chairman

Lt Col Robert S. Wacker, Ph.D.
Member

Maj Milo W. Hyde, Ph.D.
Member

Matthew R. Whiteley, Ph.D.
Member

ADEDEJI B. BADIRU, Ph.D.
Dean, Graduate School of Engineering and Management

Abstract

The wealth of available scientific data collected by the modern constellation of meteorological satellites can be exploited in new and innovative ways, with direct benefit to directed energy applications. The Atmospheric Infrared Sounder (AIRS) provides accurate, geolocated temperature data for 100 vertical levels, with near global coverage twice daily. AIRS temperature data are used as the starting point for the derivation of atmospheric parameters critical to prediction of sensor or directed energy system performance. The accuracy and utility of the atmospheric characterization can be improved by combining the data from multiple sources. Twenty-four hour data coverage is achieved by extending the atmospheric characterization between satellite observations using Numerical Weather Prediction (NWP) models. A technique is developed to derive wind profiles using AIRS temperature data and the accuracy of these winds is evaluated. These winds are not found to be as accurate as the winds available from modern NWP models, but their usefulness is demonstrated for the stratosphere and lower mesosphere where NWP model data are not readily available. Techniques to derive optical turbulence strength, as modeled by index of the refraction structure function C_n^2, are applied to integrated meteorological satellite data and NWP data. The existing technique, which bases the derivation of C_n^2 for optical wavelengths on vertical atmospheric temperature gradients, is improved by including additional wind shear components and local pressure gradient deviations from the traditionally assumed hydrostatic balance.

Acknowledgments

I would like to sincerely thank my research advisor Dr. Steven Fiorino for his steady guidance and assistance throughout my research and for making the process enjoyable. In addition, I would like to express my gratitude to my research committee members, Lt Col Robert Wacker, Maj Milo Hyde, and Dr. Matthew Whiteley, for making themselves available to share their expertise and provide the advice that helped keep the research on track.

I am thankful for the constant support from all of my family, but am especially grateful to my wife for her patience, understanding, and encouragement during this academic journey.

Table of Contents

Page

List of Figures

Page

List of Tables

Page

List of Acronyms

Acronym	*Definition*
AIRS	Atmospheric Infrared Sounder
AMSU	Advanced Microwave Sounding Unit
CALIPSO	Cloud-Aerosol LIDAR and Infrared Pathfinder Satellite Observations
CLEAR	Critical Laser Enhancing Atmospheric Research
DAAC	Distributed Active Archive Center
ECMWF	European Centre for Medium-Range Weather Forecasts
EDOS	EOS Data and Operations System
EOS	Earth Observing System
ERA	ECMWF Re-Analysis
GES-DISC	Goddard Earth Sciences Data and Information Service Center
GFS	Global Forecast System
GOES	Geostationary Operational Environmental Satellites
HEL	High Energy Laser
HRRR	High Resolution Rapid Refresh
H-V 5/7	Hufnagel-Valley 5/7
HSB	Humidity Sounder for Brazil
IR	Infrared
JPL	Jet Propulsion Lab
LEEDR	Laser Environmental Effects Definition and Reference
LIDAR	Light Detection and Ranging
MODIS	Moderate Resolution Imaging Spectroradiometer

NASA	National Aeronautics and Space Administration
NOAA	National Oceanic and Atmospheric Administration
NOMADS	NOAA Operational Model Archive and Distribution System
NWP	Numerical Weather Prediction
PMRF	Pacific Missile Range Facility
RAOB	Rawinsonde Observation
RMS	Root-Mean-Square
ROBIN	Rocket Balloon Instrument
TDRSS	Tracking and Data Relay Satellite System
TKE	Turbulent Kinetic Energy
UTC	Universal Time Coordinated
WRF	Weather Research and Forecasting

OPERATIONAL EXPLOITATION OF SATELLITE-BASED SOUNDING DATA AND NUMERICAL WEATHER PREDICTION MODELS FOR DIRECTED ENERGY APPLICATIONS

1 Introduction

The performance of directed energy and imaging systems is affected by the state of the atmosphere over the path of interest. Temperature gradients, optical turbulence, and the presence of aerosols and clouds all have significant impact, but these quantities can be difficult to accurately measure or predict over extended paths through the atmosphere. This research examines the availability, resolution, and accuracy of data collected by several satellite-based sounding instruments, and analyzes their applicability to new atmospheric characterization methods that will benefit the directed energy community. The advantages of combining satellite-based sounding data with the output from modern Numerical Weather Prediction (NWP) models is detailed and innovative techniques to improve the methods used to derive the strength of atmospheric optical turbulence are developed.

1.1 Motivation for this Research

Optical turbulence distorts and spreads electromagnetic (primarily in the visible and near-IR) radiation propagating through the atmosphere, and the ability to characterize the strength of the optical turbulence along a specified slant-range path using data from recent satellite measurements would have both civilian and military operational value. In order to accurately predict the effect that the atmosphere will have on a sensor or directed energy system, it is necessary to be able to characterize the path-weighted strength of the optical turbulence and describe the properties of any clouds or aerosols along the path. When designing directed energy systems and predicting atmospheric effects, the common

approach is to make assumptions about the state of the atmosphere, applying a simple atmospheric model or long-term average values. This can lead to unrealistic expectations about how a particular directed energy system would perform, or a lack of appreciation for the variability of performance as atmospheric conditions change.

Atmospheric turbulence can be measured using a thermosonde, but this method has limited usefulness for directed energy applications. The thermosonde measures a profile above a single geographic location, which does not provide the information needed to characterize an extended slant-range path from platform to target. A scintillometer can measure optical turbulence along a path, but it also has limited utility for long-range directed energy applications. Two large drawbacks to operational use of a scintillometer for directed energy applications are the requirement to have equipment at both ends of the path, and the possibility that for a long path with strong turbulence, saturation of the scintillometer makes accurate measurement impossible.

There is a wealth of space-based atmospheric data that can be used to derive the required atmospheric characterization. The continuous stream of data collection by dozens of scientific instruments provides the basis for both improvements in our atmospheric models and derivation of specific parameters of interest. Starting with satellite-measured temperature data, it is possible to derive 3-D fields of winds, gradient Richardson numbers, and optical turbulence strengths, as characterized by the index of refraction structure function, C_n^2.

The focus of this research is to analyze data collected by various scientific instruments in operation on meteorological satellites and to develop and evaluate techniques to take full advantage of the data these instruments can provide, and show

innovative ways the data from different sources can be combined to achieve operationally useful atmospheric characterization. The types of space-based instruments studied include IR and microwave sounders, visible/IR imagers, and LIDAR (Light Detection and Ranging) units. The primary objective is to demonstrate the ability to create operationally relevant, near real-time, 3-D gridded data sets of atmospheric turbulence and cloud characterizations, derived from satellite observations and NWP models.

1.2 Document Structure

This document is organized into five main chapters. This first chapter provides an introduction to the research goals and the motivation for the project, along with a general description of the operational capabilities that this effort enables. The second chapter details the background scientific basis for the techniques employed and includes a survey of the satellite instruments and data sources investigated. The relative strengths and weaknesses of the data provided by the individual instruments and weather models are discussed, as is the role each data source can play in the combined atmospheric characterization techniques. This discussion is followed by a review of the topic of atmospheric turbulence, covering the background information necessary for the development of modified turbulence calculation techniques for a well-mixed atmospheric layer.

The third chapter covers the methodology for the research. Several new or expanded applications of satellite-derived applications are examined in this work. The three primary tasks were analyzing the height dependent error and bias present in the satellite-sounding data used in this research, expanding, improving, and evaluating the

satellite-based windfinding algorithm originally developed in the authors 2010 master's thesis [1], and developing several techniques to derive optical turbulence strength from the sounding and NWP data. These three topics are detailed in Sections 3.1, 3.2, and 3.3. The methodology for the additional topics of satellite-based cloud location, cloud-top height determination, and techniques to use the NWP model data to fill in temporal gaps between satellite overpasses is also presented in Chapter 3.

Chapter 4 presents and analyzes the results obtained by implementing the techniques developed and explained in Chapter 3. These two chapters share a parallel structure, with Sections 4.1, 4.2, and 4.3 detailing the results from the methods described in Sections 3.1, 3.2, and 3.3. Chapter 5 summarizes the impact of the project, details the conclusions drawn from this research endeavor, and outlines recommendations for areas of follow-on research.

The satellite sounder and imager data used throughout this research are collected by instruments onboard satellites that are part of NASA's Earth Observing System (EOS). These data are transmitted to ground stations and relayed to White Sands, NM via the Tracking and Data Relay Satellite System (TDRSS). The data are then sent to the appropriate Distributed Active Archive Center (DAAC) for additional processing and distribution. All of the satellite data sets used in this research are publically available for download from either the Goddard Earth Sciences Data and Information Service Center (GES-DISC) or the EOS Data and Operations System (EDOS).

2 Background and Literature Review

2.1 Infrared Sounder Theory

2.1.1 Blackbody Theory

The wavelength dependent intensity of the upwelling radiation detected by a meteorological satellite is dependent on the temperature of the atmosphere as described by Planck's function [2]

$$B_\lambda(T) = \frac{2hc^2}{\lambda^5\left(e^{hc/k_B\lambda T} - 1\right)} \tag{1}$$

where c = 2.998 x 10^8 m/s is the speed of light, h = 6.626 x 10^{-34} J s is Planck's constant and k_B = 1.381 x 10^{-23} J/K is Boltzmann's constant.

The wavelength at which the Planck function peaks indicates the temperature of the blackbody, according to Wien's Displacement Law [3]

$$\lambda_{\max} = \frac{k_W}{T} \tag{2}$$

where the constant $k_W = 2897.9 \mu m\ K$.

To use these relationships, it is necessary to determine how closely the atmosphere approximates a perfect blackbody in the infrared. The emittance of a body can be wavelength dependent and is defined as:

$$\varepsilon_\lambda = \frac{emitted \cdot radiation \cdot at \cdot \lambda}{B_\lambda(T)} \ . \tag{3}$$

A perfect blackbody has an emittance equal to one, and by Kirchhoff's Law, would have an absorptance equal to one if it is in local thermodynamic equilibrium. Below about 100

km altitude in Earth's atmosphere, collisions between molecules are frequent enough to make the assumption of local thermodynamic equilibrium reasonable [3]. For satellite meteorology applications, it is a good approximation to say that wavelength dependent absorptance equals the wavelength dependent emission, $\alpha_\lambda = \varepsilon_\lambda$.

2.1.2 Satellite Retrieval of Temperature

The ability to look down from space and measure atmospheric temperatures at multiple depths within the atmosphere relies on molecular absorption by atmospheric gases. By knowing the concentration of a gas in the atmosphere and its mass absorption coefficient for a given wavelength, an optical depth can be determined. When a space-based sensor with a narrow field-of-view collects upwelling radiation within a narrow wavelength channel, the altitude from which most of that radiation emanated can be determined.

If one of the constituent molecules that make up the atmosphere strongly absorbs the wavelength being measured, any emissions from the surface or lower atmosphere will not make it to space. Instead, almost all of the emission received will be from an altitude near the top of the atmosphere. For a different channel, one with a wavelength for which the atmosphere is transparent, most of the radiance measured by a space-based sensor emanates from the warmest, thickest layer of the atmosphere (the very bottom of the atmosphere) and the surface of the Earth. Between these two extremes, each channel falls somewhere along the sloped edge of a molecular absorption line, and a weighting function is calculated, as described in Equation (4) and Figure 1. The height at which the weighting function peaks is important. The sensor receives a larger fraction of the atmospheric

thermal emission from that height than from any height above or below it. Schwarzchild's equation is manipulated to yield a weighting function for each individual wavelength.

$$W_\lambda(h,\mu) = \frac{d}{dh}\left(\tau_\lambda^{1/\mu}\right) \tag{4}$$

where h is a generalized height coordinate, μ is the cosine of the zenith angle, and $\tau_\lambda^{1/\mu}$ is the slant path transmittance from level h to the satellite. For each wavelength measured, the peak in this weighting function is used to assign a height to the radiance measured. The process of assigning temperatures to these heights is more complicated—an iterative process of solving to find a full temperature profile that would result in the radiance measured across all of the sounder's channels [3] [4].

The most commonly used gases in temperature sounding are carbon dioxide, water vapor, oxygen and ozone (carbon dioxide and oxygen having the advantage that they are well-mixed to an altitude of 80 km, making it possible to determine their densities with altitude) [5]. Without knowing concentration, the altitude for water vapor returns is difficult to determine, but water vapor channels are useful for imagery. Common absorption wavelengths used by satellites are in the vicinity of 15 μm (carbon dioxide), 9.6 μm (ozone), and 5-8 μm (water vapor) [3]. The primary satellite instrument exploited in the research, the Atmospheric Infrared Sounder (AIRS), additionally takes advantage of the 15 μm and 4.3 μm carbon dioxide absorption features [6].

The determination of temperature by passive atmospheric sounding starts with Schwarzchild's equation, shown in Equation (5). Vertical sounding theory relies on the integrated form of this equation:

$$L_\lambda = L_0 e^{-\frac{\delta_0}{\mu}} + \int_0^{\delta_0} e^{-\frac{\delta_0 - \delta_\lambda}{\mu}} B_\lambda(T) \frac{d\delta_\lambda}{\mu} \ . \quad (5)$$

L_λ is the radiance measured by the satellite instrument, L_0 is the radiance incident on the absorber of interest, $B_\lambda(T)$ is the Planck function, and μ is the cosine of the zenith angle. δ_0 is defined as the vertical optical depth of the entire atmosphere and the wavelength dependent optical depth δ_λ is used to determine height in the atmosphere.

The usefulness of an individual measurement is limited, but when measurements are combined from a series of closely spaced channels, each receiving a slightly different wavelength near a strong molecular absorption line, a temperature profile can be constructed. Since the gas has a different optical depth for each wavelength, each channel of the sensor will be most sensitive to radiance emitted by a different altitude in the atmosphere. Matching these individual measurements to a first-guess model of the atmosphere through an iterative process can yield a full temperature profile.

The radius of typical operational polar orbits are much lower than geostationary orbits (700-800 km vs. 35,786 km), and therefore do not need short wavelengths to have useful resolution [3]. For this reason, instruments on a polar, low Earth orbiting satellite can take advantage of microwave absorption features like oxygen's strong rotation feature at 60 GHz (5 mm). The Advanced Microwave Sounding Unit (AMSU) is an instrument employed on polar orbiting satellites which uses 15-20 channels, several on the edge of this oxygen absorption band.

The weighting functions for these AMSU channels plotted against pressure in millibars (mb) is shown in Figure 1. One millibar is equal to one hectopascal (hPa). For

each wavelength, approximate altitude can be determined using the pressure for the point where the corresponding channel's weighting function reaches a maximum [2].

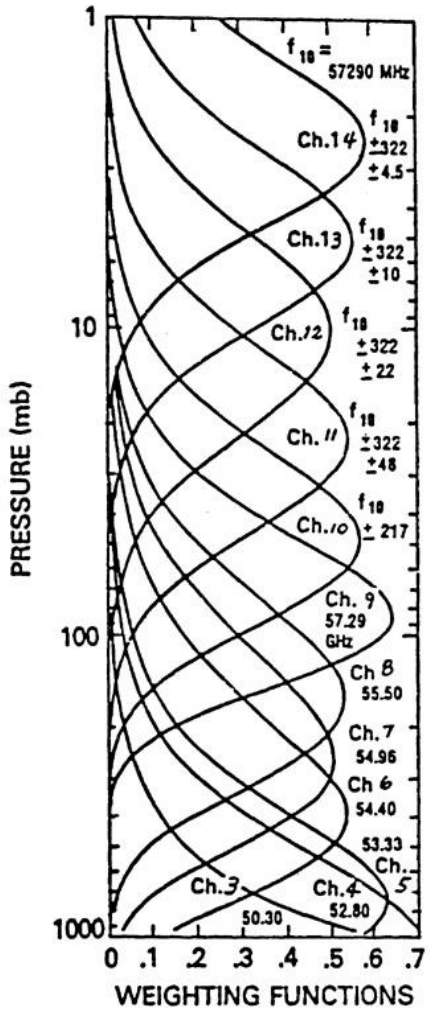

Figure 1. Microwave weighting functions for AMSU-A sounding channels (Courtesy NASA/GES-DISC) [7].

2.2 The Atmospheric Infrared Sounder (AIRS)

High resolution infrared sounders, such as the AIRS instrument onboard NASA's Aqua satellite, provide global atmospheric temperature measurements with excellent vertical resolution, comparable to the measurements made by weather balloons. AIRS is

an infrared spectrometer with 2378 channels covering a spectral range between 3.7 and 15.4 μm, taking advantage of carbon dioxide absorption features at both 4.3 μm and 15 μm. The Aqua satellite's polar orbit and the AIRS instrument's swath width of about 1600 km, lead to soundings covering most of the planet twice each day. The IR instrument does not retrieve measurements from below the highest layer of clouds, but microwave soundings from the Advanced Microwave Sounding Unit (AMSU), also onboard Aqua, are used to fill in missing surface and lower atmosphere temperature measurements [1]. Figure 2 depicts the scan geometry for the AIRS instrument, detailing field-of-view geometry and scan pattern overlap [8].

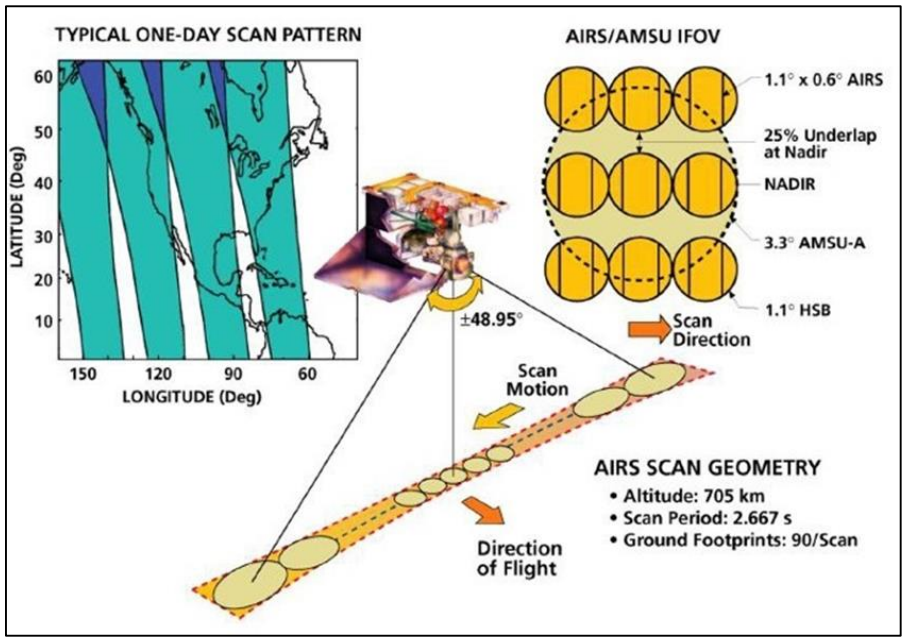

Figure 2. Scan geometry for the AIRS instrument (Courtesy NASA/GES DISC) [9].

During each 99 minute orbit of the satellite, the Earth rotates approximately 25 degrees about its axis, so that each Aqua ground track crosses the equator approximately 1730 km west of the previous crossing, as shown in Figure 3. Near the equator, the coverage is not complete and the surface area missed is filled in by the next day's flight

path. At latitudes greater than about 45 degrees, each swath overlaps the previous one causing some locations to be sounded four (or more) times per day. Most locations on Earth fall within the AIRS data swath twice in a 24 hour period, under both an ascending pass (during the local afternoon) and a descending satellite pass (during the local early morning). One of the primary objectives of this research is the development and evaluation of new techniques to exploit this AIRS temperature data for directed energy applications.

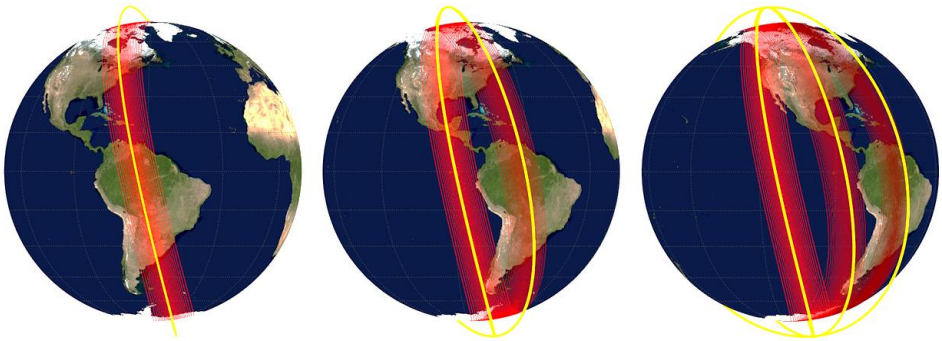

Figure 3. AIRS coverage during three sequential ascending passes on 1 Oct 2015. The left image is the first pass between 1726 and 1816 UTC. The center image shows the first pass and the second pass, between 1906 and 1956 UTC. The right image shows the first two passes, and adds the third 2046 to 2136 UTC pass.

2.3 Additional Meteorological Satellite Instruments Investigated

The AIRS instrument has excellent vertical resolution, but poor horizontal resolution when compared to imaging instruments, and it has the limitation of not being able to retrieve temperatures below thick cloud cover. AIRS is one of five scientific instruments on the Aqua satellite, and Aqua is part of NASA's A-Train constellation of Earth-observing satellites. These satellites follow the same orbital track with the trail satellite only a couple minutes behind the lead. The common ground track and near simultaneous observations

of each satellite instrument enable multiple data sets to be used together, so that the strengths of one type of instrument can make up for the shortcomings of another.

The orbits of the satellites in the A-Train constellation are sun-synchronous, meaning the orbit's 98.14° inclination is chosen so that for its semi-major axis of 7078 km, the right ascension of the orbit's ascending node precesses at the same rate as the Earth's revolution around the sun. This causes the ground track to pass over each location on the Earth at approximately the same local time every day, throughout the year [3]. The A-Train gets its name from the fact that the satellite formation always crosses the equator northbound in the early afternoon local time for the region directly below—the 'Afternoon Train.' Figure 4 shows the satellites and instruments that make up the NASA A-Train.

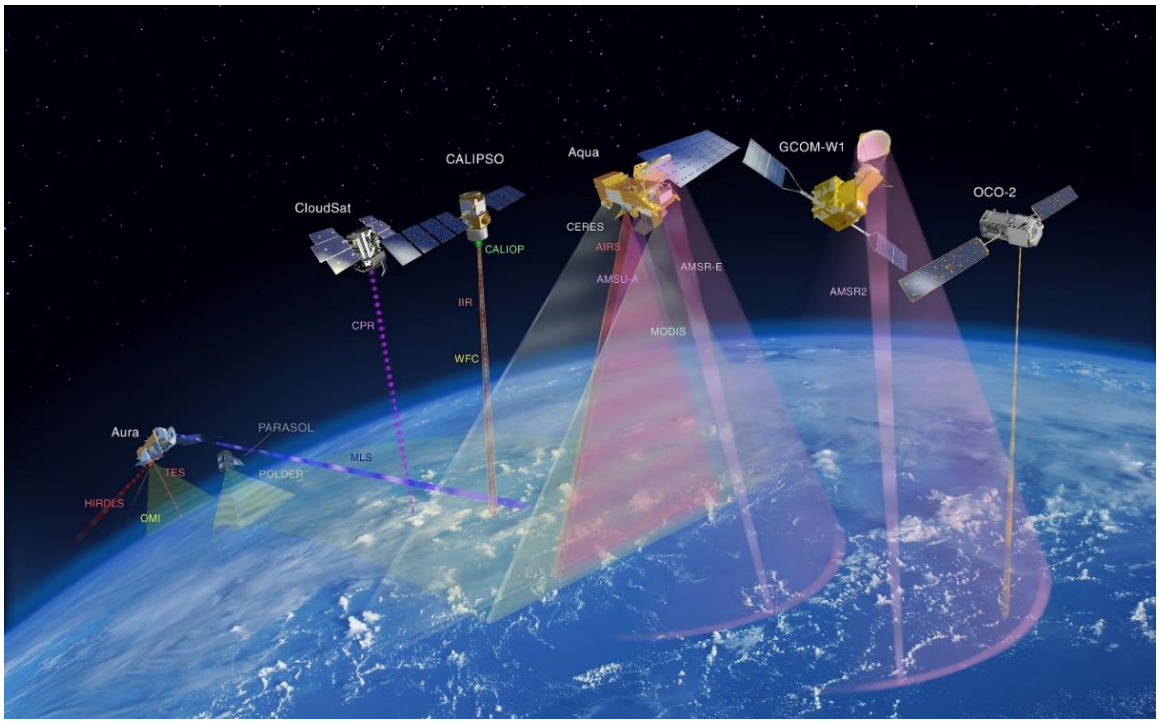

Figure 4. NASA depiction of the A-Train constellation showing sensor geometry for the primary Earth-observing instruments (Courtesy NASA/JPL-Caltech) [10].

2.3.1 Advanced Microwave Sounder (AMSU)

The AMSU began operation in 1998, and is onboard satellites NOAA-15 through NOAA-19, NASA Aqua, and EUMETSAT MetOp A and MetOp B. The instrument consists of two separate sounders. These sounders are the AMSU-A (with 15 channels between 23.8 and 89 GHz) and the AMSU-B (with 5 channels between 89.9 and 183.3 GHz). The AMSU employs a whisk broom scan pattern, sweeping 49.5 degrees on either side of nadir for a 1650 km wide swath. Nadir is the viewing angle of the centerline of the data swath, directly below the satellite's track. During each 6 second sweep, radiance values for every channel are collected for 30 fields of view for the AMSU-A. The higher frequency AMSU-B collects radiance from 90 fields during each sweep. The cross-track resolution at nadir is 45 km for AMSU-A and 15 km for AMSU-B [3] [8].

The AMSU sounders work well in combination with infrared sounders, which are not useful for tropospheric measurements below cloud cover. Because the AMSU has only 20 channels, the vertical resolution of the sounding data does not match the infrared sounders, but the microwave frequencies are able to pass through cloud cover and measure brightness temperatures all the way to the surface. The AMSU senses upwelling terrestrial radiation, comprised of a combination of radiation emitted by Earth's surface and radiation emitted by the atmosphere. As discussed in Section 2.1.2, each channel is radiatively selective, primarily detecting microwave radiation from a discrete layer within the atmosphere. The height of this layer corresponds to the height at which that channel's weighting function reaches a maximum value. On NASA's Aqua satellite, the standard AMSU-B was replaced with a modified, 4-channel version, called the Humidity Sounder for Brazil (HSB). The HSB stopped operating in February of 2003 due to an electrical

failure within the components that control the scanning mirror, thus the only microwave sounding data available from the Aqua satellite since that time are for the AMSU-A channels.

2.3.2 Moderate Resolution Imaging Spectroradiometer (MODIS)

The Moderate-resolution Imaging Spectroradiometer is a scientific instrument onboard NASA's Earth observing Aqua and Terra satellites. MODIS captures radiation in 36 spectral bands with wavelengths between 0.4 and 14.4 µm. The spacing of these spectral bands relative to atmospheric absorption features is shown in Figure 5. An advantage of the MODIS data is the spatial resolution for these channels, providing horizontal resolution ranging from 250 m to 1 km.

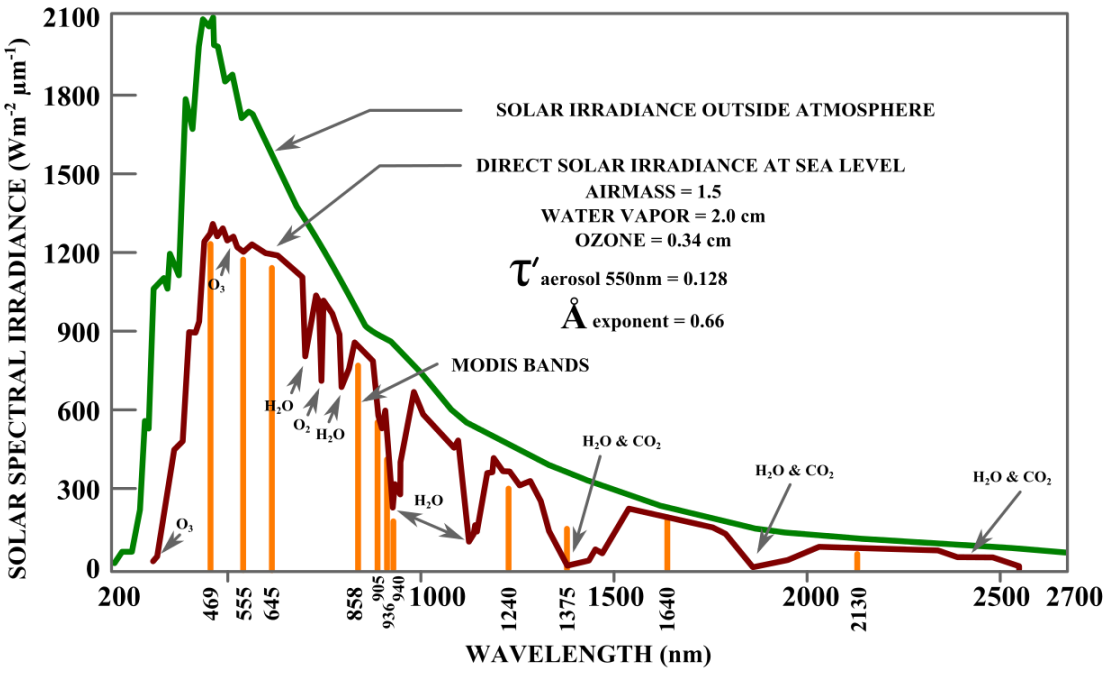

Figure 5. MODIS channel wavelengths (Courtesy NASA) [11].

In-flight calibration of the data is accomplished using an internal blackbody, a solar diffuser, and a spectral radiometric calibration assembly. Each MODIS instrument images a 2330 km wide swath, collecting data for almost all of the Earth's surface twice daily. Figure 6 shows the coverage of 24 hours of sequential descending MODIS passes.

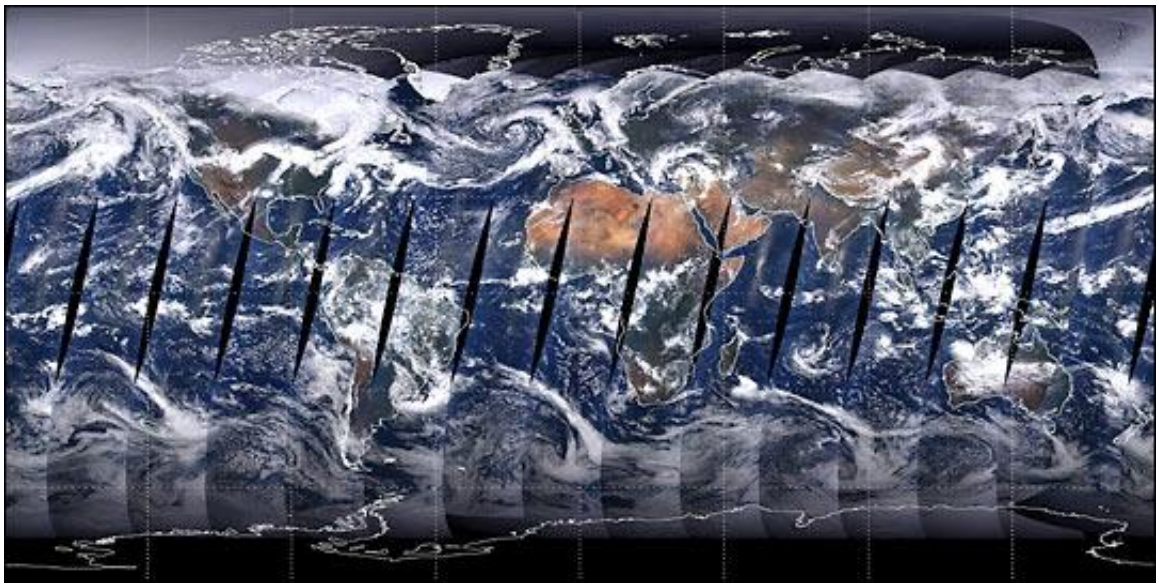

Figure 6. MODIS imagery from the 14 descending passes during one 24 hour period. This image was retrieved from https://lpdaac.usgs.gov, maintained by the NASA EOSDIS Land Processes Distributed Active Archive Center (LP DAAC) at the USGS/Earth Resources Observation and Science (EROS) Center, Sioux Falls, South Dakota. The data product for the image was provided by NASA [12].

2.3.3 Cloud-Aerosol LIDAR and Infrared Pathfinder Satellite Observations (CALIPSO)

The CALIPSO satellite is also a member of the NASA A-Train, following about one minute and 15 seconds behind Aqua. CALIPSO's LIDAR emits and measures backscatter at 532 nm and 1064 nm. This instrument has the ability to not only detect the

top and bottom heights of multiple cloud layers but also to distinguish between aerosol particles and cloud droplets and retrieve information about cloud properties. The ability to differentiate between effects of aerosols and clouds, and the determination of cloud type, allows accurate estimation of wavelength dependent path extinction. Figure 7 shows an example of how CALIPSO's vertical resolution and cloud property measurements can be combined with data from other instruments. In this case the 2-D CALIPSO data are overlaid on a corresponding Moderate Resolution Imaging Spectroradiometer (MODIS) image, both collected as the A-Train passed over Hurricane Bill in 2009.

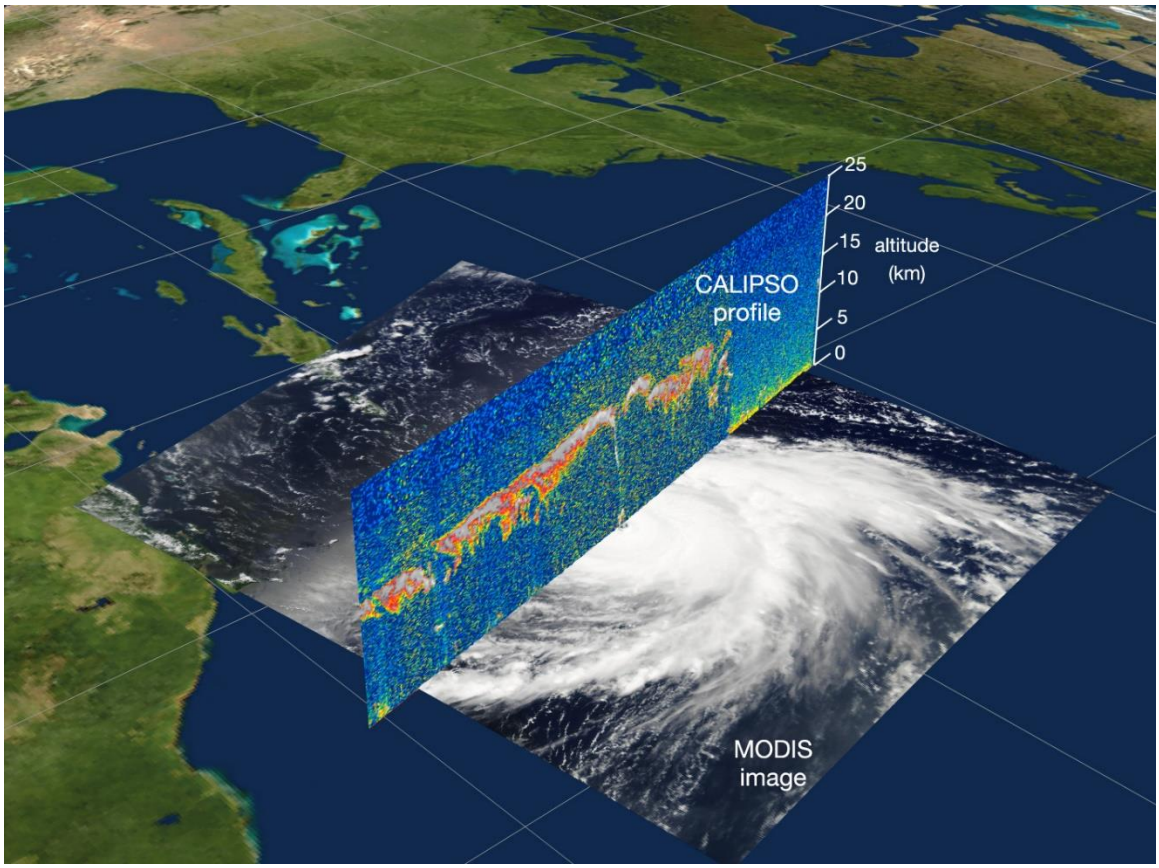

Figure 7. NASA image of overlapping CALIPSO and MODIS data--ascending satellite pass over Hurricane Bill in 2009 (Courtesy NASA) [13].

2.4 Numerical Weather Prediction (NWP)

2.4.1 Global Forecast System (GFS)

GFS is a global, hydrostatic weather forecast model produced by the National Centers for Environmental Prediction (NCEP). The current GFS Global Spectral Model is operated at its standard 0.5 degree horizontal resolution grid, but an improved 0.25 degree grid became operational in late 2014. Both models are run 4 times per day, each with 3 hour forecast timesteps out to 240 hours, followed by a lower temporal resolution extension period at 12 hour timesteps out to 384 hours. The model runs on 64 vertical, unequally-spaced sigma levels. This means the pressure levels in the model are normalized by dividing level pressure by the surface pressure, $\sigma = p/p_s$, compressing the levels so that none of the model pressure levels exist below the Earth's surface. The 64 model levels extend up to a highest pressure level of 0.03 hPa, but the output product only includes 26 levels with a top pressure level of 10 hPa. For this reason, the top of the GFS coverage volume in the available data sets is typically around 30-32 km. The gridded model output is publically available for download through the NOAA Operational Model Archive and Distribution System (NOMADS) server [14] [15].

2.4.2 European Centre for Medium-Range Weather Forecasts (ECMWF)

An NWP model that provides a source for temperatures, heights of pressure levels, and winds above the top of the available GFS data is the European Centre for Medium-Range Weather Forecasts (ECMWF). Of particular interest in this research is the ECMWF Re-Analysis (ERA) project ERA-20C. The ERA-20C data set represents output from a global, coupled atmosphere, land surface, and ocean wave model, which was re-run with

assimilated surface observations. The data set has a 3-hour temporal resolution and 91 vertical model levels up to a top level pressure of 0.01 hPa, above 75 km, covering the entire troposphere, stratosphere, and much of the mesosphere. The ECMWF re-analysis data are available to the public, covering dates from the year 1900 through the end of 2010, overlapping the first eight years of AIRS data [16].

This ECMWF model is non-hydrostatic, meaning that it is able to calculate vertical pressure gradients and accelerations. Hydrostatic models assume hydrostatic equilibrium, forcing the downward weight of the atmosphere to balance the upward pressure gradient force. At all points in hydrostatic models, $\partial p / \partial z = -\rho g$, where p is pressure, z is height, ρ is density of the air, and g is acceleration due to gravity at the height z. Large scale vertical motion can be deduced in hydrostatic models from the convergence or divergence of air flows, but pressure perturbations not in balance with gravity are not allowed. Non-hydrostatic models include additional equations, not present in hydrostatic models. These extra equations allow smaller scale vertical accelerations to be directly calculated, but their inclusion comes at the cost of making the model more computationally expensive to run. The vertical acceleration equations are necessary for the model to be able to accurately account for buoyancy forces, convection, and any local deviations from hydrostatic equilibrium [15] [17]

The global coverage and excellent horizontal and vertical resolution of the ECMWF data make them valuable for AIRS data comparison and C_n^2 calculation. Figure 8, Figure 9, and Figure 10 show sample ECMWF output for 1800 UTC on 10 Mar 2010.

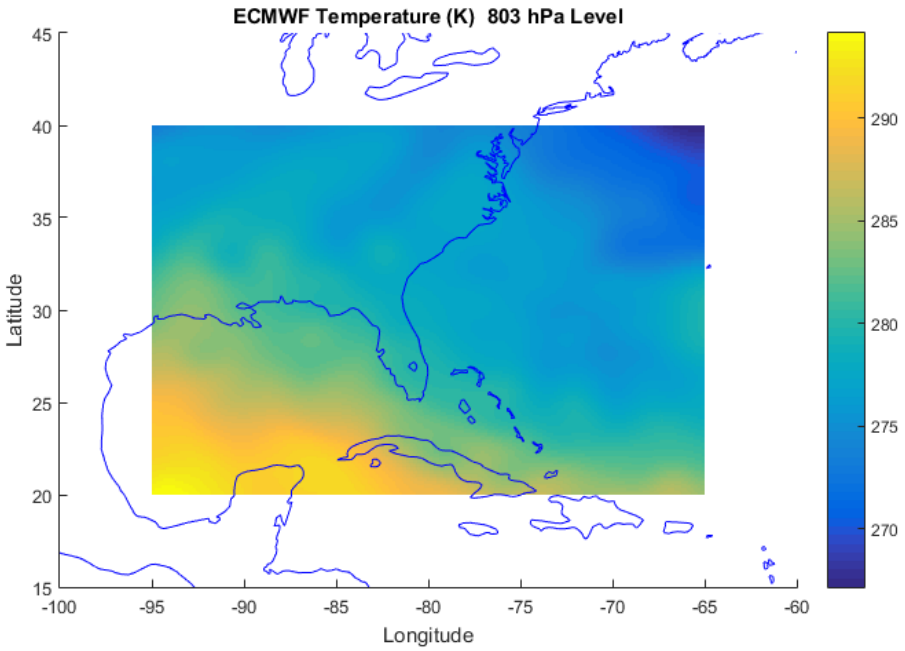

Figure 8. ECMWF Temperature, 803 hPa level, 10 Mar 2010, 1800 UTC.

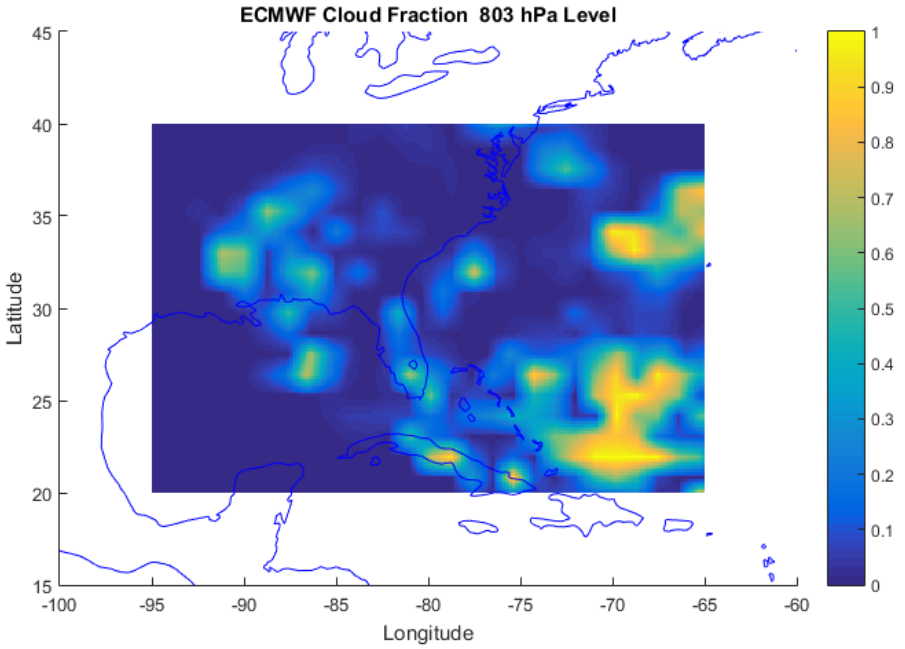

Figure 9. ECMWF Cloud Fraction, 803 hPa level, 10 Mar 2010, 1800 UTC.

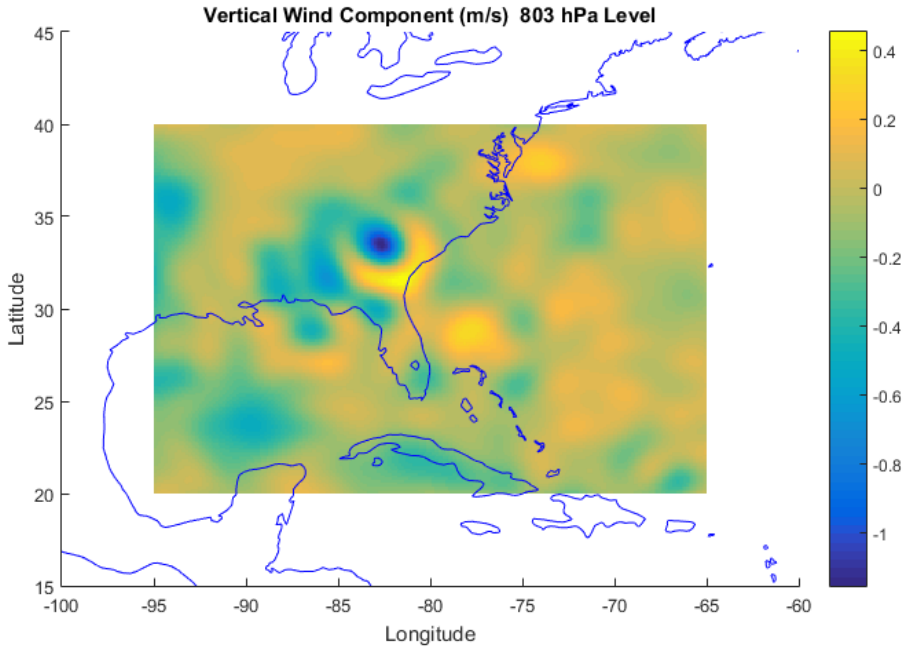

Figure 10. ECMWF vertical wind component, 803 hPa level, 10 Mar 2010, 1800 UTC.

2.4.3 Comparison of NWP models investigated

The primary NWP sources utilized in this research are the GFS and ECMWF models. Additional models were studied but were not included in the C_n^2 derivation methods developed. The ability to run the Weather Research and Forecasting (WRF) model internally (with a customizable domain and grid) and the 1 hour timestep of the High Resolution Rapid Refresh (HRRR) model are both advantages, but the fact that neither of these models provide global coverage led to them not being incorporated into the techniques developed. Table 1 details the coverage and resolution of five of the NWP models investigated for use in this research.

Table 1. Resolution comparison for NWP models investigated

Model	Domain	Horizontal Grid Spacing	Vertical Levels	Top Level Pressure	Temporal Resolution	Non-Hydrostatic
Global Forecast System (GFS) 0.50 deg	Global	0.50 deg	26	10 hPa	3 hr	No
Global Forecast System (GFS) 0.25 deg	Global	0.25 deg	26	10 hPa	3 hr	No
Weather Research and Forecasting (WRF)	Customizable to meet requirements					Yes
High Resolution Rapid Refresh (HRRR)	CONUS	3 km	50	20 hPa	1 hr	Yes
ECMWF ERA-20C Reanalysis	Global	0.125 deg	91	0.01 hPa	3 hr	Yes

2.5 Atmospheric Turbulence Theory

Optical turbulence in the atmosphere poses a problem for most electro-optical systems. It leads to image distortion for imaging sensors and beam spread for laser systems. Random fluctuations in the refractive index of air cause optical turbulence, leading to variations in the speed at which a wavefront propagates. The quantitative measure of the strength of the optical turbulence that is most often used is the refractive index structure function C_n^2 [18].

A structure function describes the spatial statistics of the parameter of interest and can be defined as

$$\mathcal{D}(r) = \left\langle \left[\phi(\vec{x}) - \phi(\vec{x'}) \right]^2 \right\rangle \tag{6}$$

where the separation between the two positions is designated r,

$$r = \left| \vec{x} - \vec{x'} \right| \tag{7}$$

The brackets $\langle\ \rangle$ in Equation (6) denote an ensemble average and isotropy, and homogeneity of the turbulence variance are implied [19].

Within the inertial subrange (the range of scales where turbulence is neither generated nor dissipated, bounded by the inner scale l_0 and the outer scale L_0) Kolmogorov turbulence follows the "two-thirds power law" [20]. For two positions separated by a distance r, the relationship between the index of refraction n at each position and the index of refraction structure function C_n^2 can be expressed as

$$\left\langle \left[n(x) - n(x+r) \right]^2 \right\rangle = C_n^2 r^{2/3} . \tag{8}$$

In this inertial subrange, C_n^2 is also proportional to the level of the power spectrum of refractive index fluctuations

$$\Phi_n(k_1) = 0.25 C_n^2 k_1^{-5/3} \tag{9}$$

where $\Phi_n(k_1)$ is the average one-dimensional power spectrum of the index of refraction n, and k_1 is the wave-number component in the direction of propagation [21] [22]. The structure function for refractive index, C_n^2, provides a measure of the strength of the optical turbulence. Typical C_n^2 values for strong optical turbulence exceeds 10^{-13} $m^{-2/3}$ and weak turbulence has C_n^2 values smaller than 10^{-16} $m^{-2/3}$ [23] [24] [25].

Atmospheric flow is complex in part because turbulent eddies can exist simultaneously on all spatial scales from the planetary scale (on order of 20,000 km) down to the fine scale (on order of 2 mm) and viscous dissipation subrange (molecular scale). The resulting atmospheric flow is the superposition of all of these turbulent eddies [26]. There is also complex interaction between horizontal motion and vertical motion. Buoyancy effects caused by heat transfer or phase change can have an effect on the type and strength of the turbulence [21]. The energy source for all of this motion is the non-uniform global distribution of differential heating, and the turbulent energy is transferred

from each scale to the next smaller scale, from planetary scale motion like the jet stream down to the smallest eddies where it is lost to friction [27]. The three spectral regions commonly discussed in atmospheric turbulence research are [21] [24] [28]:

1) Energy production range—turbulent energy is produced by buoyant forces and mechanical shear (on order of 2 km).
2) Inertial subrange—no energy is produced or dissipated; it is transferred from large turbulent eddies to smaller eddies (scales between the outer scale L_0 and the inner scale l_0).
3) Dissipation range—turbulent kinetic energy is converted to heat through friction (on order of 1 cm and smaller).

The work of Kolmogorov provides a unifying view of turbulence dynamics across these spectral regions. Kolmogorov's theory describes small scale turbulence structure as statistically homogeneous and isotropic [23]. The distribution of turbulent energy within the inertial subrange, according to Kolmogorov's hypothesis, can be determined by the 5/3 law, which states subrange spectral densities are proportional to $k^{-5/3}$, where k is the magnitude of the three-dimensional wave number. These spectral densities allow the determination of the energy transfer rate or energy dissipation rate [24] [29].

While C_n^2 values vary significantly with changes in atmospheric conditions, there is a general dependence on height that allows for the creation of standard vertical profile models. One of these standard models is Hufnagel-Valley, with the common implementation H-V 5/7. In this implementation, when integrated for a vertical path at a wavelength of λ=0.5 μm, the resulting turbulent coherence length ρ_0 is 5 cm, and the isoplanatic patch size, θ_0, is 7 μrad. These values are typical for nighttime observations in

the field of astronomy. Turbulent coherence length, the length over which phase distortion has the mean square value of 1 rad^2, is a parameter used to describe the amount of blur effects on receiver systems. The parameter isoplanatic patch size also comes from the field of astronomy, where it defines the maximum angular distance at which two moving points appear to shift position in unison. At this angular difference between paths, the mean square wavefront error is 1 rad^2. [30] [31]. H-V has the form

$$C_n^2(z) = 8.148\times10^{-26}U^2z^{10}e^{-z} + 2.700\times10^{-16}e^{-z/1.5} + C_n^2(0)e^{-10z} \qquad (10)$$

where the surface value $C_n^2(0)$ = 1.7x10^{-14} m$^{-2/3}$ and an upper level wind speed U = 21 m/s yield the 5/7 implementation [28] [30] [32] [33]. Figure 11 depicts H-V 5/7 plotted against another common standard model, Critical Laser Enhancing Atmospheric Research (CLEAR) 1 Night.

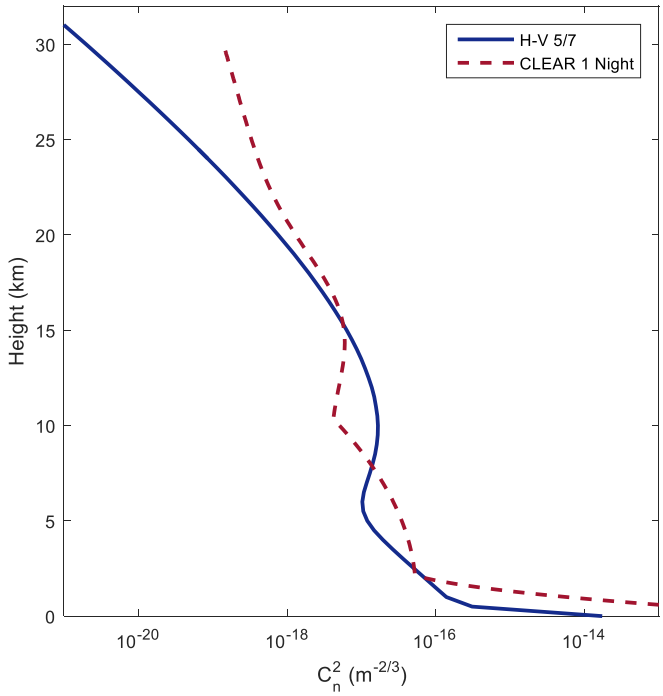

Figure 11. Comparison of two standard vertical C_n^2 profile models, H-V 5/7 and CLEAR 1 Night.

The refractive index of air is a function of pressure, temperature, and water vapor concentration. At radio wavelengths the most important of these factors is the water vapor. In analysis of refractive index fluctuations affecting radio transmission, it is common to consider only the water vapor concentration gradients or, in the approach described by Tatarskii, to consider the water vapor and temperature gradients. At optical wavelengths the water vapor has little influence on refractive index, and the standard approach taken is to base optical refractive index fluctuations solely on temperature fluctuations. In both of these regions of the electromagnetic spectrum, the traditional approach is to treat pressure fluctuations as negligible [34] [35]. A pressure gradient term is derived, analyzed, and incorporated into a modified C_n^2 calculation process detailed in Section 4.3.5.

3 Methodology

3.1 AIRS Temperature Measurements and Retrieving AIRS Data

AIRS data files are made available to the public by NASA, searchable by time and geographic coverage through the Mirador Earth science data search tool developed and maintained by GES-DISC [36]. For this research, an automated process built using MATLAB® is used to search the NASA database and retrieve the required AIRS data files for processing. In order to have radiosonde wind profiles available to compare to the profiles derived from satellite soundings, many of the locations for this research were selected in the vicinity of rawinsonde sites that the Aqua satellite passes over near the scheduled daily weather balloon release times (0000 UTC and 1200 UTC) [37]. These locations lie in north-south bands near 20° E and 160° W longitude, and due to Aqua's sun-synchronous orbit, the location of these bands remains constant throughout the year. Rawinsonde observations for this research were obtained through a website maintained by the University of Wyoming's Department of Atmospheric Science [38].

The continuous stream of AIRS data is broken into six-minute granules. Each AIRS data point within the granule corresponds to one of the 1350 sounding locations covered during those six minutes (45 points along the flight path, 30 points wide). The field-of-view center coordinates for each of the sounding locations in one data granule are shown in Figure 12. This file covers a segment of a descending AIRS pass that tracked along the eastern border of Alaska.

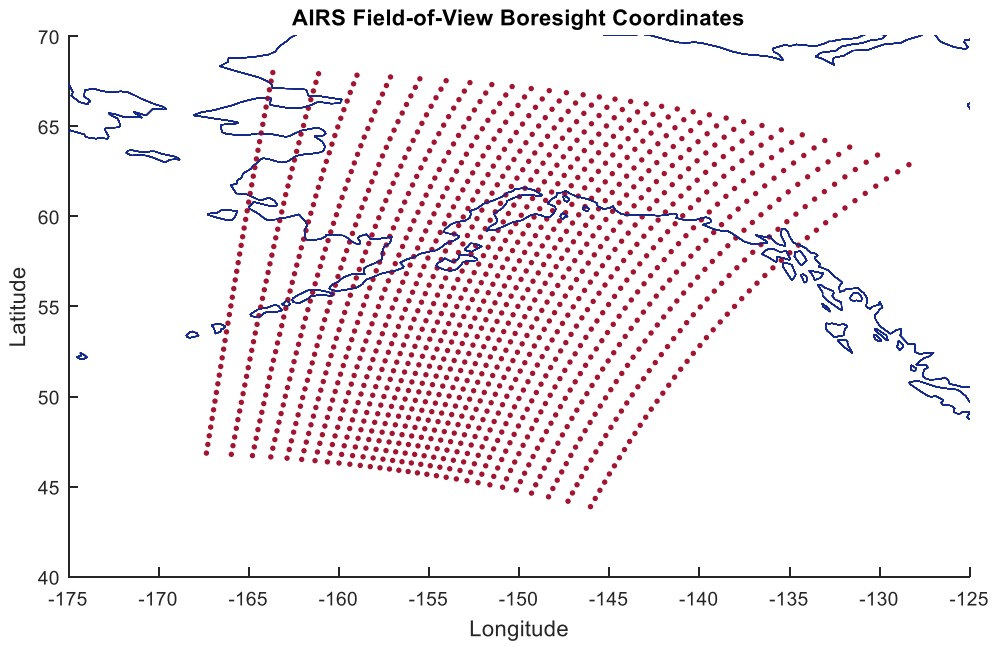

Figure 12. Depiction of sounding boresight coordinates for a 6-minute data granule. In this example granule number 125 on 15 Oct 2014 represents this segment of this descending AIRS pass over Alaska between 1229 and 1235 UTC.

The level 2 AIRS data set contains atmospheric temperature values for 100 standard vertical pressure levels at each sounding location. These pressure levels are the same for each sounding column, making it straightforward to compare one sounding to another. The first step in selecting the appropriate AIRS files for download is the determination of a date and time, and a set of coordinates of interest. The Mirador server is searched, and if there is an AIRS granule that includes the entered coordinates during the specified time search window, it is downloaded (two granules are downloaded if the entered coordinates fall within 300 km of the leading or trailing edge of the granule). For one of these data granules, a horizontal layer of temperatures at the AIRS standard pressure level of 753.6 hPa is shown in Figure 13.

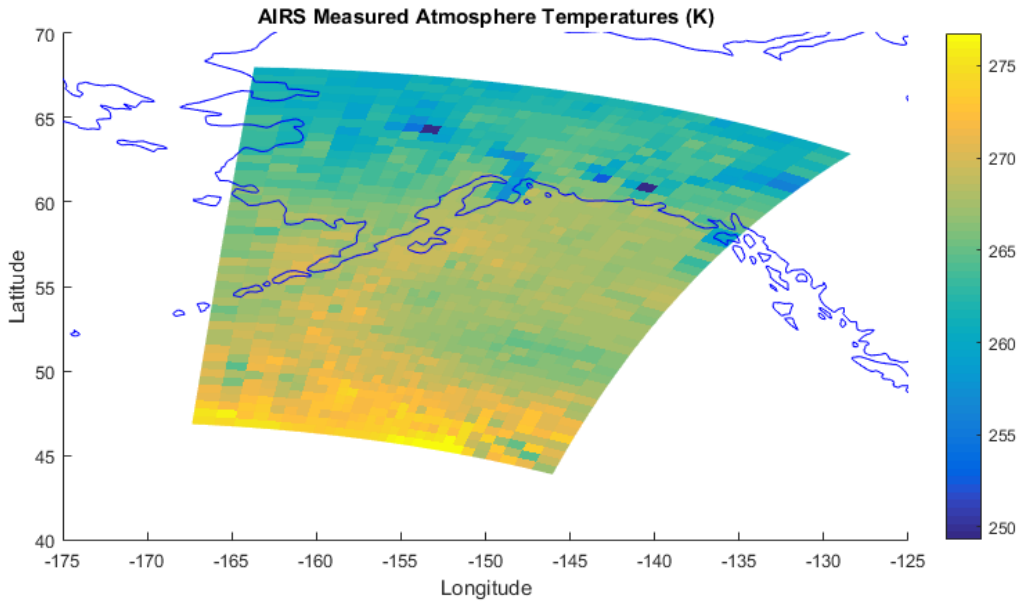

Figure 13. Horizontal slice through the volume of AIRS-retrieved temperatures contained in a 6-minute data granule at 753.6 hPa, 1229-1235 UTC, 15 Oct 2014.

The retrieved data are filtered to select the vertical temperature profiles for all sounding locations within 300 km of the coordinates of interest. This filtered data set includes approximately 160-200 sounding locations within each pressure layer, making up a circular region 600 km across. For each sounding location, the data set includes surface pressure, surface geopotential height, and a temperature measurement for up to 100 pressure levels between 0.0161 hPa and 1100 hPa (all 100 temperatures may not be available due to terrain elevation and surface pressure). During the level 2 processing to calculate temperature values from the satellite measured IR radiances and microwave brightness temperatures, an error value is assigned to each temperature.

The AIRS field-of-view coordinates provide the correct latitude and longitude coordinates for only the lowest altitude field-of-view, where the AIRS instrument's line of sight intersects the surface of the Earth. As the instrument sweeps across each scanline,

the angle varies between 49 degrees left of nadir to 49 degrees right of nadir. The coordinates of each temperature measurement above the surface layer are not calculated, nor are they provided with the AIRS level 2 products, but the satellite's latitude, longitude, and altitude are reported throughout each orbit. The atmospheric height of each temperature measurement is known, so extending a line from each surface location to the satellite's position allows assignment of correct latitude and longitude coordinate to each measurement along that line. Figure 14 depicts the result of this process, showing the corrected location of each of the 135,000 temperature retrievals during a 6-minute data granule. Each red line in this figure depicts the column of 100 soundings, which correspond to a single AIRS field-of-view at the surface.

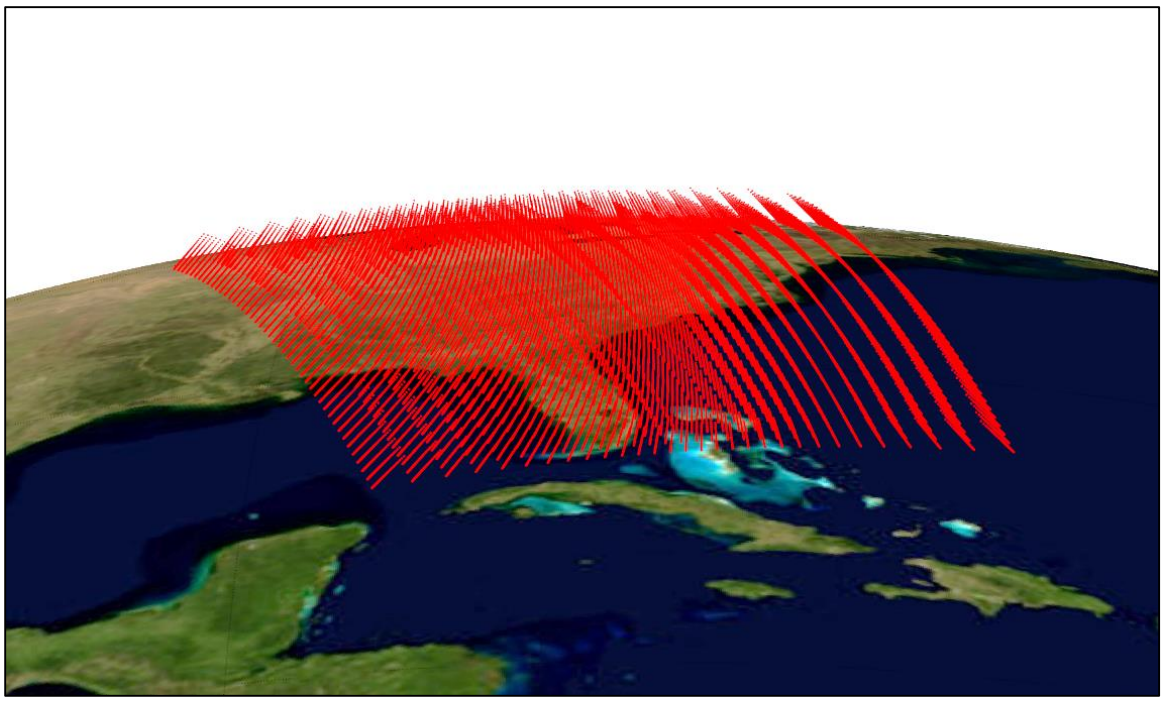

Figure 14. Corrected latitude and longitude coordinates for entire 3-D granule of AIRS temperature data during an ascending AIRS pass over Florida.

3.2 AIRS-Derived Wind Profiles—Vertical Wind Profile Calculation Using the Thermal Wind Equations

For each of the 100 AIRS pressure levels, smooth surfaces are fit through the pressure heights and temperature distributions. These surfaces are used to find the local slope of the isobaric surface and the rate of temperature change along the pressure level in both the east-west and the north-south directions. An example AIRS data granule is plotted in Figure 15.

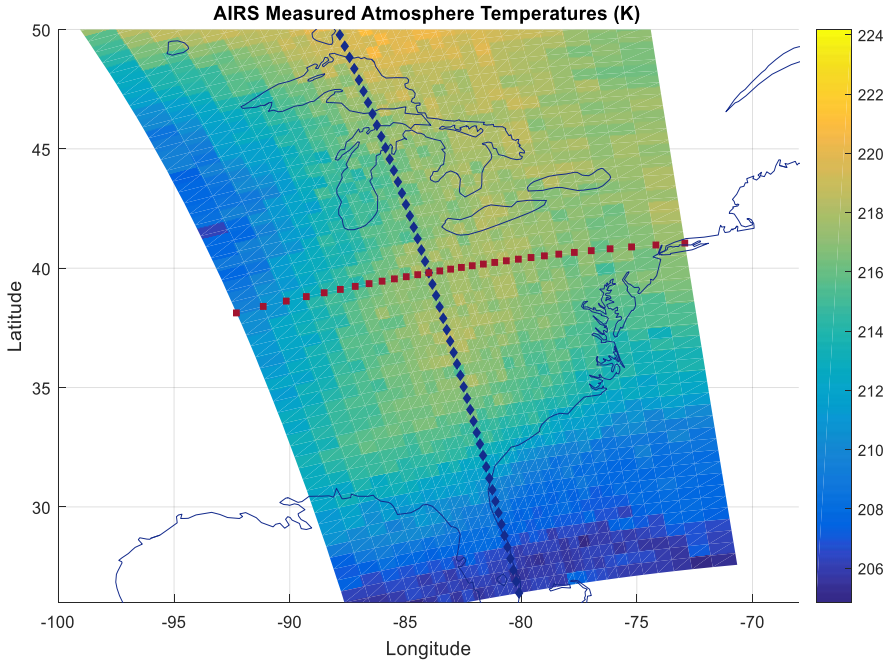

Figure 15. Sample of sounding locations surrounding coordinates of interest—along satellite flight path (blue diamonds) and perpendicular to satellite flight path (red squares). This granule of AIRS data was collected on 24 Oct 2014, as the Aqua satellite overflew Dayton, OH at 1839 UTC. This horizontal slice through the data shows retrieved temperature at the 151 hPa pressure level (heights between 13.1 and 14.2 km).

Figure 16 and Figure 17 illustrate, in two dimensions, how the smoothing process leads to the required gradients [1]. Figure 16 shows two cross-sections through a sounding data set. The north-south trail of blue data points show a slice of sounding locations parallel to the flight path of the satellite and the red locations identify an east-west scanline perpendicular to satellite track, corresponding to the blue and red tracks in Figure 15. The two tracks intersect at the sounding location nearest to the input target coordinates. In Figure 16, the temperature measurements within the 151 hPa layer for each sounding location along these two lines are plotted. The small error and variation in the temperatures can lead to many different values for temperature gradient, depending on how many data points are included, and how a surface is fit to the data.

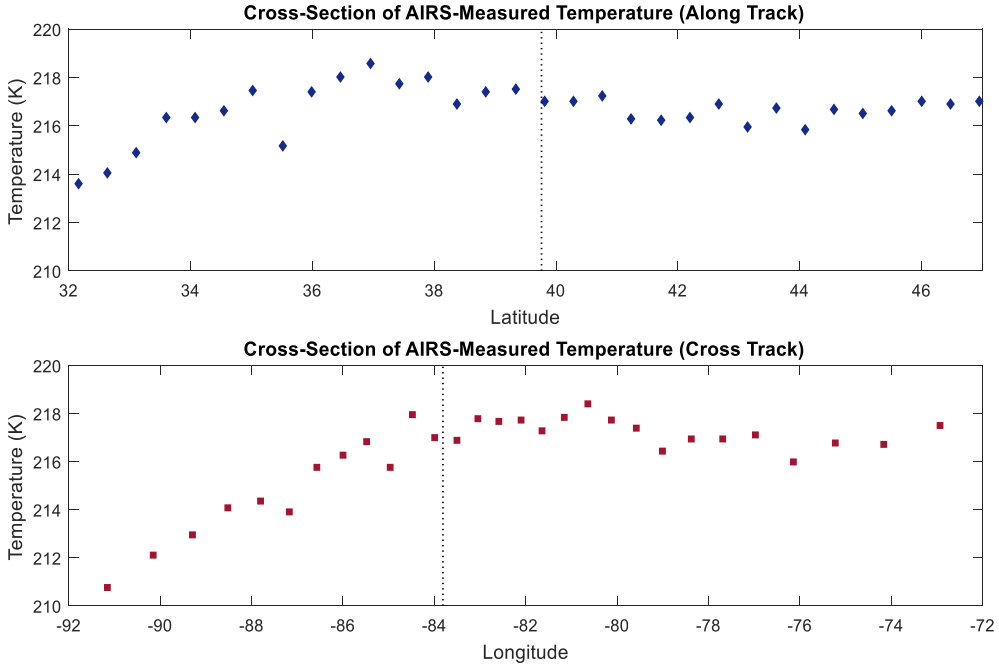

Figure 16. Satellite measured temperatures at the 151 hPa pressure level along the satellite flight path (blue diamonds) and perpendicular to the satellite flight path (red squares) for the data granule shown in Figure 15. The vertical dotted lines indicate the coordinates of interest.

To smooth the data, and calculate the most accurate temperature and height gradients, a surface needs to be fit to the data to reduce the effect of error in the temperature and height data. A three-dimensional surface is fit to each level's data by local regression smoothing (specifically the Robust Locally Weighted Scatter Plot Smoothing function within the MATLAB® Curve Fitting Toolbox [39]). Representative cross-sections of this smooth surface are shown in Figure 17. The temperature gradient is determined by finding the slope of this surface at the target coordinates, and by a similar curve fitting process, the slopes of the isobaric surfaces are determined. This method of smoothing accounts for more data points than just the few immediately surrounding the target coordinates, and it minimizes the effect of error in the individual satellite measured temperatures.

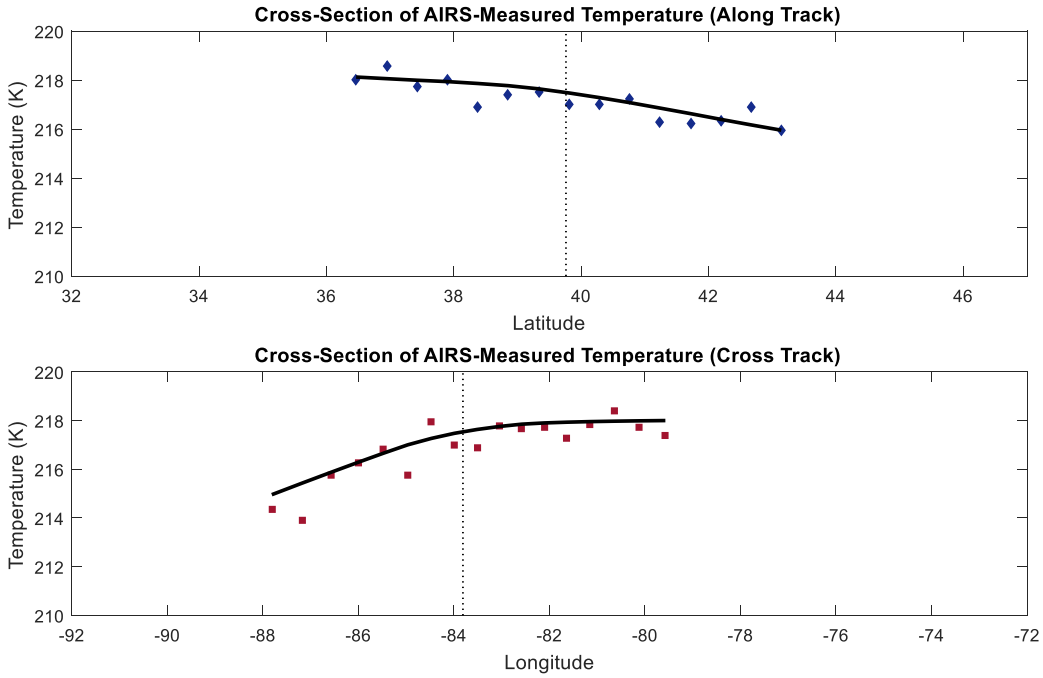

Figure 17. Cross-sections of the 3-D smoothed surface fit to all AIRS temperature measurements within 300 km of the input target coordinates for the 151 hPa pressure level data shown in Figure 15 and Figure 16.

The vertical temperature gradients are found by dividing the difference in temperature at the center of two pressure surfaces by the vertical separation between the surfaces, and repeating this process for each pair of pressure surfaces. Once all of the required temperature and pressure height gradients are calculated, the wind profile can be assembled from the bottom up or the top down, one level at a time.

The thermal wind relationship between components of the geostrophic wind, u_g and v_g, at two consecutive levels in the atmosphere, 1 and 2, is described in Equations (11) and (12). This development makes two important assumptions—that the atmosphere is in both hydrostatic and geostrophic balance. When expressed as components, u is the zonal velocity, the component of the horizontal wind from the west, and v is the meridional velocity, the component of the horizontal wind from the south. The change in magnitude of each wind component, from one level to the next, can be found by

$$\left(u_g\right)_2 - \left(u_g\right)_1 = -\frac{g_0}{f}\frac{\partial\left(z_2 - z_1\right)}{\partial y} \tag{11}$$

and

$$\left(v_g\right)_2 - \left(v_g\right)_1 = \frac{g_0}{f}\frac{\partial\left(z_2 - z_1\right)}{\partial x} \tag{12}$$

where g_o is the acceleration due to gravity at sea level, and f is the Coriolis parameter, which depends on latitude. The thickness of each layer $z_2 - z_1$ is linearly proportional to the mean temperature within the layer, as described by the hypsometric equation [26]:

$$z_2 - z_1 = \frac{R_d \bar{T}_v}{g_o}\ln\left[\frac{p_1}{p_2}\right]. \tag{13}$$

where R_d is the dry gas constant, 287 J/K kg, and $\bar{T}_v$ is the mean virtual temperature in the layer. The variables p_1 and p_2 are the atmospheric pressures at the levels at the bottom and top of the layer. Combining Equations (11), (12), and (13) provides a method for determining the vertical change in *u* and *v* components of the geostrophic wind through each layer. The change in wind between the top and bottom of a pressure layer is a function of the vertical change in pressure through the layer and the horizontal temperature gradient, as described in Equations (14) and (15):

$$\left(u_g\right)_2 - \left(u_g\right)_1 = -\frac{R_d}{f} ln\left[\frac{p_1}{p_2}\right]\left(\frac{\partial T}{\partial y}\right)_p \tag{14}$$

and

$$\left(v_g\right)_2 - \left(v_g\right)_1 = \frac{R_d}{f} ln\left[\frac{p_1}{p_2}\right]\left(\frac{\partial T}{\partial x}\right)_p \quad . \tag{15}$$

The form of the thermal wind relationship shown in Equations (14) and (15) neglects the dependence on vertical temperature gradient, which also contributes to the wind gradient [26]. A more complete set of equations for the wind gradients in *u* and *v* components is [40]:

$$\frac{\partial u_g}{\partial z} = -\frac{g}{f\,T}\left[\left(\frac{\partial T}{\partial y}\right)_z + \frac{\partial T}{\partial z}\left(\frac{\partial z}{\partial y}\right)_p\right] \tag{16}$$

and

$$\frac{\partial v_g}{\partial z} = \frac{g}{f\,T}\left[\left(\frac{\partial T}{\partial x}\right)_z + \frac{\partial T}{\partial z}\left(\frac{\partial z}{\partial x}\right)_p\right] . \tag{17}$$

Starting from one known wind level, in this case the GFS model surface wind, the full wind profile is calculated by applying Equations (16) and (17) to each layer in

sequence, adding the change in wind component through the layer to the value at the previous level. This technique performs better when calculating total wind speed than wind direction. Surface friction effects can cause rotation of the wind vector that is not reflected in the temperature data. Analysis of how consistent and accurate the AIRS-derived wind profiles are is presented in Section 4.2.1. Figure 18 and Figure 19 show example AIRS-derived wind profiles, compared to the corresponding rawinsonde observations (RAOB) profiles.

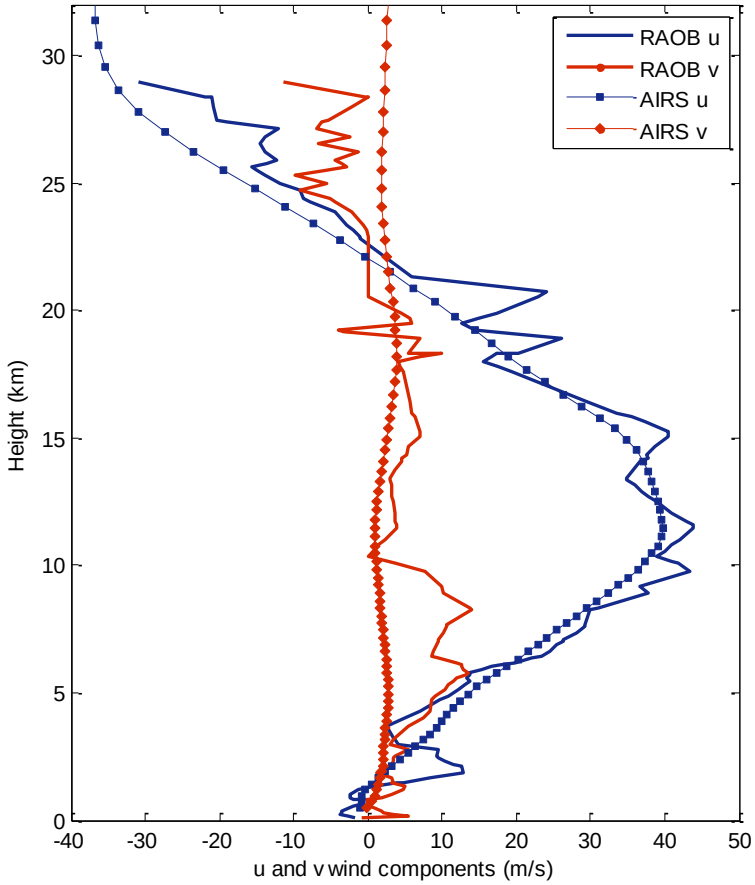

Figure 18. Comparison of AIRS-derived and RAOB *u* and *v* wind components for 11 Apr 2014 1250 UTC, Anchorage, AK.

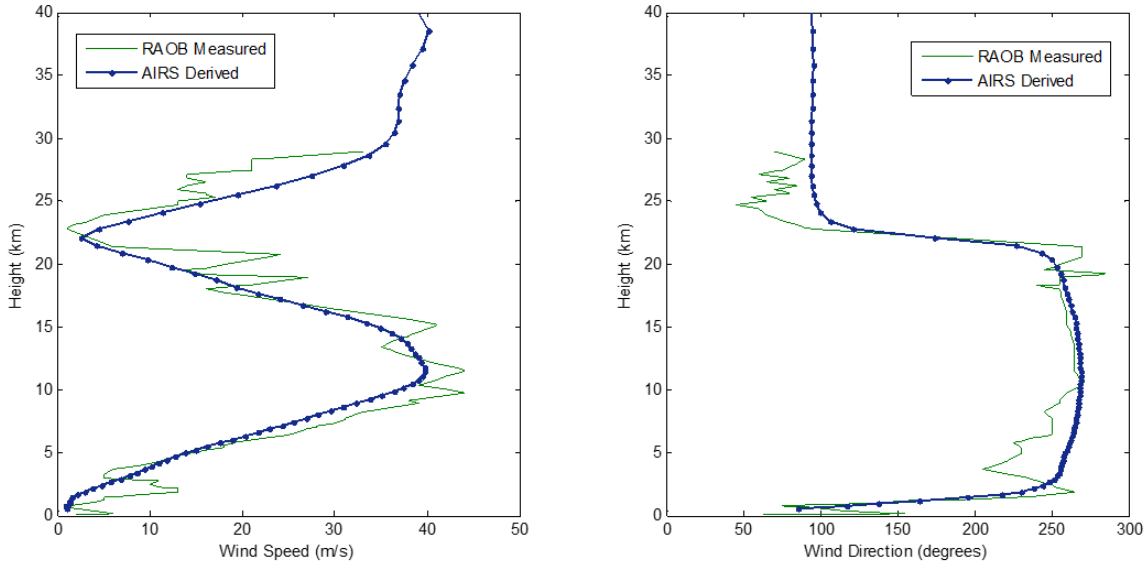

Figure 19. Comparison of AIRS-derived and RAOB wind speed and direction for 11 Apr 2014 1250 UTC, Anchorage, AK (same wind profile as Figure 18).

3.3 Calculation of the Index of Refraction Structure Function C_n^2

3.3.1 Relationship between C_T^2 and C_n^2

The AIRS instrument provides the 3-D temperature data needed for calculation of the temperature structure functions C_T^2 and C_n^2 for optical wavelengths. Using an expression derived by Tatarskii [35] [41] [42], C_T^2 can be determined by

$$C_T^2 = a^2 \alpha L_0^{4/3} \left(\frac{dT}{dz} + \gamma_d \right)^2 \tag{18}$$

where a^2 is an empirically determined constant, most often assigned the value of 2.8 [43] [44] [45] [46]. The outer scale length L_o is the largest scale of the atmospheric turbulence, or the upper bound of the inertial subrange. Values for L_o are reported throughout the range of "many meters to several tens of meters," but experimental measurements are scarce,

especially outside the planetary boundary layer [47]. Unless noted otherwise, L_o is estimated to be 100 m in this research. The dry adiabatic lapse rate γ_d is

$$\gamma_d \equiv \frac{g}{c_p} = 9.8 \times 10^{-3} K / m \tag{19}$$

where g is acceleration due to gravity at sea level, 9.81 m/s, and c_p is the heat capacity of air at constant pressure, 1005 J/kg K for dry air [5]. The term $\left({}^{dT}\!/_{dz} + \gamma_d \right)$ is the deviation between the temperature lapse rate and the dry adiabatic lapse rate, making it another way to express the vertical rate of change of potential temperature θ. Potential temperature is the temperature a parcel of unsaturated air would acquire if it were brought adiabatically to a standard pressure, usually 1000 hPa. Potential temperature can be calculated by

$$\theta = T \left(\frac{p_0}{p} \right)^{{}^{R_d}\!/_{c_p}} \tag{20}$$

where p_o is the standard pressure, 1000 hPa, and the ratio of the dry gas constant to the heat capacity of dry air, $R_d / c_p \approx 0.286$ [5].

The coefficient α in Equation (18) can be replaced by the ratio of eddy coefficients K_H and K_M by $\alpha \approx K_H / K_M$. K_H is the eddy diffusivity for heat, and K_M is the eddy diffusivity for momentum. The ratio of these eddy transfer coefficients, K_H / K_M, is also referred to as the inverse of the turbulent Prandtl number. By replacing α with this ratio, Equation (18) becomes

$$C_T^2 = a^2 \frac{K_H}{K_M} L_0^{{}^4\!/_3} \left(\frac{\partial T}{\partial z} + \gamma_d \right)^2 . \tag{21}$$

C_n^2 can be related to C_T^2 by [28] [35] [44]

$$C_n^2 = \left(\frac{\partial n}{\partial T} \right)^2 C_T^2 = \left(79 \times 10^{-6} \frac{P}{T^2} \right)^2 C_T^2 \ . \tag{22}$$

The numerical coefficient 79×10^{-6} in Equation (22) is appropriate for pressure measured in hPa and temperatures in K. This coefficient is wavelength dependent, and the value 79×10^{-6} is commonly selected because it corresponds to the middle of the visible optical range. The value would be 82.9×10^{-6} at 300 nm and 77.4×10^{-6} at 700 nm [35].

Combining Equations (21) and (22) yields the initial method for calculating C_n^2 employed in this research, which will be referred to in this document as the traditional Tatarskii approach:

$$C_n^2 = 2.8 \frac{K_H}{K_M} \left(79 \times 10^{-6} \frac{P}{T^2} \right)^2 L_0^{4/3} \left(\frac{\partial T}{\partial z} + \gamma_d \right)^2 \ . \tag{23}$$

3.3.2 Gradient Richardson Number

The gradient Richardson number, R_i, indicates the dynamic stability of the atmosphere and gives insight into turbulence production. It is the ratio of buoyancy forces (the numerator is the square of the Brunt-Väisälä frequency) to inertial accelerations (the denominator is the square of the vertical shear in the horizontal wind). It can be calculated from the vertical gradients in potential temperature and wind speed, previously derived from AIRS temperature data using [26] [34] [48] [49]

$$Ri = \left(g \frac{\partial \ln \theta_v}{\partial z} \right) \Big/ \left(\frac{\partial |V|}{\partial z} \right)^2 \ . \tag{24}$$

In Equation (24) θ_v is the virtual potential temperature, z is the geometric height, and V is the magnitude of the horizontal wind. The Richardson number is a measure of the stability of the flow, with larger values corresponding to stable, laminar flow. When the Richardson number exceeds a critical value, usually reported to be near 0.2 or 0.3, turbulent flow becomes laminar [21] [47] [50]. Table 2, reproduced from [34], identifies typical gradient Richardson numbers for various conditions of static stability and flow type.

Table 2. Values of the gradient Richardson number for different static stability and flow conditions, reproduced from Avila and Vernin [34].

$\partial\overline{\theta_v}/\partial z$	**Static Stability**	**Ri**	**Flow**
> 0	stable	> $Ri_{critical}$	laminar
> 0	stable	0 < Ri < $Ri_{critical}$	turbulent
< 0	unstable	< 0	convective (turbulent)

The eddy diffusivity ratio, K_H/K_M, can be approximated from the gradient Richardson number by [51]:

$$\frac{K_H}{K_M} = \frac{1}{7R_i} \quad \text{for } R_i \geq 1 \tag{25}$$

and

$$\frac{K_H}{K_M} = \frac{1}{6.873R_i + \dfrac{1}{1+6.873R_i}} \quad \text{for } 0.01 < R_i \leq 1\ . \tag{26}$$

3.3.3 Application of the Traditional Tatarskii Approach to AIRS Data

This C_n^2 calculation process has been previously applied to Numerical Weather Prediction (NWP) model data. Alliss and Felton used the WRF model to generate C_n^2 climatology over the Hawaiian Islands in 2009 [44] [45], but the techniques developed to apply the process to satellite sounding data, where the required temperature, pressure, and wind information is all passively collected from space, has not been found in the literature on the subject. An example of a C_n^2 profile calculated by applying this process to AIRS temperatures and derived winds is shown in Figure 20. Additional results and analysis of the technique are found in Section 4.3.

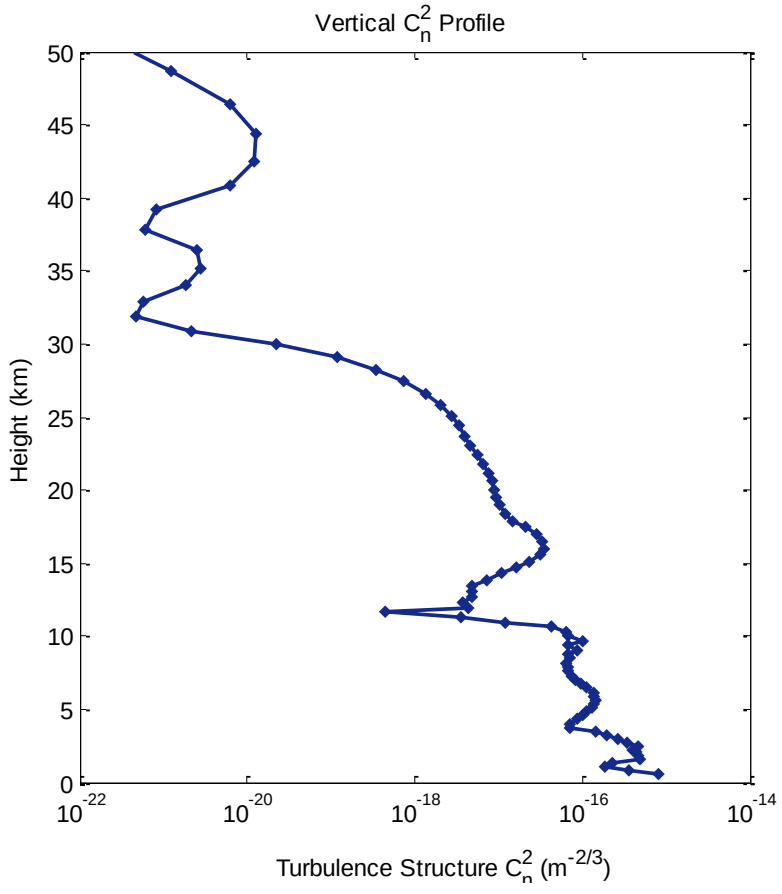

Figure 20. AIRS-derived C_n^2 profile - 11 Apr 2014 1250 UTC, Anchorage, AK.

3.4 Cloud Location and Characterization

3.4.1 Determination of Cloud-Top Height using AIRS Data

An additional focus of this research is determination of the heights of cloud layers and tops. Clouds cover approximately 40% of the Earth's surface at any given time [52]. At wavelengths of interest for directed energy applications, direct transmittance through all but the thinnest of cloud layers is extremely low [2]. For this reason, it is essential to be able to identify whether a specified slant-range path through the atmosphere is cloud-free or not. A critical step in this direction is to identify the height of the top of the highest cloud layer at each sounding location, which is related to the greatest atmospheric pressure for which AIRS is able to retrieve a temperature. Satellite-based sounders provide the data necessary to both locate the extent of the cloud cover horizontally and determine the height of the highest layer. Thermal radiation emitted from heights below clouds is largely absorbed before reaching space, and the channels whose weighting functions are associated with those heights measure unrealistically cold temperatures. Figure 21 depicts an image of the cloud cover over the eastern United States from one of the Geostationary Operational Environmental Satellites (GOES), and Figure 22 shows plots of the AIRS cloud fraction and cloud top pressure for one 6-minute granule of data from an ascending pass about 10 minutes after the GOES data were collected. The left plot shows the AIRS-derived cloud fraction, the fraction of the nine included AIRS fields-of-view that are not cloud-free all the way to the surface. The right plot shows the atmospheric pressure for the AIRS standard layer containing the highest layer determined to be cloudy, allowing an estimate of the altitude of the top of the highest cloud layer.

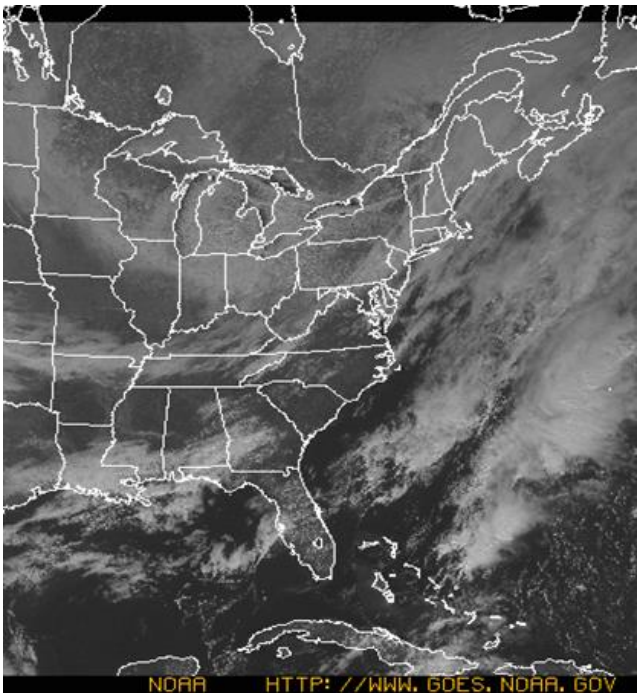

Figure 21. GOES-East image for 1815 UTC on 27 Jan 2014, retrieved from the NOAA Geostationary Satellite Server [53].

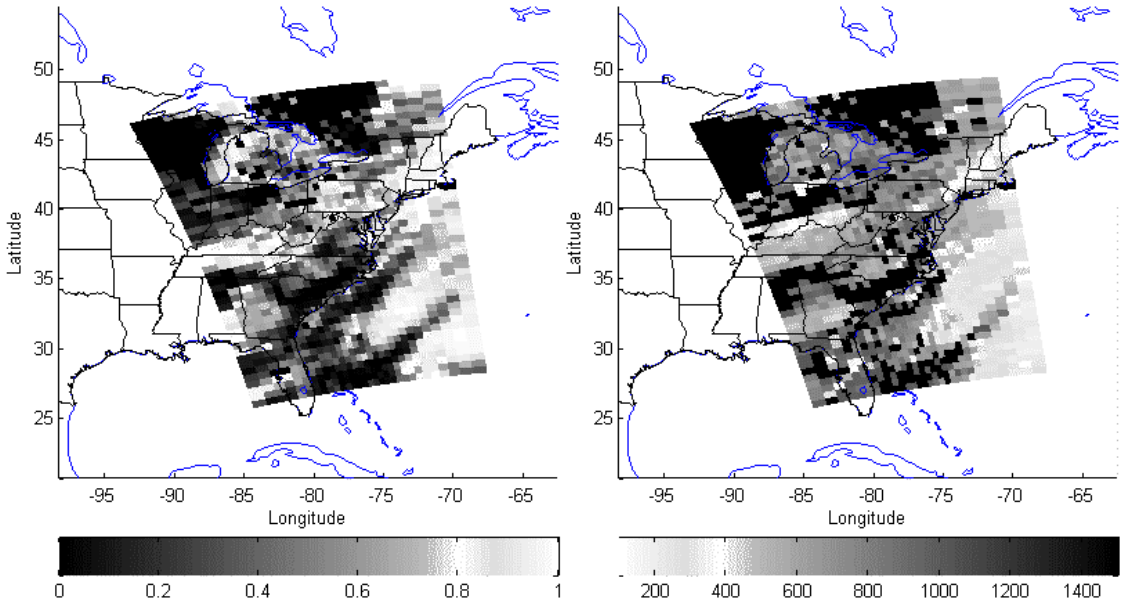

Figure 22. AIRS-derived cloud fraction (left) and cloud-top pressure in hPa (right). AIRS data collected between 1824 and 1830 UTC, 27 Jan 2014 [41].

A 3-D depiction of the cloud-top surface that results from assigning heights to the AIRS-derived cloud-top pressures is shown in Figure 23. Holes or missing data in the surface indicate regions that are cloud-free all the way to the surface [54].

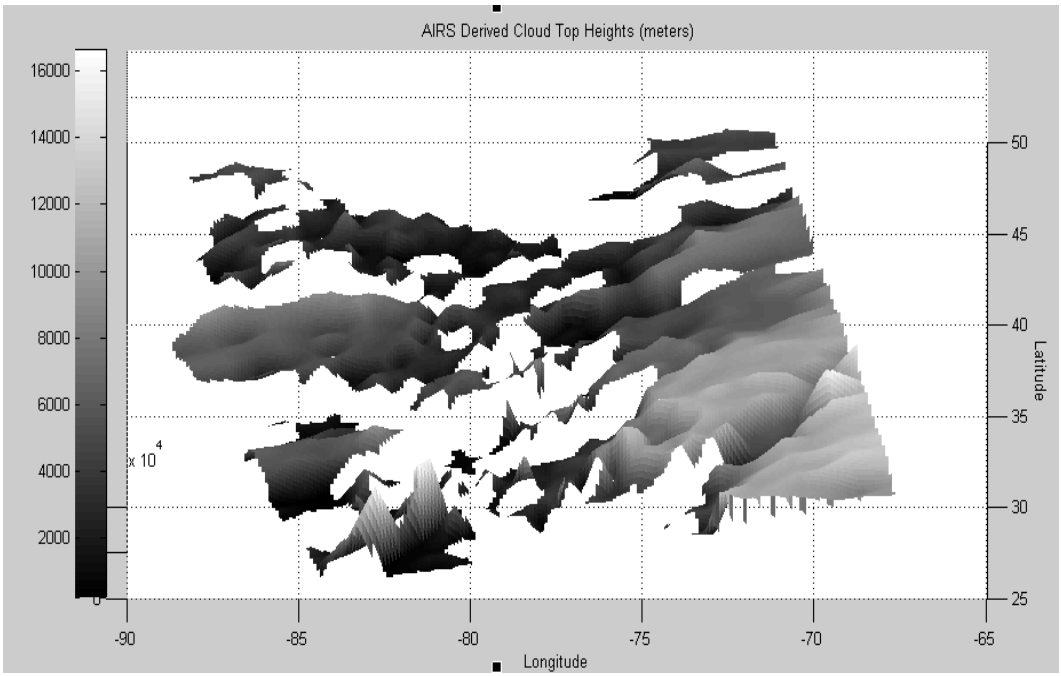

Figure 23. AIRS-derived cloud-top heights - 1826-1830 UTC, 27 Jan 2014.

3.4.2 Determination of Cloud-Top Height using MODIS Data

By incorporating data from a second A-Train instrument, cloud layer identification and top height calculation can achieve a level of accuracy and resolution that will make the near real-time cloud characterization useful for directed energy research and operations. MODIS data is available from the instruments onboard the Aqua and Terra satellites [55]. The 1 km horizontal resolution of the MODIS instrument can improve the determination of the horizontal extent of the cloud and better identify locations that are cloud-free all the way to the surface. Figure 24 shows the MODIS cloud products for the same geographic area and time period covered by the AIRS data in Figure 22 and Figure 23.

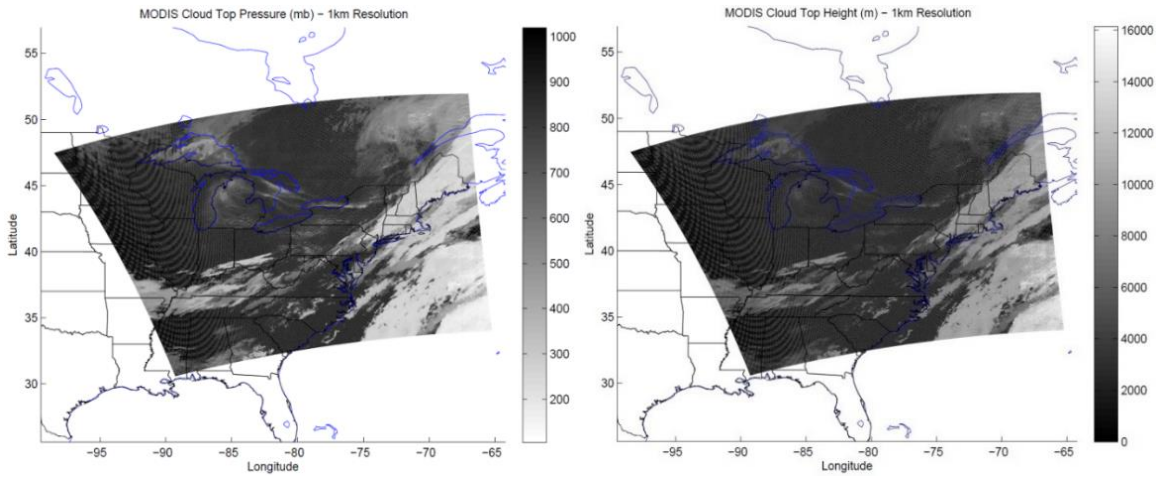

Figure 24. MODIS-derived cloud-top pressure in millibars (left) and cloud-top height in meters (right). Collected between 1825-1830 UTC, 27 Jan 2014.

Figure 25 shows a MODIS-derived 3-D depiction of cloud-top heights, similar to the AIRS-derived image shown in Figure 23. The improvement in horizontal resolution is clear, with the 1-km resolution better defining cloud-top shape and cloud-free regions.

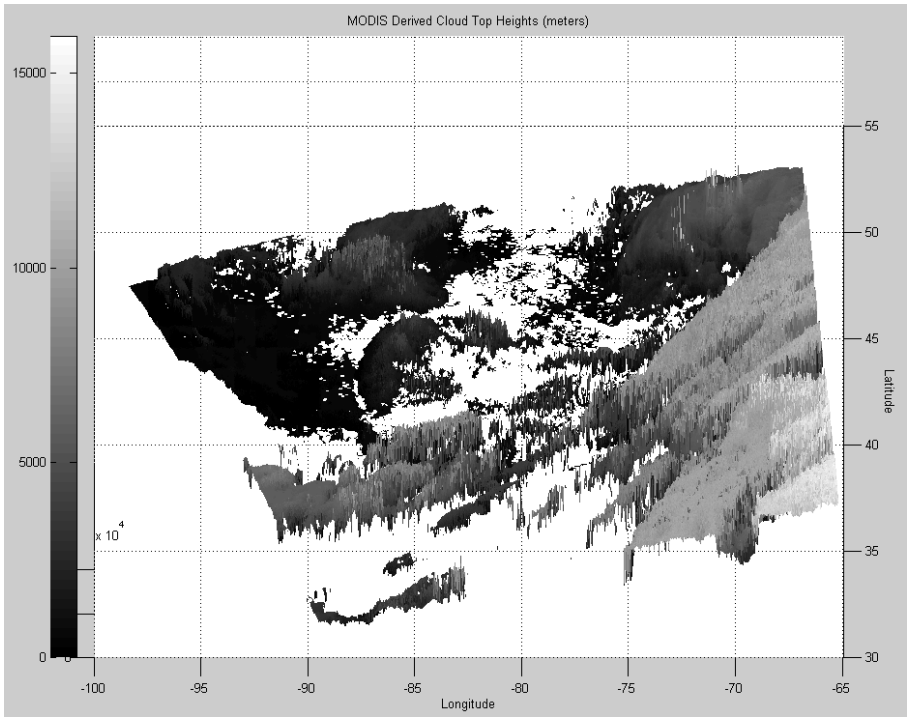

Figure 25. MODIS-derived cloud-top heights - 1825-1830 UTC, 27 Jan 2014.

By combining the AIRS and MODIS data sets, the excellent vertical resolution of the AIRS data can refine the cloud-top height assignment in the MODIS data while retaining the MODIS 1-km horizontal resolution. The improved cloud-top product could be used to determine expected cloud-free line of sight for an operational high energy laser (HEL) weapon system at a specified location and altitude.

3.4.3 MODIS Radiance Data as Verification Tool for Laser Environmental Effects Definition and Reference (LEEDR) Development

An additional application for the MODIS data processing techniques developed for cloud-top height determination is to obtain calibrated radiance values for each of the 36 MODIS channels. This ability is useful for ongoing efforts to improve AFIT's LEEDR modeling and simulation code. The LEEDR software package provides detailed atmospheric characterization, allowing users the ability to customize key parameters such as humidity profile and aerosol concentrations. The user is also able to define cloud layer heights and thicknesses, and select cloud types. The location, date, and time are input to determine sun angle. Once the atmospheric conditions are entered, LEEDR calculates wavelength dependent transmission, absorption, and scattering along any specified path through the atmosphere. Current improvements include a more robust code to model the complicated process of multiple scattering within cloud layers. The ability to compare LEEDR modeled upwelling radiance with calibrated MODIS measurements (available for any location, time of year, and cloud type) is proving invaluable during model refinement. Figure 26 and Figure 27 show a granule of MODIS radiance measurements, with seven locations selected to give a cross-section of cloud type, height, and layer thickness.

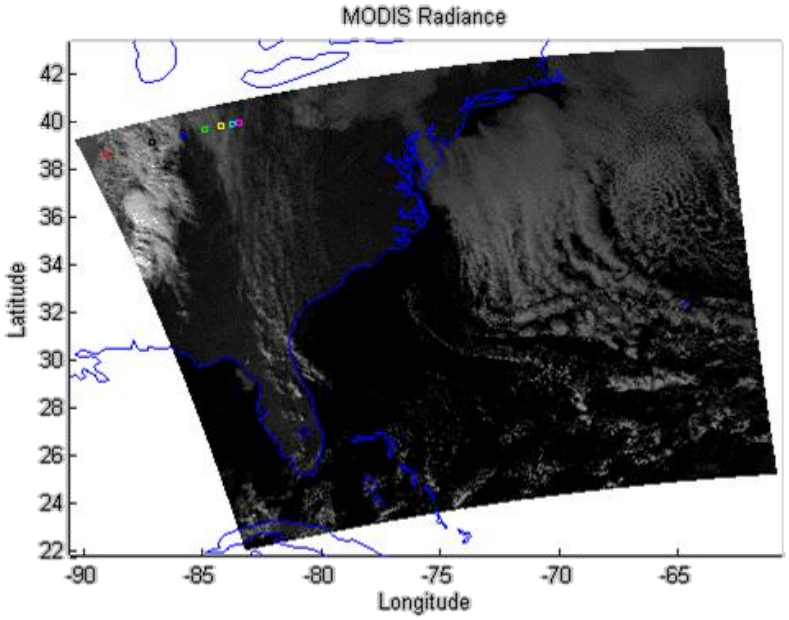

Figure 26. MODIS 1 km data granule. The seven squares in the northwest corner of the image correspond to the seven spectral radiance measurements plotted in Figure 27, providing a sample of several cloud-top heights and cloud types. Data collected 15 Dec 2014, 1815-1820 UTC.

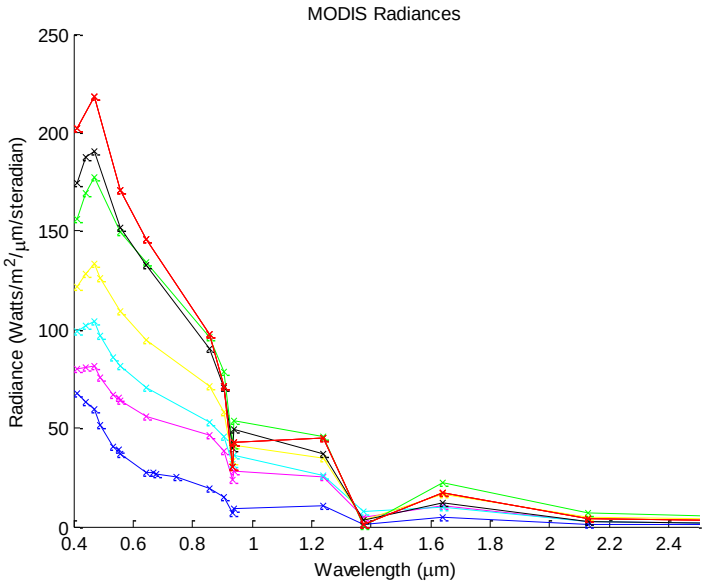

Figure 27. Calibrated MODIS radiance measurements. Each spectral radiance line corresponds to one of the MODIS fields-of-view identified in Figure 26.

3.5 Gap Filling with NWP models

The instruments onboard the polar-orbit A-Train satellites collect data for most locations twice a day, so there are 11-13 hour periods of time with no updates. There are two ways to overcome this problem. One way would be to exploit data collected from similar instruments on satellites in different orbits. For example, Aqua is not the only satellite with a MODIS instrument. The satellite Terra has an identical MODIS unit, and its orbit crosses the equator about three hours earlier than Aqua, giving many locations four overpasses a day and cutting in half the mean time between data collection.

A better and more operationally useful way to fill in these temporal gaps in satellite coverage is to take advantage of the output from NWP models. This research focuses on incorporation of output from the two models described in Section 2.4. The techniques developed in this work to calculate C_n^2 values are applied to temperature, pressure, height, and wind data obtained from the GFS model (both the 0.5 degree and 0.25 degree horizontal resolution) and the ECMWF model. Both of these global models have the ability to provide atmospheric data for any location of interest, but there is a big difference in how accessible the data are. GFS output is freely available to the public for download from NCEP. Access to ECMWF forecasts and recent model output requires an expensive license, limiting the number of organizations that can work with the data. The approach taken in this research is to utilize the publically available ERA-20C data which allows analysis using data with the same coverage and resolution as the forecast data. The ERA-20C data has the limitation that it only covers years 2010 and earlier.

The primary advantage to working with output from both the GFS and ECMWF models is that it allows comparison between a hydrostatic and a non-hydrostatic model.

Another reason is that it allows investigation into the effect increased resolution has on derived products. The ECMWF grid spacing of 0.125 degrees is half and one-quarter of the spacing between grid points in the two GFS models. Vertical coverage is another advantage of the ECMWF, with the top pressure level of 0.01 hPa this model generates output from the surface to heights above 75 km. In this research, NWP data are used in two different ways. The first method is to use NWP data only to fill in the temporal gaps between satellite overpass. In this method, the C_n^2 derivation technique being analyzed is applied to the satellite sounder data at the timesteps for which it is available, and to the NWP data at 3-hour intervals in between. This method allows the creation of C_n^2 profiles that extend for several days or weeks with enough data points to make useful comparison to scintillometer measurements.

The second way NWP data are used in this research is to apply the same C_T^2 and C_n^2 derivation techniques to data obtained by satellite sounder, NWP model, and rawinsonde when multiple sources are available for the same location at nearly the same time. This allows analysis of the performance of the C_n^2 derivation technique when applied to data sets with different spatial and temporal resolution, and it also allows for determination of the suitability of the various satellite sounder and NWP products to this type of optical turbulence research.

4 Results and Analysis

4.1 Validation of Satellite-Measured Temperatures

The technique for deriving winds through the thermal wind relationship as described in Section 3.2 relies on often very small horizontal temperature gradients, making it sensitive to any error in the underlying temperature data. Also, the full wind profile is constructed by adding each layer's wind gradients to the previous layer, which causes even small errors in measured temperature to compound and at times lead to large errors in wind speed and direction. For these reasons, additional analysis of the error in the AIRS temperatures is included as part of this research.

The error in AIRS/AMSU-measured temperatures varies with height, amount of cloud cover, and geographic location (which affects the IR and microwave sounding background). AIRS reported error is largest in the upper atmosphere, where the air density is much lower [56], but rawinsonde observation (RAOB) temperatures are not available for comparison at these altitudes, as the weather balloon does not typically survive past an altitude of 25-30 km. The height dependence in the AIRS-reported error can be seen in Figure 28, which plots an AIRS temperature profile against the rawinsonde measured temperature profile for the 1200 UTC release at the Anchorage, AK station. The AIRS profile is for the field-of-view closest to the rawinsonde release coordinates as the satellite passed over Anchorage at 1408 UTC.

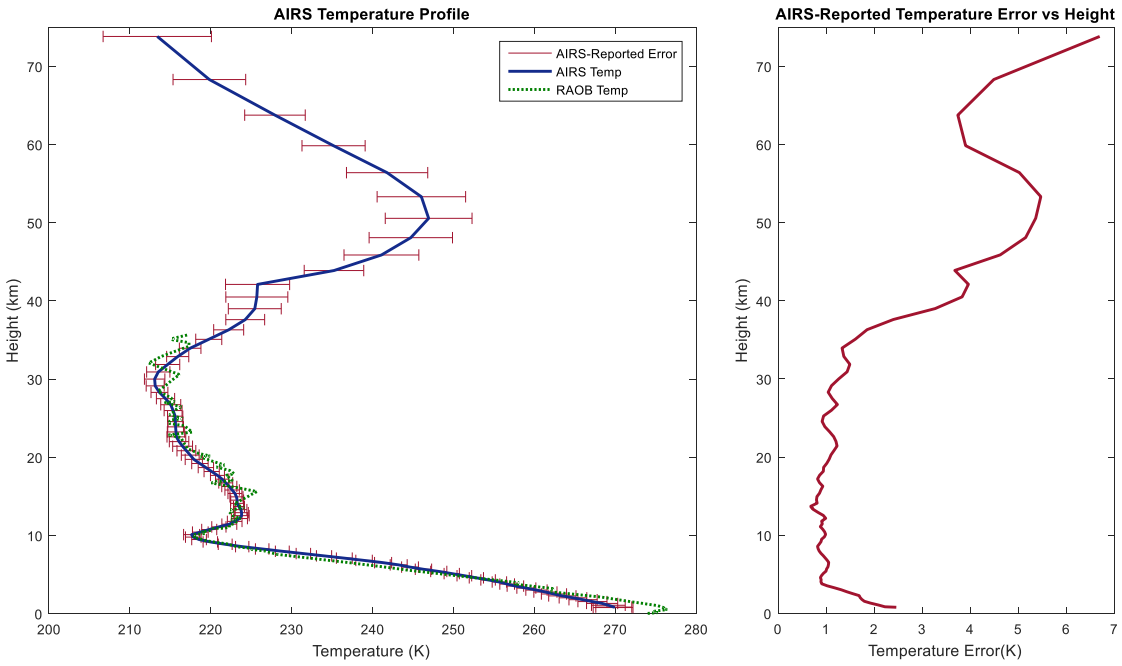

Figure 28. Anchorage, AK comparison of rawinsonde observation and AIRS temperatures–15 Oct 2014, 1408 UTC. In the left plot, the size of the error bar at each AIRS height indicates the magnitude of the temperature error reported with the AIRS level 2 data. The green dotted line shows the temperature measurement made by a rawinsonde released at the Anchorage International Airport two hours after this AIRS overpass. The right plot shows the magnitude of the AIRS-reported error as a function of height.

For the temperature accuracy study, four locations in Alaska and Hawaii were selected due to their scheduled 0000 UTC and 1200 UTC rawinsonde times closely matching the AIRS overpass times. For each of these locations, all AIRS data for the 12 year period 2003-2014 were processed, and when the overpass time for the sounding location nearest to the rawinsonde site was within 1 hour of the rawinsonde release, the temperature profiles were compared. The results of this analysis are presented in Figure 29 and Figure 30.

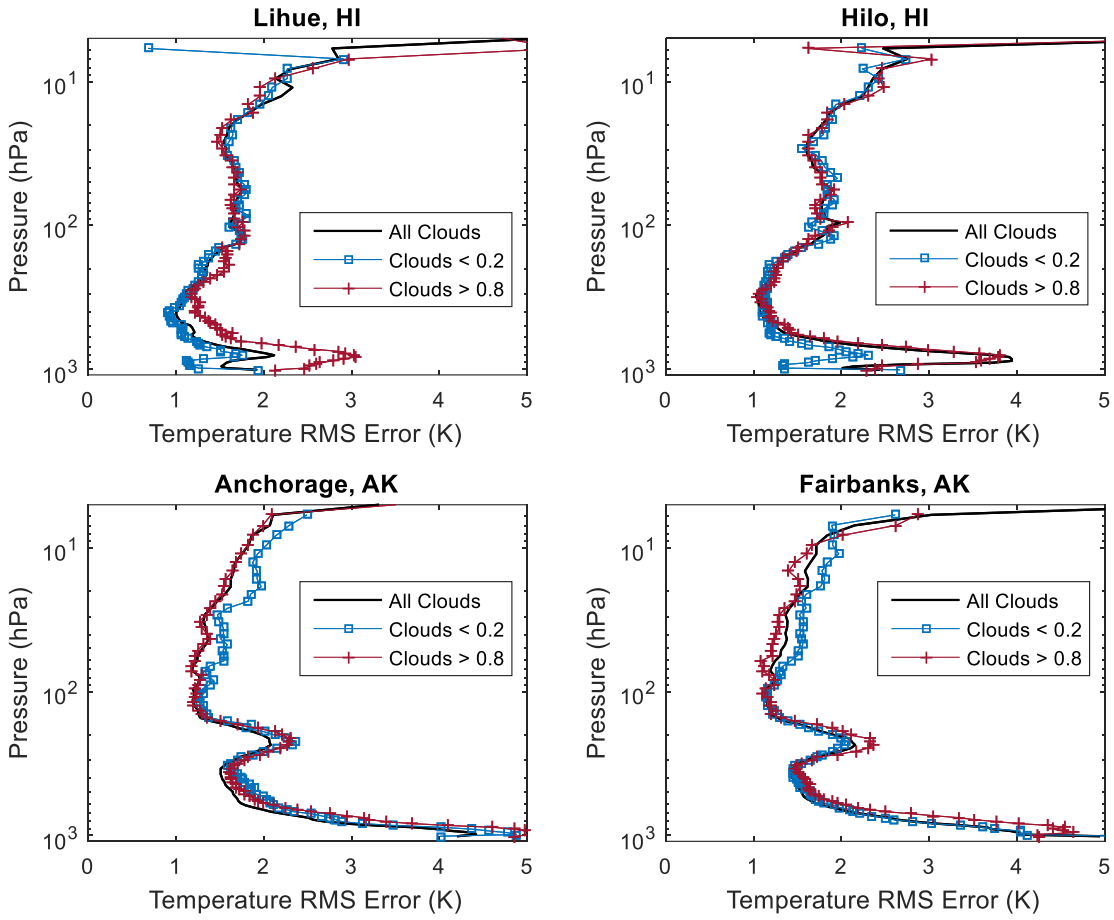

Figure 29. Root-Mean-Square (RMS) error between AIRS and rawinsonde measured temperatures for four locations selected for frequent AIRS overpass near time of 0000 UTC and 1200 UTC rawinsonde release. For 12 years of AIRS data (2003-2014), each instance when the AIRS overpass time was within 1 hour of the rawinsonde release is included. This figure includes data for 7519 match-ups for Lihue, HI, 7358 for Hilo, HI, 6792 for Anchorage, AK, and 6414 for Fairbanks, AK.

The differences between the AIRS-retrieved temperatures and the rawinsonde measurements are greatest in the lower atmosphere (below 700 hPa) and in the upper atmosphere (above 20 hPa). In the region between 20 hPa and 700 hPa the RMS error is between 1.0 and 2.5 K for each location.

In the lower atmosphere the satellite-retrieved temperatures were most accurate for locations with low or no cloud cover, as the resolution of the AIRS sounder outperforms the AMSU instrument. A different effect was observed in the upper atmosphere for the two locations in Alaska. For heights above the 100 hPa level, the temperatures for cloud-covered locations were a better match to the rawinsonde measurements than the cloud-free locations were. This effect could be due to low cloud cover providing a more uniform background for the IR sounder or it might identify the presence of optically-thin cirrus clouds which are not recognized by the AIRS cloud detection algorithm. This effect is not present in the Hawaii locations, as much of the AIRS field-of-view is water when the location is cloud-free. Further investigation including additional locations and cloud conditions is required to investigate the cause of this effect.

Figure 30 identifies a different sounding background issue with the AIRS temperature profiles. In both Alaska locations, there is a strong cold temperature bias in the data for the few pressure levels closest to the surface. In both cases there are multiple levels near the bottom of the profile for which more than half of the sampled temperatures are colder than the rawinsonde observation by more than 2 K. It seems this difference is probably a winter time effect, when at times a very strong temperature inversion exists within 500 m of the surface. A 2010 paper [57] on these surface-based inversions found that in Fairbanks in December and January, the air temperature at the surface is on average 10 K colder than the air temperature at a height of 1000 m. Due to the vertical spread of the weighting functions, the sounding channels near the bottom of the vertical profile would receive a contribution (in this case a reduction from the typical amount of radiance) from the cold surface and the first few hundred meters, which causes problems for the

process of assigning temperatures to the profile. This allows the cold surface to drag down the calculated temperatures for the neighboring levels. If that is the case, this effect should show up more in winter than in summer, so analyzing the seasons separately would help confirm or refute this explanation.

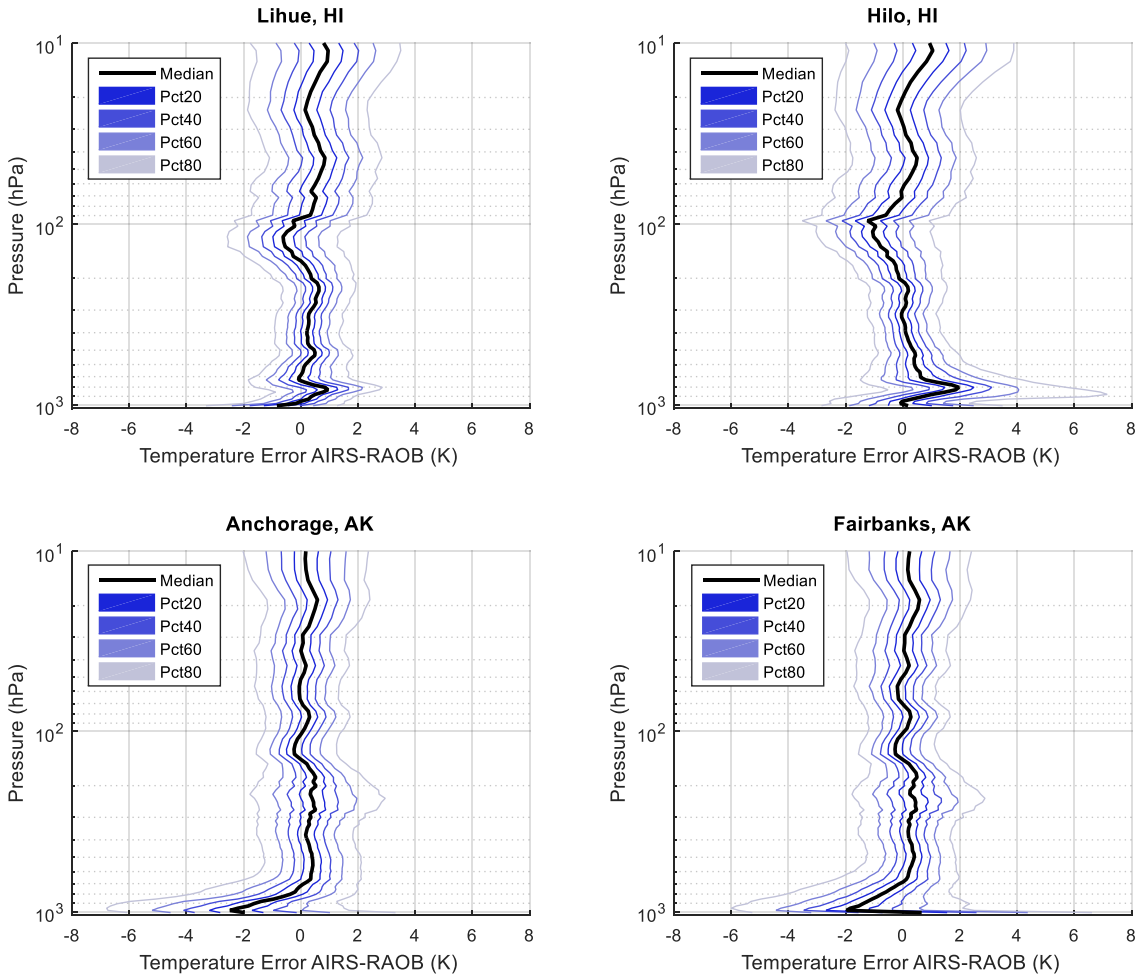

Figure 30. Temperature bias between AIRS and rawinsonde measured temperatures for four locations selected for frequent AIRS overpass near time of 0000 UTC and 1200 UTC rawinsonde release. These comparisons include the same 2003-2014 AIRS and rawinsonde data as Figure 29.

4.2 AIRS-Derived Winds

4.2.1 Accuracy of the AIRS-Derived Winds

A useful source of measured vertical profiles of wind speed and direction for use in analysis of AIRS-derived wind profiles is the network of rawinsonde observations [37]. These weather balloon soundings provide accurate wind data for hundreds of locations each day at 0000 and 1200 UTC. There are only two bands of longitude values for which the twice daily AIRS passes (early afternoon and early morning local time) are close to the time of the RAOBs. When they coincide, direct comparison of the wind profiles can be made, as shown in Figure 31.

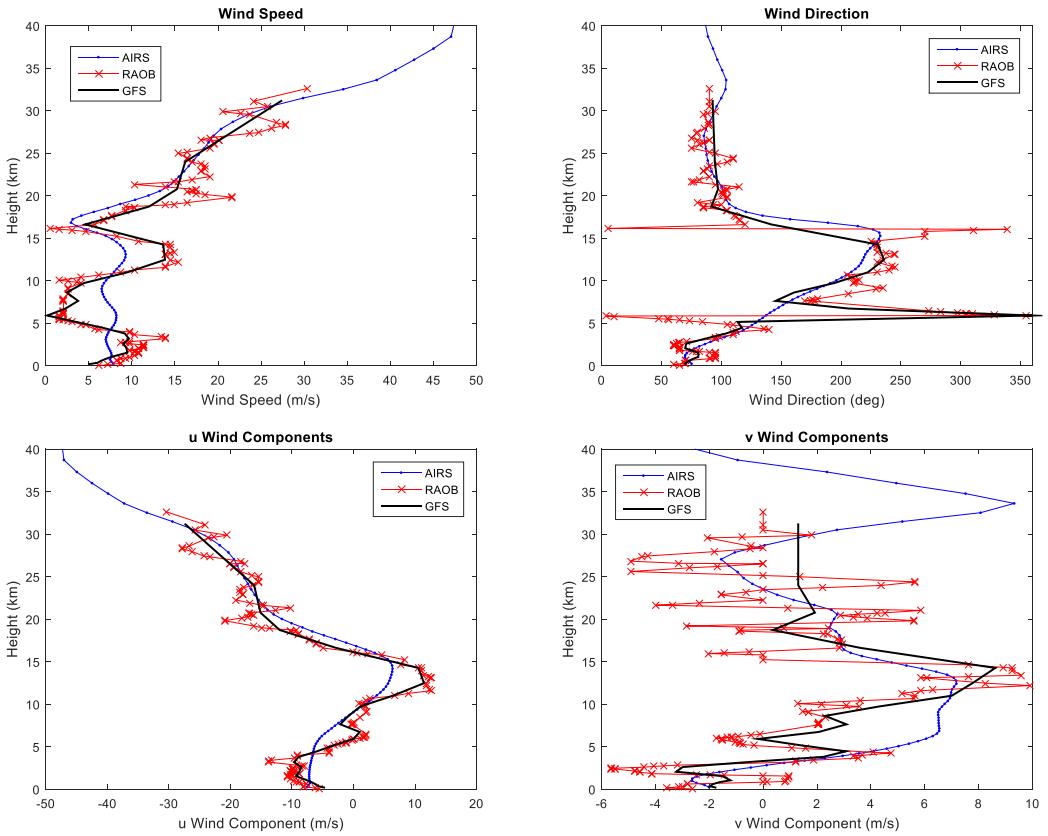

Figure 31. Comparison of AIRS-derived, RAOB-measured, and GFS-modeled wind profiles, Lihue, HI, 5 August, 2014, 0000 UTC.

Figure 31 also includes the corresponding NWP wind profile, in this case from the Global Forecast System (GFS) 0.5 degree model. This model is used because both the archived data and forecast data are widely available, making it a good choice for research and potential operational applications. GFS wind profiles do not match the vertical resolution of the RAOB, but typically provide an accurate representation of the trends in wind speed and direction. This makes it practical to use the GFS winds to evaluate the accuracy of the AIRS-derived winds, investigating locations and times of day for which no RAOB data are available.

A grid of 210 locations was selected in the Northern Hemisphere, covering the eastern Pacific Ocean and western portion of North America (at 5 degree latitude and longitude intervals). The geographic coverage of these sample sounding locations is shown in Figure 32.

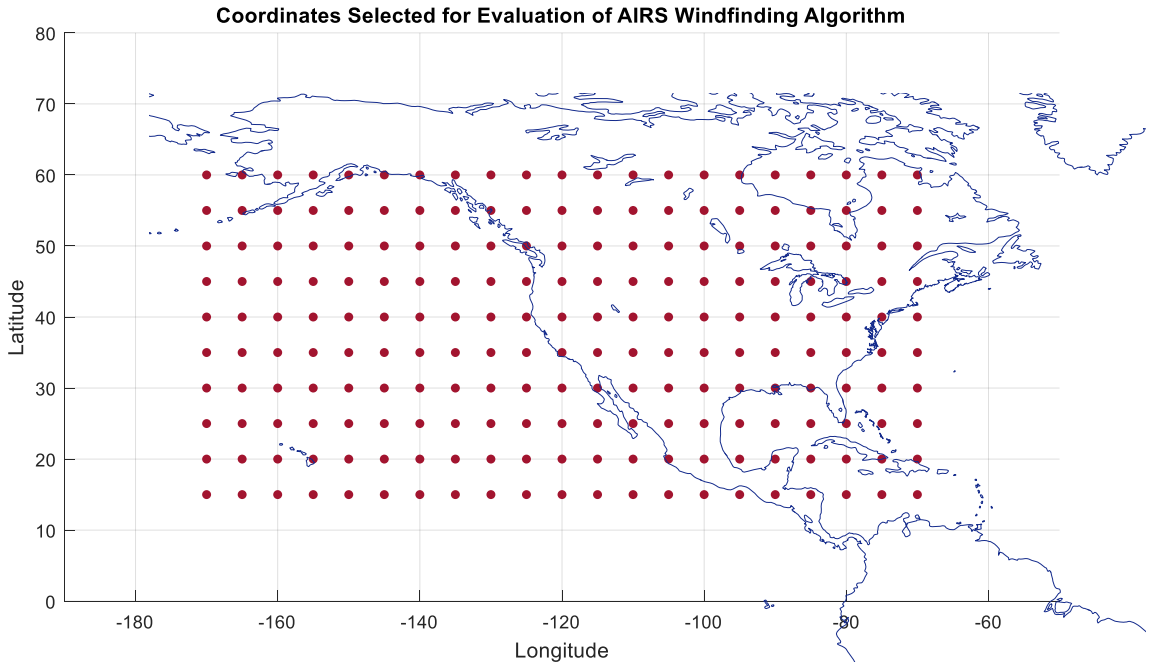

Figure 32. AIRS sounding coordinates selected for GFS comparison.

For each of the locations identified in Figure 32, 100 AIRS soundings were selected for download, one day and one night sounding per week throughout 2014. Corresponding GFS data for the nearest GFS grid point and closest 3 hour interval were retrieved for comparison. Of the possible 21,000 matches, 18,747 had both AIRS and GFS profiles available. These match-ups were used to investigate the conditions under which the AIRS windfinding technique worked best and which conditions led to the least accurate winds.

When calculating a wind profile, if the coordinates of interest fall near the edge of the AIRS swath, the temperature and pressure gradients used in the wind derivation technique may be less accurate because of missing neighboring AIRS data points. For this reason, it is expected that the AIRS winds should not match the GFS winds as well when the closest AIRS field-of-view is near an edge. Figure 33 shows the average of all wind speed profile RMS errors, plotted by corresponding AIRS field-of-view number.

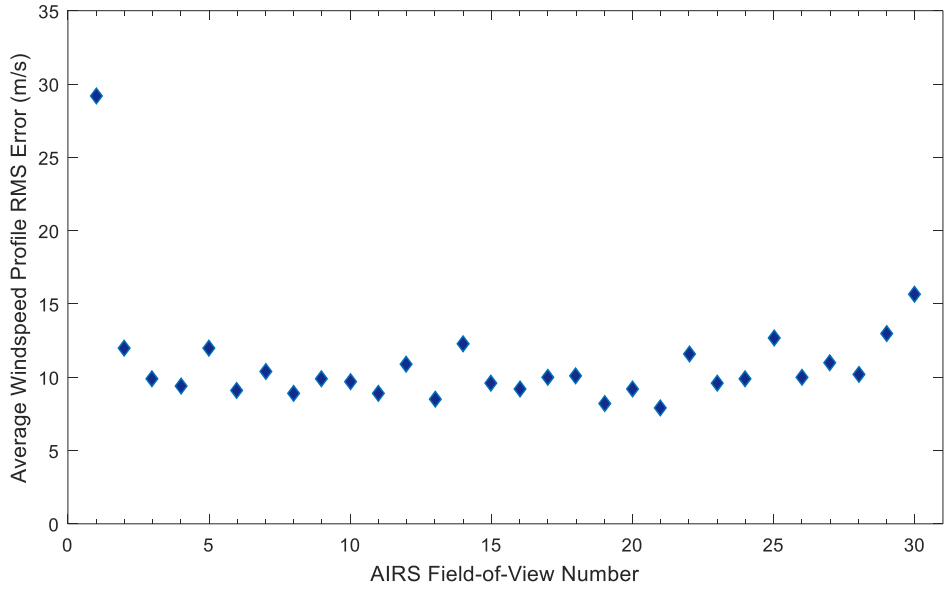

Figure 33. Wind speed profile error by AIRS field-of-view. The AIRS scan geometry is a left to right, whisk broom type, with each scanline comprised of 30 fields-of-view, numbered 1 through 30.

Field-of-view numbers 1 and 30 represent the left and right edges of the AIRS swath. AIRS wind speed was used for this comparison because it is more important for turbulence derivation than wind direction, but similar results are observed for *u* and *v* wind components individually. The least accurate results occur at the edges, but it appears that only the outer two fields-of-view are significantly impacted by this effect.

Time of day and time of year are additional factors that were investigated for their effect on the accuracy of the derived wind profile. Figure 34 and Figure 35 show the average RMS error values for all of the retrieved soundings, separated by month and whether it was the local afternoon sounding (day) or just after local midnight sounding (night). The over land soundings do not indicate any clear dependence on time of day or time of year.

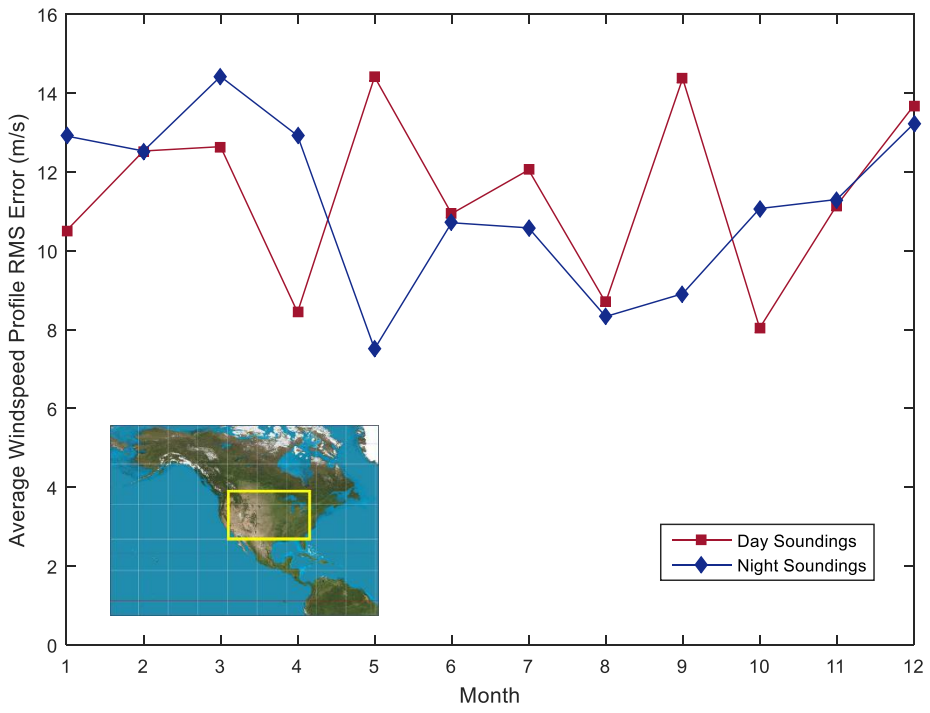

Figure 34. Average AIRS-derived wind speed RMS error for selected over-land soundings, plotted by month.

The over water comparisons in Figure 35 appear to reveal some seasonal variation in accuracy, evident in both the day and night sounding data. The RMS wind speed errors are greatest around April/May and smallest during August/September.

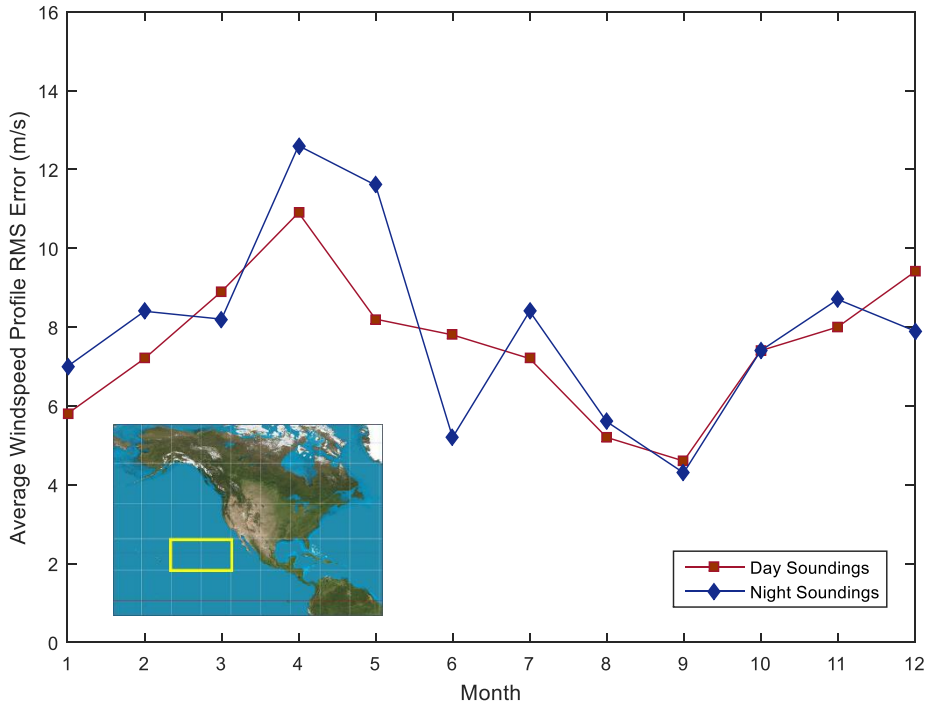

Figure 35. Average AIRS-derived wind speed RMS error for selected over-water soundings, plotted by month.

The most significant factor in how well the AIRS-derived wind profile agrees with the GFS wind is cloud cover. The atmospheric temperatures below clouds are not retrieved by the IR AIRS instrument—they are retrieved at reduced vertical resolution by the AMSU radiometer. These AMSU temperatures are used to complete the temperature profiles, and the reduced vertical resolution reduces the accuracy of the satellite-derived winds.

The AIRS reported cloud fraction for the soundings sampled ranged from completely clear (8.1%) to completely overcast (5.9%). To show this range, and the distribution of these cloud fraction values, a histogram is included as Figure 36.

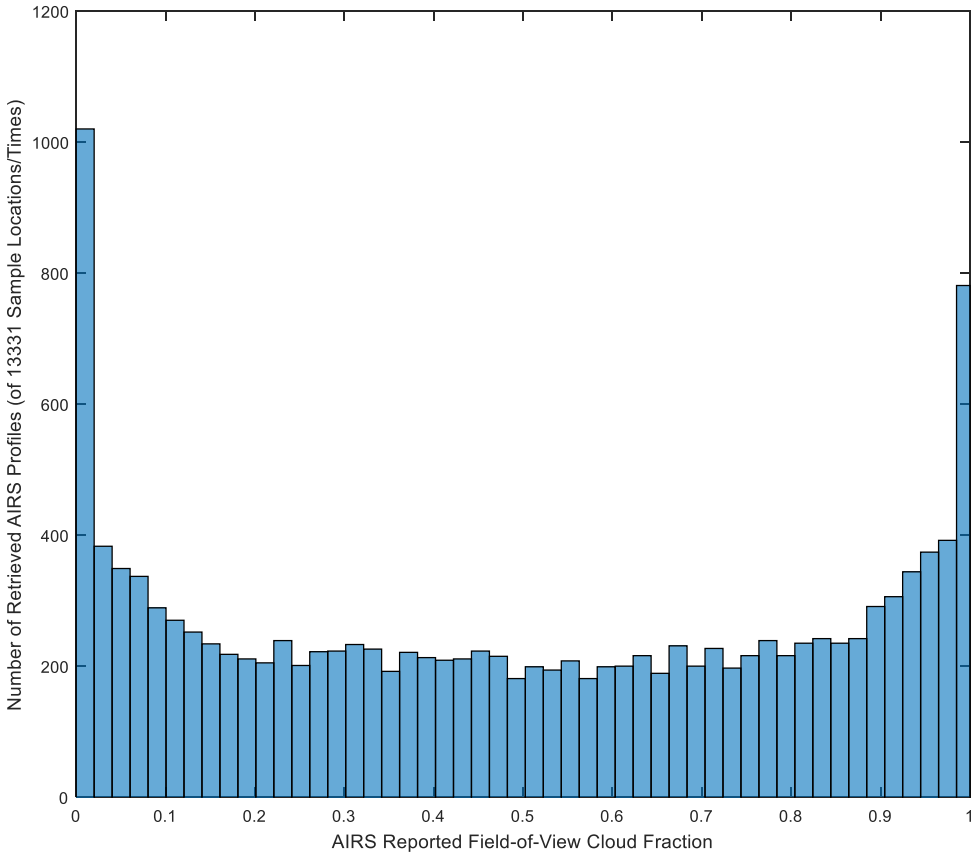

Figure 36. Histogram of AIRS reported cloud fraction values, the total effective cloud cover for all cloud layers within the AIRS field-of-view.

Each AIRS field-of-view is comprised of 9 separate IR soundings, and the total effective cloud fraction over all cloud layers for these 9 spots is determined by multiplying the cloud fraction for each field-of-view by the cloud emissivity. The assumption is made that the clouds are spectrally flat, and for a cloud that is partially transmissive, the equivalent opaque fraction is reported. This allows an effective cloud fraction value for each AIRS field-of-view to have any value between 0 and 1.0 [54] [58] [59].

As described in Section 4.1, cloud cover increases the error in the retrieved temperatures in the lower atmosphere. The increased error in the temperatures retrieved near the surface affects the accuracy of the winds in the lower atmosphere, which (because

of the way the wind profiles are constructed from the bottom up) increases the error throughout the profile.

This research shows that the portion of the AIRS field-of-view that is cloud obscured affects wind profile accuracy, with the worst average accuracy occurring when cloud fraction exceeds a value of 0.8. Figure 37 shows the average of all wind speed profile RMS errors within each bin plotted against corresponding cloud cover percentage, in 5% increments.

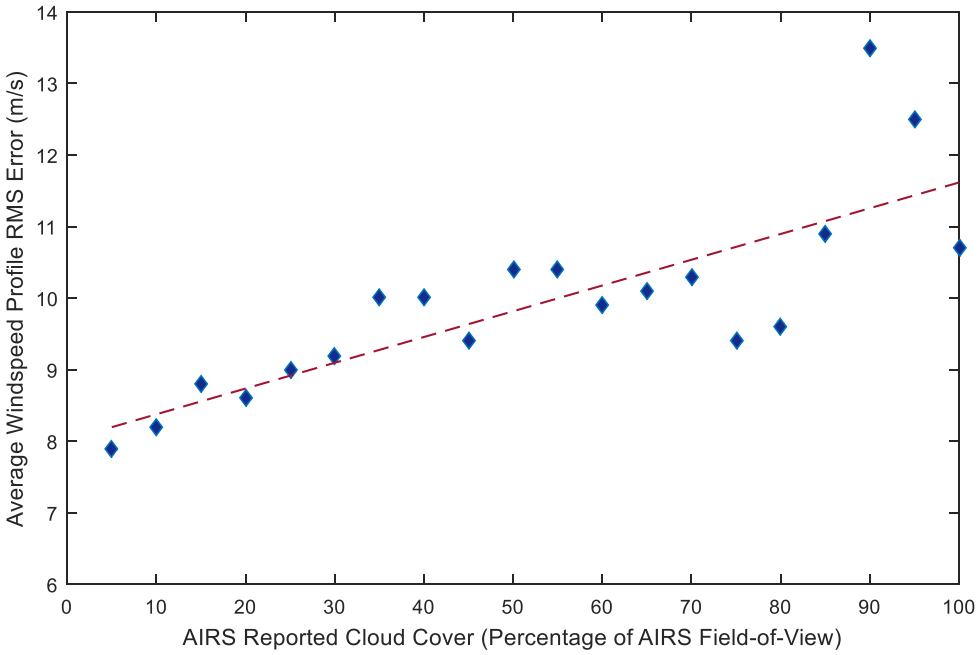

Figure 37. Average wind speed profile RMS error by AIRS reported cloud cover percentage for the 18,747 sampled AIRS soundings and corresponding GFS data points.

Figure 38 depicts the spread of these RMS errors throughout the range of cloud cover values, showing that the cloud cover effect on wind profile accuracy is small compared to the variability from one sample to the next.

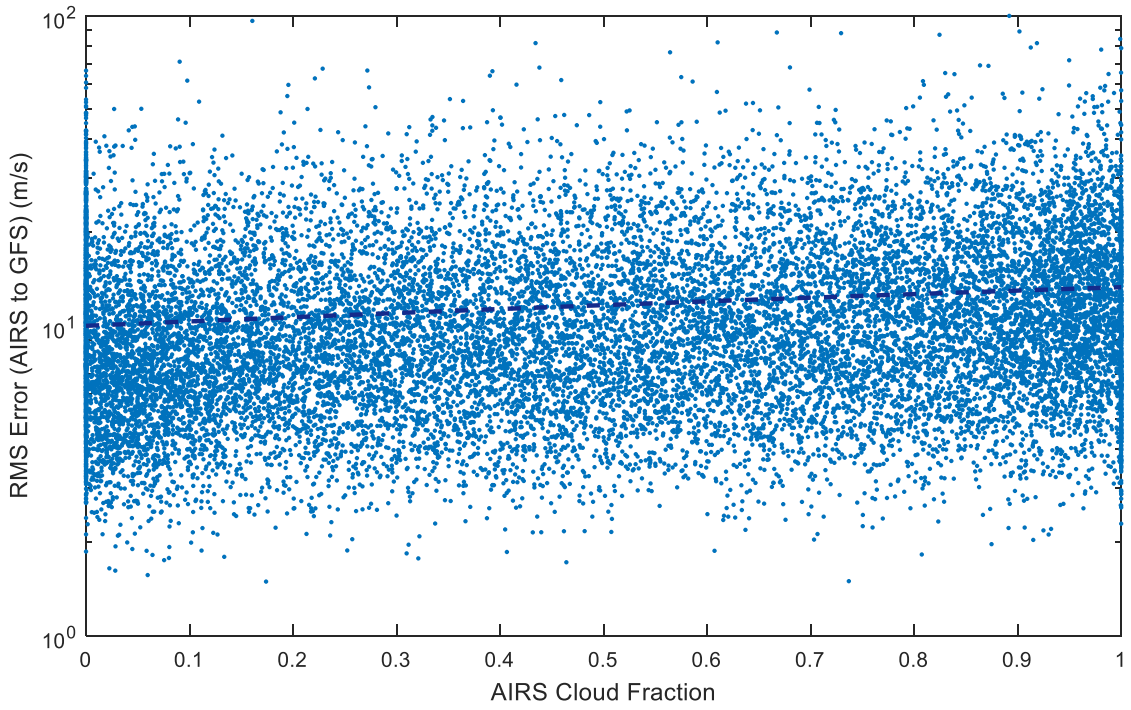

Figure 38. Wind speed profile RMS error by AIRS reported cloud cover percentage for the 18,747 AIRS soundings sampled.

Another important factor affecting the accuracy of the AIRS-derived wind profile is the surface type below the sounding. The AIRS weighting functions for many of the lowest altitude channels intersect the surface, and the emissive properties of the surface determine the amount of radiance contributed by the surface to that channel. Cloud cover has a larger effect on the AIRS/AMSU data over land than over water, because the included AMSU-derived data is more strongly affected by the varying surface emissivities found over land. Figure 39 shows that even when corrected for variations in cloud cover, the surface emissivity variation leads to reduced accuracy in regions where the sounder background is land.

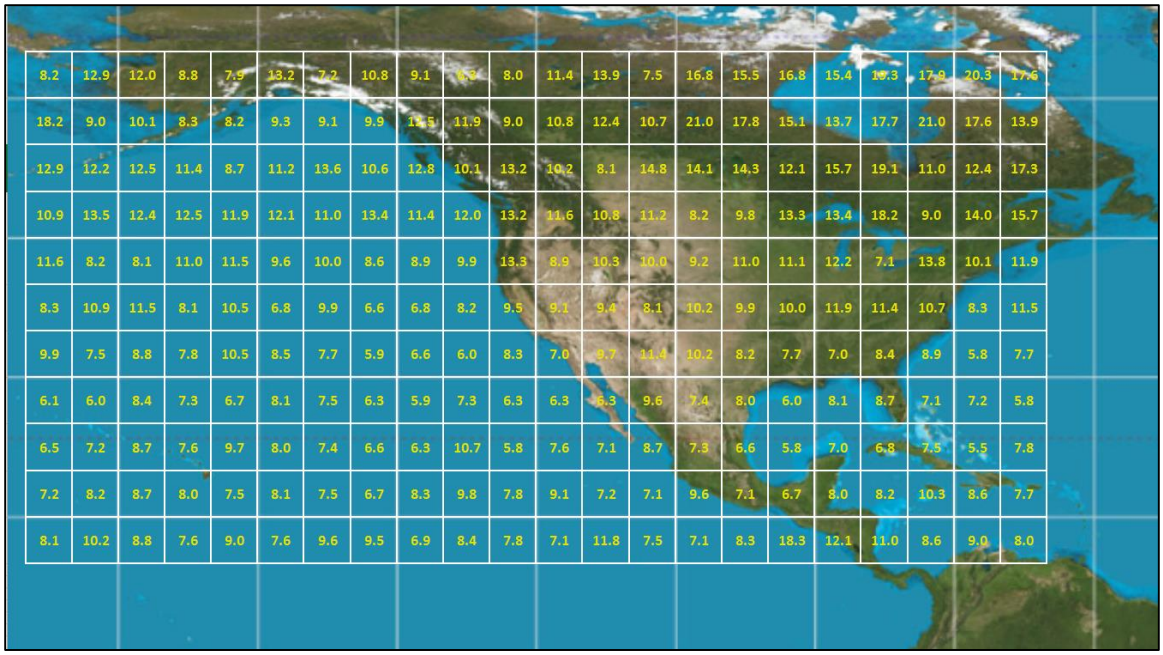

Figure 39. Average AIRS-derived wind speed profile RMS error (in m/s), compared with GFS wind profile for nearest grid point and time. In this figure, the RMS error for the wind profiles for each of the 5152 cloud-free or nearly cloud-free (AIRS cloud fraction across the field-of-view less than 0.2) AIRS soundings within each 5 degree by 5 degree box.

In Figure 39, only soundings with less than 0.2 cloud fraction are included. For these soundings, the average wind speed RMS error for the ocean only regions is 8.6 m/s. When land fills part of the box, the average RMS error is 11.2 m/s, 30% larger.

This technique of deriving winds from satellite sounding data has its operational advantages (passive sensing, single data source, and computationally inexpensive), but the accuracy of the resulting winds does not match the winds available from the NWP models investigated. When compared with rawinsonde measured winds, the AIRS wind profiles obtained often capture trends in wind speed and direction, but the satellite-derived wind profiles are typically not as accurate as winds provided by modern NWP models.

4.2.2 AIRS-Derived Winds in the Stratosphere

While not found to be suitable for low-altitude operational applications, the AIRS-based windfinding technique can provide wind information in regions of the atmosphere not currently covered by the GFS model. The AIRS data retrieves temperatures up to altitudes of 70-75 km (standard pressure level 0.0161 hPa), so derived wind profiles extend throughout the stratosphere and lower mesosphere, above the highest data available from most current NWP models. Direct measurements of winds in the upper atmosphere (heights unreachable by weather balloons) are infrequent and expensive. The ability to diagnose winds at these altitudes from satellite sounder data would be operationally useful.

The traditional way to obtain winds at altitudes between 40 and 80 km is to launch a rocketsonde. An example of this is illustrated in Figure 40, which shows the full AIRS-derived u and v wind profiles compared with wind components measured by a series of four Super-Loki/PWN 12A rockets deploying Rocket Balloon Instrument (ROBIN) Inflatable Falling Spheres. At altitude, each ROBIN sphere is inflated by evaporation of a contained liquid. It has an attached corner reflector, allowing it to be tracked by a precision ground-based radar as it falls through the atmosphere [60]. While it does not match the vertical resolution of the rocketsonde data in the stratosphere, the AIRS windfinding technique captures the wind component trends, providing some insight into the strength and direction of the wind at heights well above those modeled by GFS and other easily accessed NWP models.

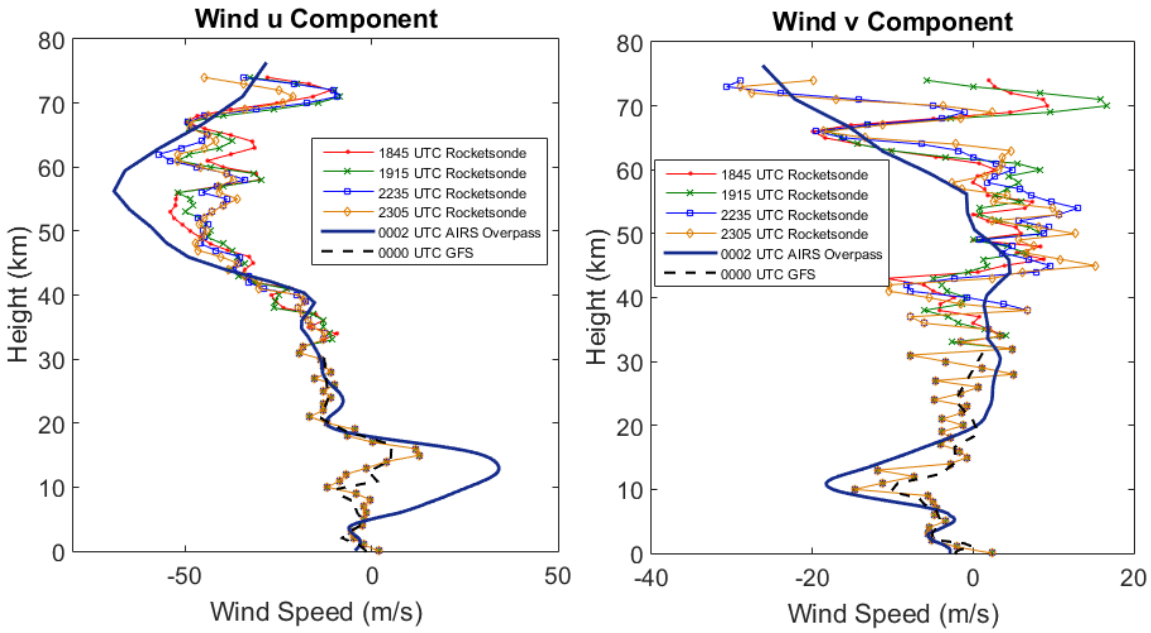

Figure 40. Comparison of the *u* and *v* wind component profiles derived from AIRS temperature data with winds measured by rawinsonde and by rocketsondes launched from the Pacific Missile Range Facility (PMRF) on 8 Jun 2015. The rocketsonde data was obtained through personal communications with Mary Bedrick, AFLCMC/XZIG, Wright-Patterson AFB and Dr. Clara O'Farrell, NASA JPL [61].

4.3 Calculation of Refractive Index Structure Function (C_n^2)

4.3.1 AIRS-Derived C_n^2 Profiles

One of the challenges with the AIRS-based C_n^2 derivation technique is the result of the nature of the AIRS temperature data. Temperature retrieval by IR sounding involves assigning a temperature to each altitude based on the radiance received on many channels. The weighting function for each channel defines how sensitive that channel is to radiance from each layer of the atmosphere. These weighting functions overlap each other vertically, and the radiation received by an individual channel emanates from a range of

altitudes. Through an iterative process, the temperature assigned to each level by the retrieval algorithm is based on the radiance received by many channels with weighting function peaks near the height of that level. This leads to an unavoidable smoothing of the temperature data—even when the AIRS temperatures match RAOB temperatures within a few K at every altitude, the weather balloon is able to detect temperature structure and variability over small vertical distances that are smoothed out by the satellite retrieval process.

This temperature smoothing leads to less variability than is present in directly measured wind profiles. Figure 41 shows an example of this smoothing in the left plot. In this example, the AIRS-derived wind speed agrees very well with the rawinsonde measurement, but the rawinsonde measures speed fluctuations of 5-10 m/s throughout the balloon's ascent. These fluctuations are not present in the AIRS wind profile.

When the AIRS-derived wind gradient is used to calculate the gradient Richardson number, the smoothing of the wind speed profile leads to a larger Richardson number. The right plot in Figure 41 shows a comparison between the Richardson numbers calculated from the AIRS and the RAOB data. The AIRS-derived values are between 1 to 2 orders of magnitude larger than the RAOB derived values for much of the profile. This higher gradient Richardson number leads to lower C_n^2 values, especially at heights where the smoothed wind speed reaches relative minima or maxima. If the wind speed does not change much from one level to the next (e.g., the levels between 11 and 12 km in Figure 41) the denominator of the Richardson number equation approaches zero, leading to a spike in Ri, and a corresponding proportional drop in K_H/K_M and C_n^2. This demonstrates that even though the sounder data has comparable vertical resolution and good temperature

accuracy (most of the temperature profile within 1.5 K of RAOB measured temperature), there are problems introduced by the fact that space-based sounding will always fail to measure temperature structure and fluctuations that occur on a scale smaller than 2 or 3 vertical data points. Missing the temperature variability has an impact on the wind profile, which affects the Richardson number almost exclusively in one direction—pushing Ri to larger values which leads to smaller C_n^2 values.

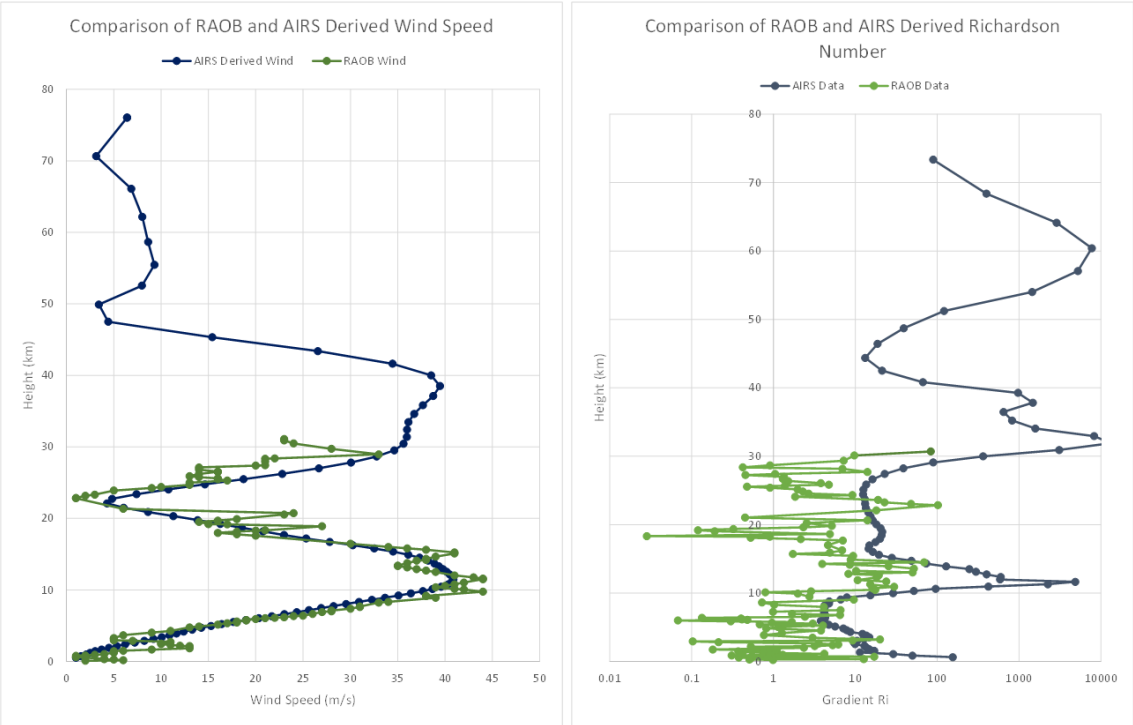

Figure 41. Smoothing of satellite data leads to large gradient Richardson numbers - 11 Apr 2014 1250 UTC, Anchorage, AK.

4.3.2 Use of NWP Winds with AIRS Temperatures to Calculate C_n^2

An alternative source of wind information, which avoids the accuracy problems with the AIRS-only winds, is NWP data. NWP winds match rawinsonde measurements more closely than the AIRS-derived winds do, so their use for C_n^2 calculation is expected

to yield better results. While not capturing all of the variability in component wind speeds over small vertical distances that are measured by a rawinsonde, GFS winds are not as smoothed as the AIRS-derived winds (see Figure 31 for an example). This difference leads to more structure in the C_n^2 profile, as seen in Figure 42, where the C_n^2 values calculated using GFS 0.5 degree model winds, obtained through the NOMADS server, are compared to an AIRS-only C_n^2 profile.

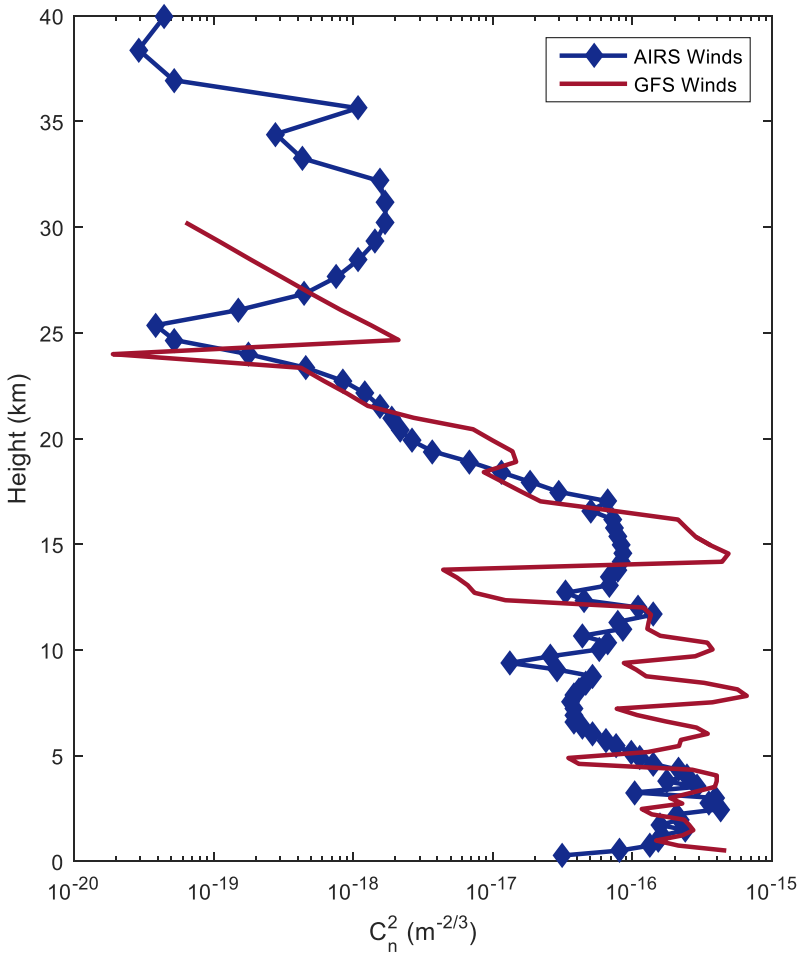

Figure 42. Comparison of C_n^2 profiles from AIRS-only technique and hybrid AIRS temperatures and GFS winds. This comparison is for Lihue, HI, 2 January 2013, 1800 UTC.

4.3.3 Creation of a Standard Maritime C_n^2 Model

The techniques developed in this research project provide the tools necessary to create a standard C_n^2 model for specific locations or conditions by calculating hundreds of profiles, across a range of different weather conditions, and averaging them. For each height, a mean C_n^2 value and the standard deviation can be determined. Even though C_n^2 values at a given location can vary greatly as atmospheric conditions change, at times by more than an order of magnitude from one minute to the next, a standard model is a useful engineering tool, providing a way to determine an envelope of expected performance for a directed energy system or sensor in a specified environment. The widely used C_n^2 model, Hufnagel-Valley 5/7 (previously presented in Figure 11), was developed to characterize optical turbulence (C_n^2) as it varies with height over land. While the H-V 5/7 model is not meant to predict precise values, observations will likely be in a range close enough to the model's prediction to make it a useful system design and planning tool. H-V 5/7 is not designed for, nor well-suited to, modeling turbulence over the ocean. Thus recent AFIT research, conducted by Lt Greg Anderson, has focused on the development of an H-V-like standard model of optical turbulence for a maritime atmosphere [62]. Maritime temperature climatology data collected by AIRS and wind data from the GFS model were used in the Tatarskii relationship as described in Section 3.3.1 to calculate over 29,000 C_n^2 profiles over the world's oceans. Three standard models were proposed as alternatives to the H-V model. Results showed that maritime profiles generally do not exhibit the surface spike in turbulence seen in H-V 5/7. Additionally, a strong latitudinal variation in the height of the C_n^2 inflection associated with the height of the tropopause is observed, motivating the need for separate models for polar and tropical regions.

For this research project, 40 maritime locations were selected, and for each of those locations, all available day and night AIRS soundings were collected for the entire year of 2013. The locations were selected to sample a range of global maritime atmospheres, and allow day-night, seasonal, and regional comparisons to be made. The 40 locations used to generate these standard C_n^2 profiles are shown in Figure 43.

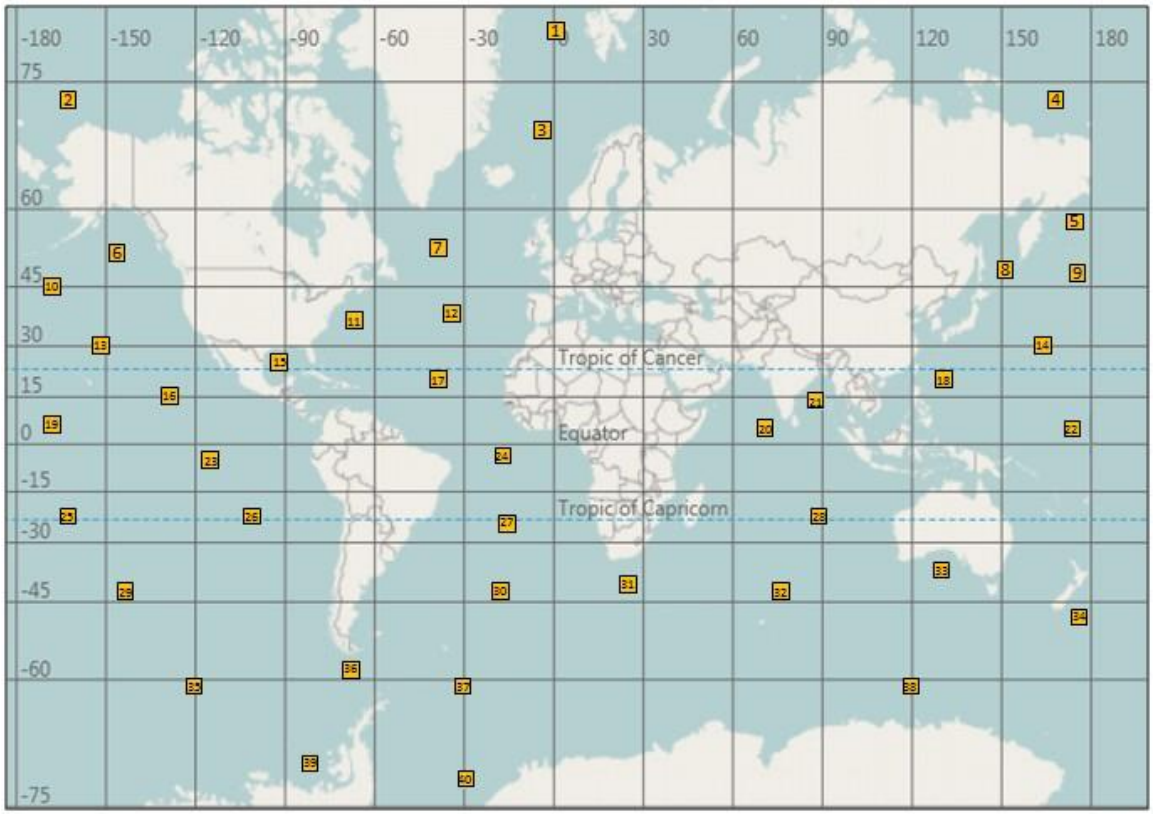

Figure 43. Satellite and NWP data were collected for 40 global, maritime locations, identified by the numbered markers in this figure [62].

A plot of the calculated and median daytime C_n^2 values for the month of April 2013, for a maritime location north of the state of Alaska is shown in Figure 44. The observed values represent every C_n^2 value calculated from the combined AIRS and GFS wind data available for this location during this time period.

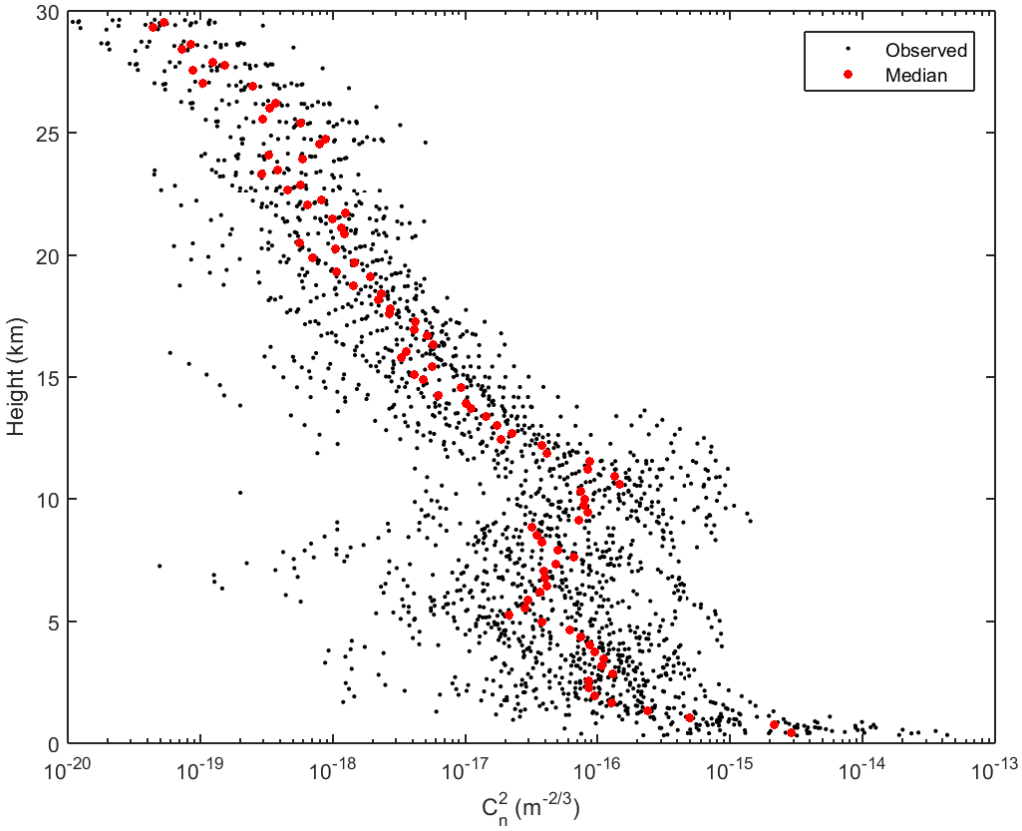

Figure 44. One month of daytime AIRS and NWP data derived C_n^2, April 2013. The location is identified as position 2 in Figure 43 [62].

This averaging process was expanded to include all 40 maritime locations and extended for the entire year of 2013. One example of the resulting standard C_n^2 models is a dynamic piecewise model, which is comprised of two C_n^2 profiles to account for the variability in tropopause height with latitude. Figure 45 shows this model (for polar and tropical regions), each plotted over the AIRS and NWP derived C_n^2 values for all of the selected locations and the entire 2013 time period of the study.

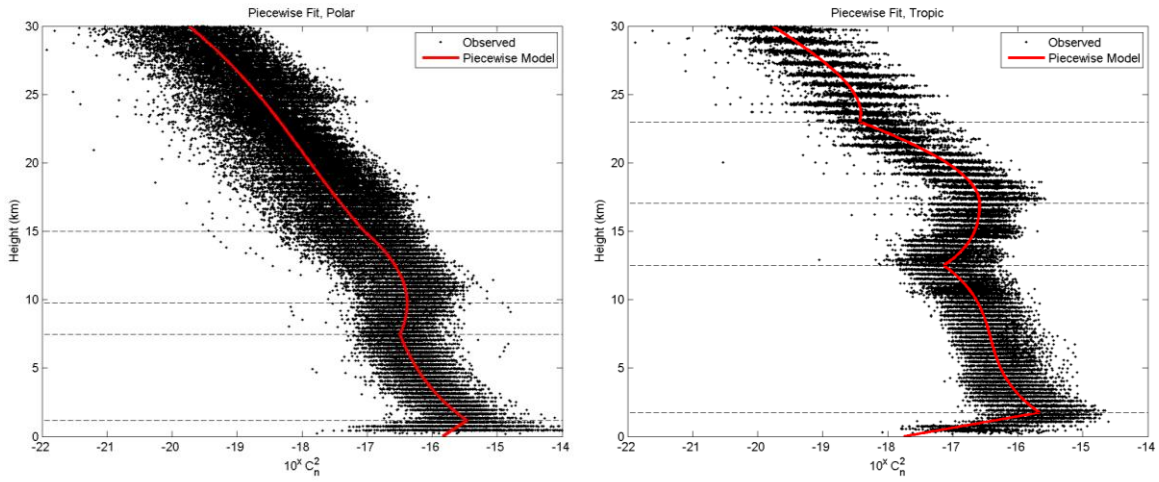

Figure 45. Dynamic piecewise polar and tropical model C_n^2 profiles [62].

The techniques used to create this maritime model rely on meteorological satellite and NWP data, exploiting the combination of AIRS atmospheric temperature data and NWP wind profiles. This combination provides an excellent data set for creating this type of standard C_n^2 profile, exploiting the vertical resolution of the AIRS instrument with the accurate horizontal wind speeds of an NWP model, GFS in this case. By further filtering the AIRS data, selecting a smaller geographic window, narrowing to a specific time of year, or separating day and night overpasses, this technique could be employed to develop custom, operationally relevant standard C_n^2 models to meet specific requirements. With over twelve years of AIRS data available, it is possible to obtain data from enough overpasses to generate a statistically significant sample size for narrow conditions. For example, a standard model generated using only daytime, winter soundings within 100 km of a single midlatitude location could still include data from more than 80,000 AIRS soundings during the 2002-2015 time period.

4.3.4 Derived C_n^2—NWP-Only

The availability of NWP data at three hour intervals, or even one hour intervals for some models recently put into operation, assures that for operational requirements below 30 km in height, forecast data are available within 90 minutes of any time of interest. NWP models provide all of the atmospheric parameters required to calculate C_n^2 using the traditional Tatarskii approach. One advantage of this NWP-only technique is the ability to forecast C_n^2 for a specified location in the future, something not possible if the calculation cannot begin until 30-60 minutes after the satellite passes overhead and the temperature data are processed.

The C_n^2 forecast could extend as far into the future as the underlying NWP model (10-16 days for GFS and 7 days for ECMWF), but of course the potential error in the forecast increases with the length of the forecast. Figure 46 shows example vertical C_n^2 profiles generated solely from NWP data. In this example, ECWMF 0.125 degree horizontal resolution data for a 20 x 30 degree geographic region covering the southeast United States are used to calculate both a profile for a single grid point and a mean profile for all profiles within the region.

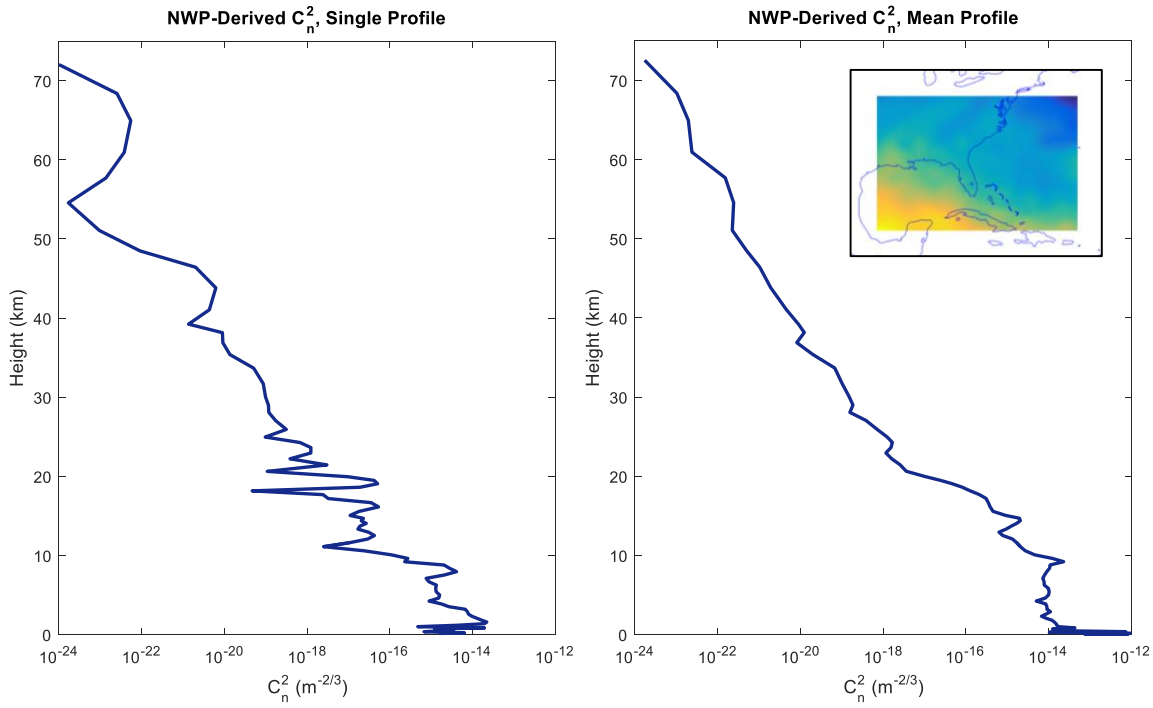

Figure 46. C_n^2 profiles for sample data set from the ECMWF ERA-20C re-analysis model for 1800 UTC, 1 Jun 2010. The left plot is for a single grid point at the northwest corner of the sampled data (40° N, 95° W), and the right plot is the mean C_n^2 value at each height for the 38,400 vertical profiles across the southeast United States and Gulf of Mexico (the geographic region depicted in the top right corner of the plot).

Figure 47 shows the range of derived C_n^2 values throughout this ECMWF data set. Throughout the vertical profile, 80% of the C_n^2 values fall within an envelope from about 1.5 orders of magnitude below to about 1 order of magnitude above the median value. These 38,400 profiles are all for the same time, for a 20° band of latitude, so they exhibit some common characteristics. For example, the bump in C_n^2 present in nearly all of the profiles between 13 and 15 km is indicative of the height of the tropopause at this time of year in this geographic region.

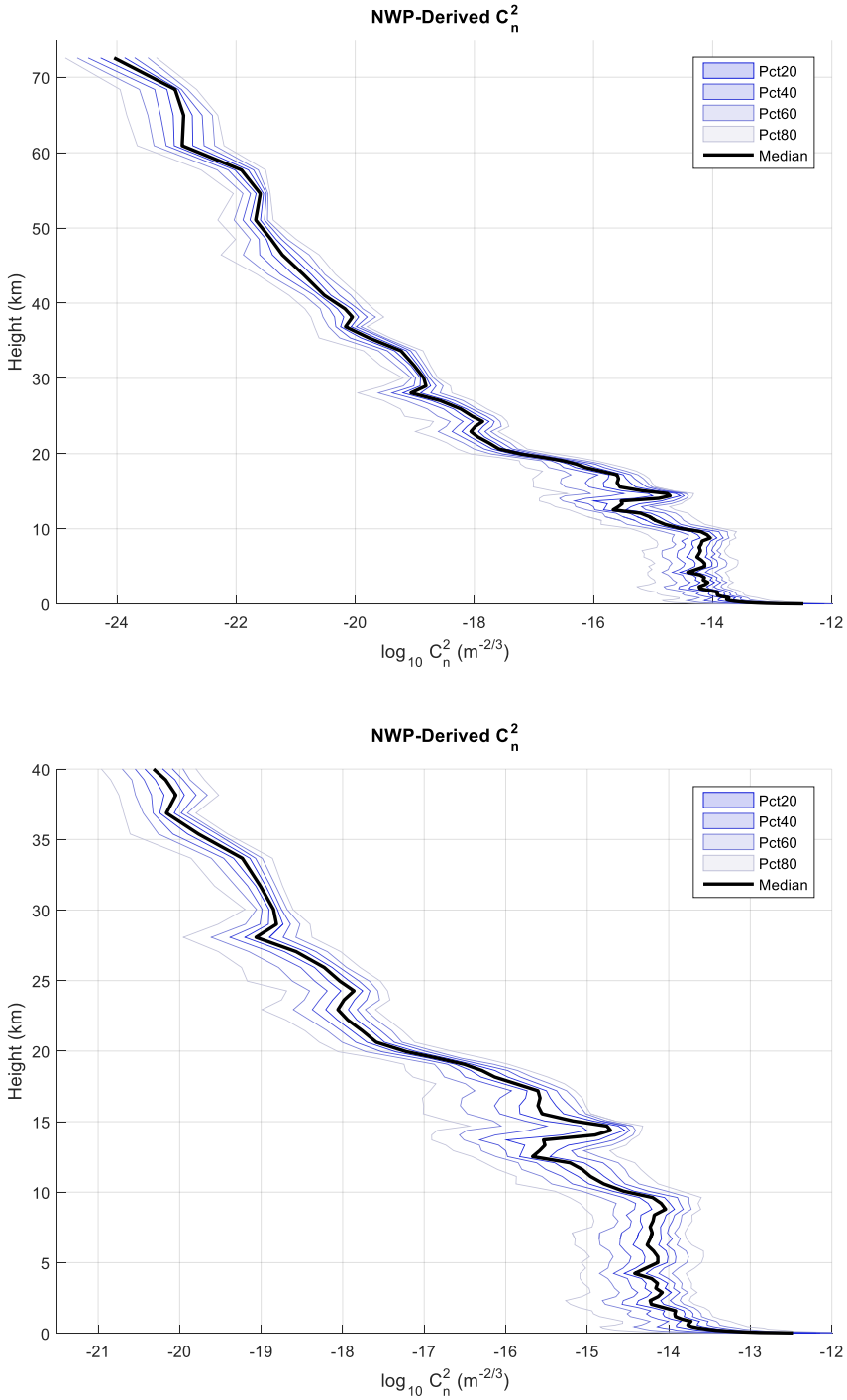

Figure 47. C_n^2 profiles for 38,400 grid points within a southeast US data set from the ECMWF ERA-20C re-analysis model for 1800 UTC, 1 Jun 2010. The top plot contains the entire vertical data set. The bottom plot is the bottom 40 km of the same data set to better show the spread in values around the median profile.

4.3.5 Modifications to C_n^2 Calculation Technique

4.3.5.1 Additional Wind Shear Terms in Richardson Number

Turbulent Kinetic Energy (TKE) is the kinetic energy associated with turbulent fluctuations of the atmosphere. A useful quantity in the study of turbulence and dynamic meteorology is the turbulent kinetic energy per unit mass [26]

$$\frac{TKE}{m} = \frac{1}{2}\left(\overline{u'^2} + \overline{v'^2} + \overline{w'^2}\right) . \tag{27}$$

The rate of change of *TKE/m* is determined by all sources or losses of turbulence within the volume of interest. These generation and loss terms are broken out in Equation (28):

$$\frac{\partial\left(TKE/m\right)}{\partial t} = Ad + M + B + Tr - \varepsilon \tag{28}$$

where *Ad* is the advection of turbulence by the mean wind, *M* is mechanical generation, and *B* is buoyant generation or consumption, *Tr* is transport by the turbulence itself, and ε is the term for viscous dissipation [26]. Of these terms, the two most important to this research are mechanical generation and buoyant generation or consumption [63]. One way to represent the balance of these is the gradient Richardson number in wind component form,

$$Ri = \left(\frac{g}{\bar{\theta}_v}\frac{\partial\bar{\theta}_v}{\partial z}\right) \Big/ \left[\left(\frac{\partial\bar{u}}{\partial z}\right)^2 + \left(\frac{\partial\bar{v}}{\partial z}\right)^2\right] . \tag{29}$$

The denominator of Equation (29) represents the mechanical generation of turbulence by wind shear, where the two terms represent the vertical shear in the two components of the horizontal wind, *u* and *v*. These terms are the only two wind shear terms available from a

single vertical wind profile, such as the set of wind measurements made by a rawinsonde. There are additional wind shear terms that could be responsible for generation of turbulence. The full, 3-dimensional mechanical generation term could be expressed as

$$\left(\frac{\partial \bar{u}}{\partial z}\right)^2 + \left(\frac{\partial \bar{v}}{\partial z}\right)^2 + \left(\frac{\partial \bar{u}}{\partial y}\right)^2 + \left(\frac{\partial \bar{v}}{\partial x}\right)^2 + \left(\frac{\partial \bar{w}}{\partial y}\right)^2 + \left(\frac{\partial \bar{w}}{\partial x}\right)^2 . \quad (30)$$

While the additional components are not available from a single rawinsonde measurement, the 3-D volumes of wind data studied in this research does provide the ability to calculate them. The wind field calculated from applying the AIRS windfinding technique to a series of neighboring AIRS fields-of-view provides the horizontal shear in the horizontal wind terms, $\frac{\partial \bar{u}}{\partial y}$ and $\frac{\partial \bar{v}}{\partial x}$. Vertical winds are not available from the AIRS windfinding technique, but they are available from NWP models.

3-D numerical weather models contain vertical wind components at each grid point by tracking convergence and divergence of the modeled horizontal winds. Starting from the surface model level, horizontal winds converging at a grid point force air up (because it cannot go into the ground) and diverging horizontal winds pull air down from above. Once all of the vertical motion is calculated for the lowest level, these vertical wind components specify the bottom boundary condition for the next higher level. Using the divergence and convergence of the horizontal winds at the second level, that level's vertical motion can be calculated, and so on throughout the 3-D grid.

As highlighted in Section 2.4.2, when compared to a hydrostatic model, a non-hydrostatic model more accurately represents vertical motion because in addition to vertical motion forced by convergence and divergence, buoyancy forces are modeled, and

the vertical accelerations calculated allow the winds to evolve in a more accurate manner from timestep to timestep. An approach taken in this research is to exploit the wind fields available from the non-hydrostatic ECMWF model to calculate a modified gradient Richardson number, using all six of these shear terms, to investigate the impact of the inclusion of the additional components.

First for a single sample data set, the original and modified gradient Richardson number profiles are calculated and compared. The effect of the additional components is very small. Figure 48 shows the difference between the original and modified Richardson number profiles for this test case.

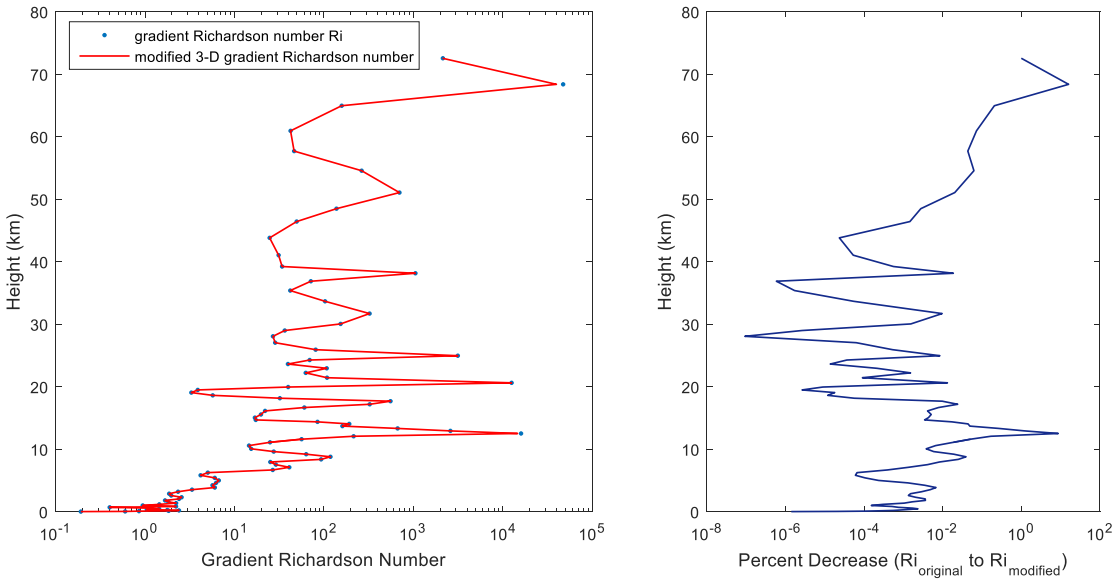

Figure 48. Comparison between gradient Richardson number, and modified 3-D, six shear term gradient Richardson number, which accounts for additional sources of mechanical generation of turbulence. This profile is calculated for a sample set of coordinates 40 km east of Springfield, MO, on 1 June 2010 at 0000 UTC. The two largest percent decreases for this example are 16% and 8%, and at all other heights the difference is less than 2%. The mean difference is 0.0032%.

The slight decrease in Richardson number leads to an increase in the ratio of K_H/K_M and a corresponding increase in C_n^2, but the increase would be slight (much less than 1%) throughout most of the vertical profile. The condition that would likely allow the modification to have a significant effect is a height where there is almost no change in the horizontal wind components from one level to the next. In Figure 49 the vertical profiles of the six shear components are plotted individually for the previous wind profile.

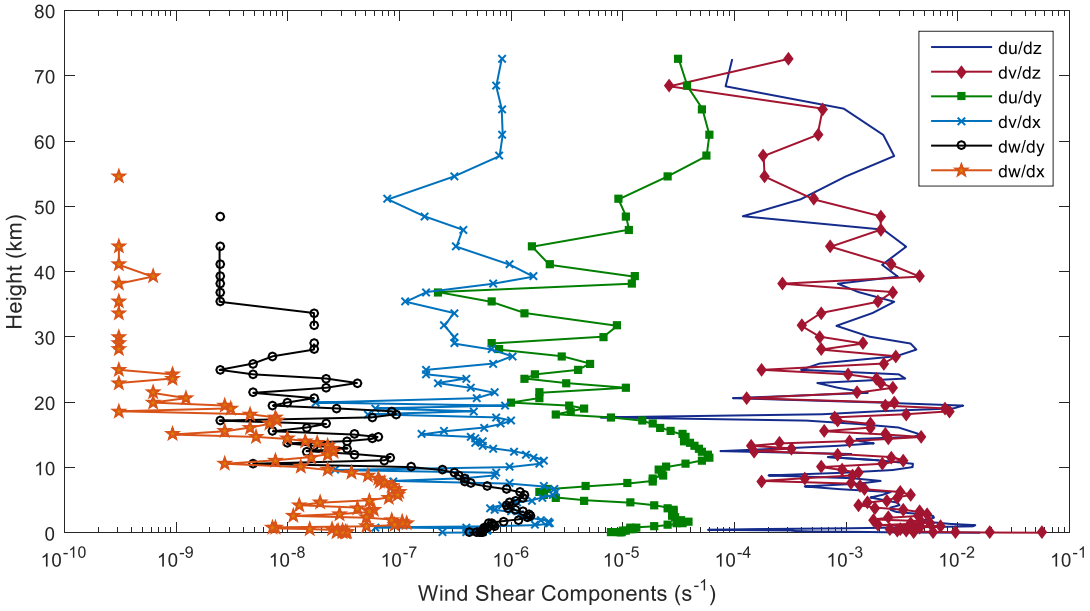

Figure 49. Six wind shear components that make up the mechanical generation of turbulence term in the modified 3-D gradient Richardson number. These profiles are calculated for the sample set of coordinates detailed in Figure 48.

Throughout much of the profile, the two shear terms included in the traditional gradient Richardson number dominate, typically 2-3 orders of magnitude larger than the components added by the modification. Figure 49 only represents the shear profiles for a single vertical path through the ECMWF data. To better understand the typical differences in magnitude between the six components, Figure 50 reproduces the previous plot, but for

the mean at each height from many profiles. A 160 x 240 grid was assembled from the 0.125 degree horizontal resolution ECMWF ERA-20C re-analysis data set. For each of these 38,400 grid points, the six shear components for the 91 vertical levels are calculated, and the profiles of the mean values of each component are plotted in Figure 50. These are not independent samples, as they are adjacent coordinates in the same data set, but the area is large enough to cover a range of different weather conditions, giving a good indication of where the mean magnitudes would settle out as additional data from different dates and times are included.

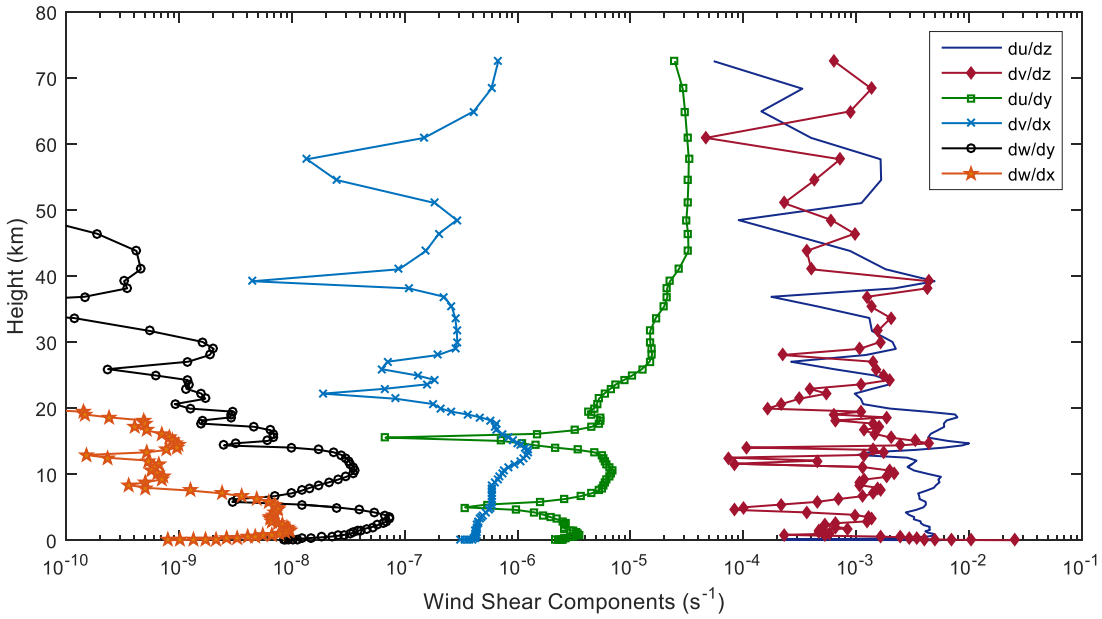

Figure 50. Average values for each of the six wind shear components that make up the mechanical generation of turbulence term in the modified 3-D gradient Richardson number. These profile averages are calculated for a 0.125 degree ECMWF ERA-20C grid between 20-40° N latitude and 65-95° W longitude, for 1 Jun 2010.

Comparison of the average profiles confirms the trend observed in Figure 49's single profile. The two shear components $\frac{\partial \bar{u}}{\partial z}$ and $\frac{\partial \bar{v}}{\partial z}$ are the most significant. Next are the horizontal shear in the horizontal wind terms $\frac{\partial \bar{u}}{\partial y}$ and $\frac{\partial \bar{v}}{\partial x}$, and because the vertical wind speeds are so much smaller than typical horizontal wind speeds, the components of shear in the vertical wind $\frac{\partial \bar{w}}{\partial y}$ and $\frac{\partial \bar{w}}{\partial x}$ are the least significant. To further minimize the impact of the four smaller shear terms, these gradients are each squared when included in the Richardson number calculation. While there is a physical basis for including these additional shear components, the accuracy and usefulness of the resulting C_n^2 values are not significantly improved when compared to the traditional approach of only considering the two dominant terms.

4.3.5.2 Problem with Tatarskii technique in a well-mixed layer

The traditional Tatarskii approach to calculating C_n^2 has an inherent problem in a well-mixed, neutrally-buoyant layer. C_T^2 is proportional to the local deviation from the dry adiabatic lapse rate. In a neutrally-buoyant layer where the actual lapse rate is very close to the dry adiabatic lapse rate, C_T^2, and therefore C_n^2, can be vanishingly small. This small value can underrepresent the strength of the turbulence present, as the assumption that all turbulence is related to local buoyant generation neglects additional sources. Turbulence can be generated by wind shears, leading to mixing which tends to push the lapse rate toward adiabatic so the presence of the turbulent mixing would not be reflected in the vertical temperature gradient. Also, turbulence may be advected into the area of interest

by the mean wind, where it may persist for a time even if the local vertical temperature gradient is not favorable to buoyant generation.

4.3.5.3 Inclusion of Pressure Gradient Term

The traditional Tatarskii approach used in this research (detailed in Section 3.3.1) derives C_n^2 from the temperature structure function C_T^2 and $\partial n/\partial T$ according to

$$C_n^2 = \left(\frac{\partial n}{\partial T}\right)^2 C_T^2, \tag{31}$$

which led to Equation (23). Tatarskii [35] makes the assumption that the turbulence is incompressible and that for optical wavelengths in dry air, gradients in refractive index depend only on the vertical potential temperature gradient. With this assumption removed, C_n^2 can be calculated by [64]

$$C_n^2 = a^2\left(\frac{K_H}{K_M}\right)L_0^{4/3}\left(\frac{\partial n}{\partial T}\frac{d\theta}{dz}+\frac{\partial n}{\partial p}\frac{dp'}{dz}+\frac{\partial n}{\partial e_v}\frac{de_v}{dz}\right)^2 . \tag{32}$$

The potential temperature gradient term, $\frac{\partial n}{\partial T}\frac{d\theta}{dz}$, is the dominant term and does lead to the largest contribution to the strength of the optical turbulence, but the additional terms are non-zero and in some cases are important to include. At optical wavelengths, the vapor pressure term $\frac{\partial n}{\partial e_v}\frac{de_v}{dz}$ is still small enough to be neglected in this research, but the pressure term $\frac{\partial n}{\partial P}\frac{dp'}{dz}$ can be an important source of optical turbulence, especially in well-mixed, neutrally-buoyant atmospheres where the potential temperature gradient term becomes very small. This pressure gradient term is discussed in detail in Section 4.3.5.5.

Data sets generated by high resolution, non-hydrostatic NWP models, such as the ECMWF ERA-20C atmospheric re-analysis model, allow comparison of the magnitude of each of the terms in Equation (32) for various atmospheric conditions.

4.3.5.4 Pressure Fluctuation Effect on Index of Refraction

The index of refraction of air depends on the local temperature, pressure, and humidity, so the basic equation of state is [22] [35]

$$N = N(T, p, q) \tag{33}$$

where N is related to the refractive index by $N = (n-1)\times 10^6$, T is temperature, p is pressure, and q is absolute humidity (mass of water/volume). Equation (33) is differentiated to yield

$$dN = \left(\frac{\partial N}{\partial T}\right)_{p,q} dT + \left(\frac{\partial N}{\partial p}\right)_{\mathrm{T},q} dp + \left(\frac{\partial N}{\partial q}\right)_{\mathrm{T,p}} dq\,. \tag{34}$$

To determine C_n^2, the local fluctuations in refractive index are approximated by

$$N' \approx \left(\frac{\partial N}{\partial T}\right)_{\bar{T},\bar{p},\bar{q}} \theta + \left(\frac{\partial N}{\partial p}\right)_{\bar{\mathrm{T}},\bar{p},\bar{q}} p' + \left(\frac{\partial N}{\partial q}\right)_{\bar{\mathrm{T}},\bar{p},\bar{q}} q' \tag{35}$$

where θ, p', and q' are the fluctuations about the mean value for each quantity.

As experimentally determined and published by Barrell and Sears in 1939 [65], Equation (36) provides a way to calculate the index of refraction of air as a function of temperature, pressure, and humidity.

$$(n-1)\times 10^{6} = \left[0.378125 + \frac{0.0021414}{\lambda^{2}} + \frac{0.00001794}{\lambda^{4}}\right] \times \frac{p\left[1+\left(1.049-0.157T\right)p\times 10^{-6}\right]}{1+T/273.16} - \left[0.0624 - \frac{0.000680}{\lambda^{2}}\right]\frac{f}{1+T/273.16} \tag{36}$$

The numerical coefficients in this equation are appropriate for their chosen units, where λ is wavelength in μm, p is pressure in mm Hg, T is temperature in degrees Celsius, and f is the partial pressure of water vapor in torr [65]. To simplify Equation (36) the two coefficients that define the wavelength dependent dispersion are redefined as $A(\lambda)$ and $B(\lambda)$ [22]:

$$A(\lambda) = 0.378125 + \frac{0.0021414}{\lambda^{2}} + \frac{0.00001794}{\lambda^{4}} \tag{37}$$

and

$$B(\lambda) = 0.0624 - \frac{0.000680}{\lambda^{2}}. \tag{38}$$

The values of these dispersion coefficients throughout the visible spectrum and into the near-IR are plotted in Figure 51. The effect of these dispersion coefficients across the visible and near IR spectrum is small [22], and in this research a characteristic wavelength near the middle of the range of wavelengths of interest will be selected and used throughout the refractive index calculations that follow. The wavelength selected is 0.5 μm, yielding the values $A(\lambda)$ = 0.387 and $B(\lambda)$ = 0.0597. It is noted that the error introduced by this choice is 1.35% at 300 nm, and 1.7% at 1.0 μm.

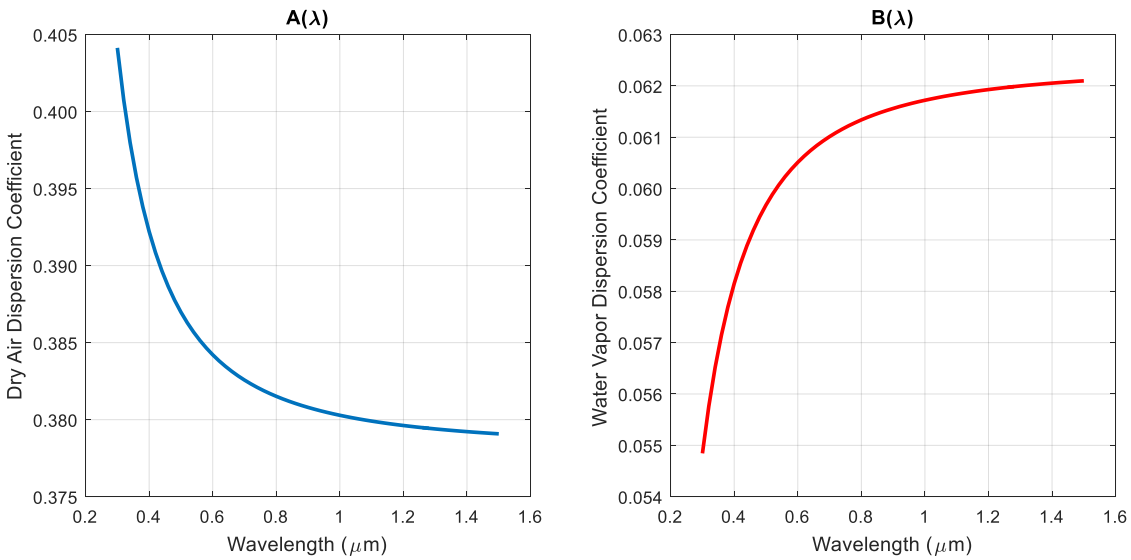

Figure 51. Barrell and Sears dispersion coefficients.

With the simplification by replacing the dispersion coefficients, Equation (36) becomes

$$(n-1)\times 10^6 = A(\lambda)\frac{p\left[1+\left(1.049-0.157T\right)p\times 10^{-6}\right]}{1+T/273.16} - B(\lambda)\frac{f}{1+T/273.16} \quad . \qquad (39)$$

Changing the numerical coefficients to be consistent with the units used throughout this document, replacing $(n-1)\times 10^6$ with N, and setting f to zero for dry air, Equation (39) is modified to become

$$N_{dry} = A(\lambda)\frac{204.9\,p}{T}\left[1+p\left(3.295\times 10^{-5}-1.178\times 10^{-7}T\right)\right] \qquad (40)$$

where p is now pressure in hPa and T is temperature in K. It is this form of the equation that is differentiated to determine the effect that the temperature and pressure fluctuations have on refractive index according to Equation (35). Again, the effect of humidity is small

at the wavelengths of interest, and the third term in Equation (35), $\left(\frac{\partial N}{\partial Q}\right)_{\overline{T},\overline{P},\overline{Q}} q'$, is neglected in this research.

The partial derivatives of Equation (40) with respect to temperature and pressure are

$$\left(\frac{\partial N_{dry}}{\partial T}\right)_{\overline{T},\overline{P}} = -A(\lambda)\frac{p\left(204.9+6.751\times10^{-3}p\right)}{T^2} \tag{41}$$

and

$$\left(\frac{\partial N_{dry}}{\partial p}\right)_{\overline{T},\overline{P}} = A(\lambda)\frac{\left[204.9+p\left(0.01350-4.824\times10^{-5}T\right)\right]}{T} \ . \tag{42}$$

4.3.5.5 C_n^2 Values Calculated using Temperature and Pressure Gradients

The partial derivatives are entered into this dry air expression for C_n^2

$$C_n^2 = a^2\left(\frac{K_H}{K_M}\right)L_0^{4/3}\left(\frac{\partial n}{\partial T}\frac{d\theta}{dz}+\frac{\partial n}{\partial P}\frac{dp'}{dz}\right)^2 \ . \tag{43}$$

The term $\frac{\partial n}{\partial T}$ is the change in refractive index with change in temperature and $\frac{\partial n}{\partial p}$ is the change in refractive index with change in pressure, both determined by differentiating the Barrell and Sears equation, as shown in Equations (41) and (42). The term $\frac{d\theta}{dz}$ is the deviation from dry adiabatic, as previously calculated for the traditional Tatarskii approach. The interesting term is the local vertical pressure fluctuation term, $\frac{dp'}{dz}$. Here p' is not atmospheric pressure, but the fluctuation in atmospheric pressure. The approach taken in this research is to follow the train of thought that if the atmosphere were at all times, and

at all locations, in hydrostatic balance there would be no local vertical pressure fluctuations. Furthermore, if the pressure at one location were perturbed from hydrostatic balance, it would be a transient event as the surrounding atmosphere would immediately apply a restoring force to move back toward hydrostatic balance. This is an argument for stating that the magnitude of any deviations from hydrostatic equilibrium are of the same order as the transient pressure fluctuations. Therefore, if there were a way to identify at one instant, at one location, the local pressure deviation from hydrostatic equilibrium, that deviation could be used to estimate the magnitude of the temporal pressure fluctuation at that location, dp'. Therefore $\frac{dp'}{dz}$ is the vertical pressure gradient deviation from hydrostatic.

A non-hydrostatic model, like the ECMWF, makes this possible. The technique begins with bottom level of the model and working up one level at a time from there, using a rearranged hypsometric equation:

$$p_2 = \frac{p_1}{e^{\left(g\Delta z / R_d \overline{T_v}\right)}} \ . \tag{44}$$

At model level 2, this equation is used to calculate what the pressure would be if hydrostatic forces were in balance, using the model's pressure at level 1, the difference between the heights of levels 1 and 2, and the mean virtual temperature in the layer between levels 1 and 2. The difference between what the pressure would be (if exactly in hydrostatic balance) and what the pressure at level 2 actually is in the model defines the local pressure deviation dp'. This pressure deviation is divided by the vertical distance between the levels to approximate $\frac{dp'}{dz}$. This process is repeated for each higher grid point in the model

to calculate a pressure deviation value for every level in the model except the surface level. These values for $\frac{dp'}{dz}$ are used in Equation (43) to calculate C_n^2 values that are based on the temperature deviations from adiabatic and the pressure deviations from hydrostatic.

To illustrate the effect of this modification, a vertical ECMWF ERA-20C profile is selected because it contains a layer between 600 and 800 m where the lapse rate very nearly matches the dry adiabatic lapse rate. In Figure 52 the contributions to C_n^2 from the temperature and pressure gradient terms are plotted individually, along with the resulting C_n^2 including both terms.

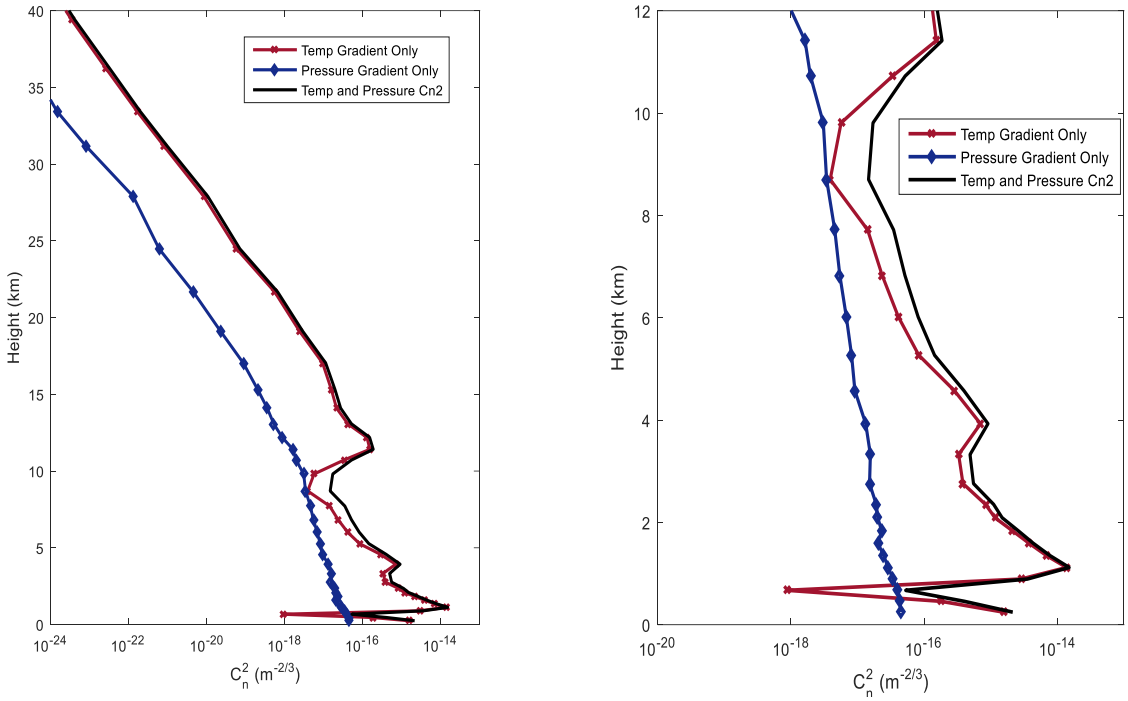

Figure 52. Comparison of contributions to C_n^2 by temperature and pressure gradient terms. The right plot is the lowest 12 km of the same data as the left plot, expanded to show detail. This Dayton, OH profile is for 10 Nov, 2010, 0000 UTC.

In Figure 52, the pressure gradient term is much smaller than the temperature gradient term (by about two orders of magnitude) throughout most of the profile, but at the

heights where the temperature gradient term drops sharply due to the near constant potential temperature, the pressure gradient term becomes significant. To analyze the improvement this modification has on derived C_n^2 values, a series of comparisons are made to scintillometer-based measurements made by Dr. Mikhail Vorontsov and his research team at the University of Dayton [66]. These measurements are from November and December of 2010, along a 7 km path between the University of Dayton and the Veterans Affairs Medical Center, shown in Figure 53.

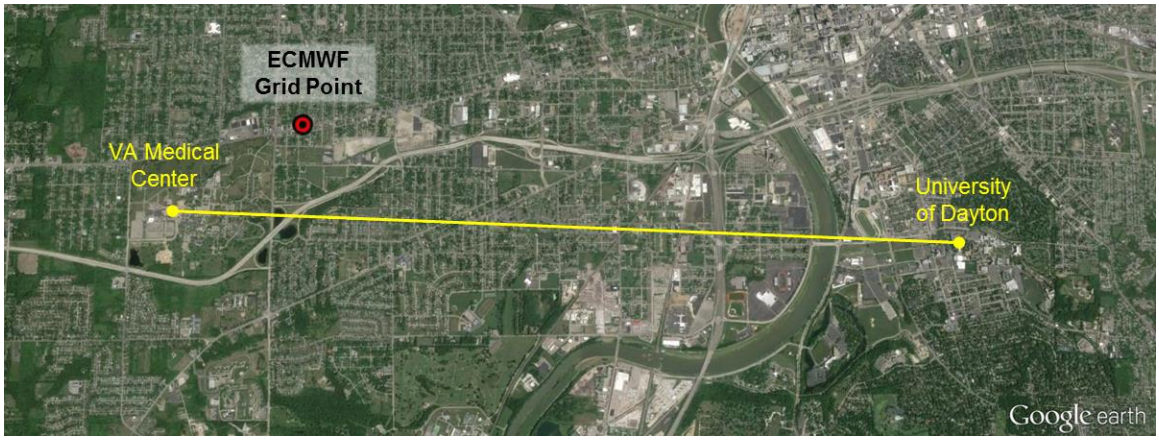

Figure 53. Depiction of the 7 km University of Dayton scintillometer path and nearest ECMWF grid point. Map data and imagery: Google Earth, Landsat [66] [67].

These two months of University of Dayton scintillometer measurements are during the time period covered by the ECMWF ERA-20C data. For these C_n^2 calculations, the values of K_H/K_M =1 and L_0= 10m are used since they are more appropriate values for the boundary layer, and the constant K_H/K_M prevents any problems being introduced by the gradient Richardson number calculation. The ECMWF data are for a single grid point near the scintillometer path, just north of the path toward the VA Medical Center end of the path.

The C_n^2 values (temperature gradient only, and combined temperature and pressure gradients) calculated for the lowest ECMWF level at the grid point shown in Figure 53 are plotted in Figure 54, along with the UD scintillometer measured C_n^2 values along the 7 km path. These data represent all available scintillometer data for this 5-week time period, with gaps when no data were collected. Figure 55 and Figure 56 show two 6-day subsets of these data.

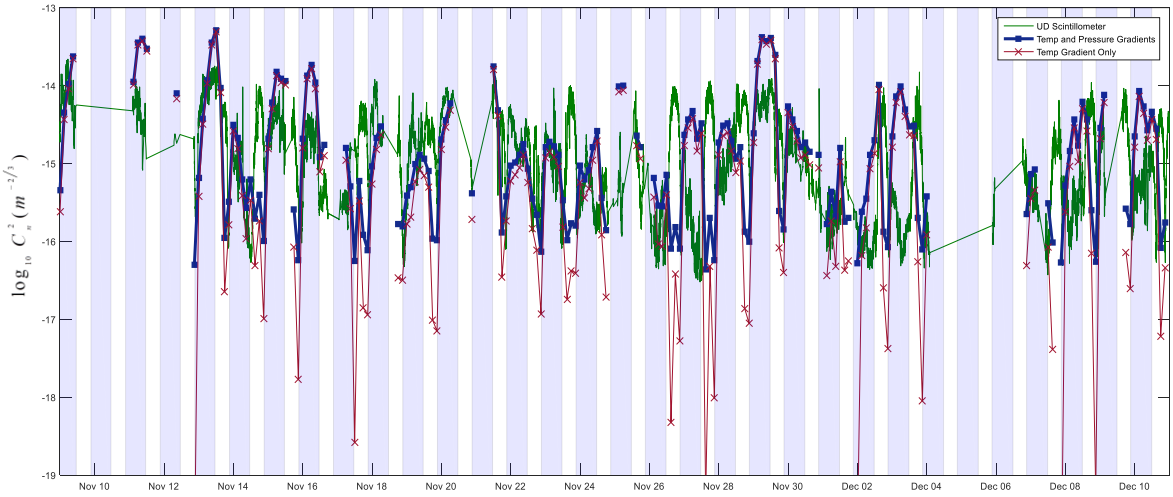

Figure 54. Analysis of modified and unmodified C_n^2 derivation technique, each compared to UD scintillometer data collected by the University of Dayton during Nov-Dec 2010. For all three of these plots, the dates/times on the horizontal axis are UTC, and the shaded regions identify the time periods between local sunset and sunrise [66].

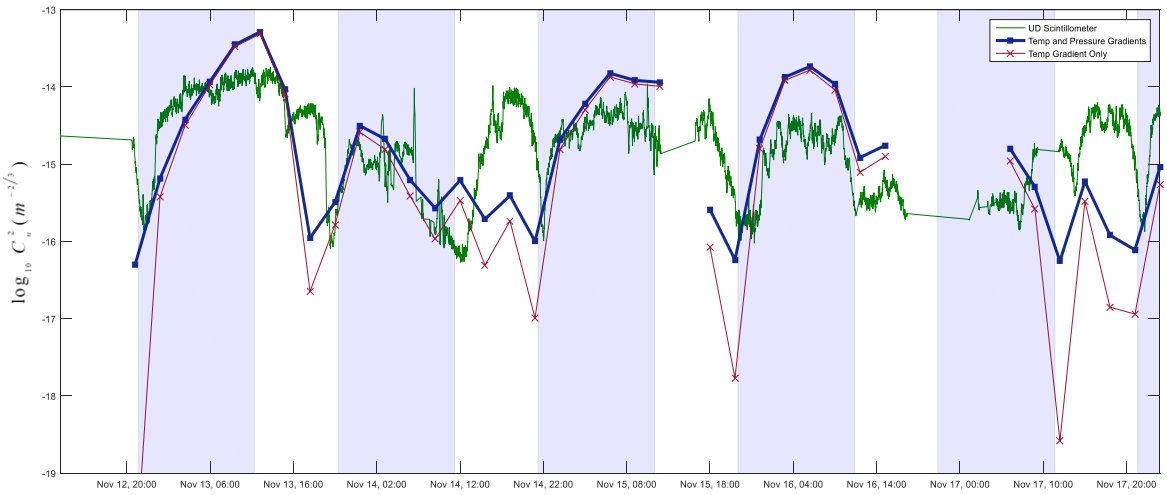

Figure 55. Subset of Figure 54 data. 11 Nov 2010-17 Nov 2010 [66].

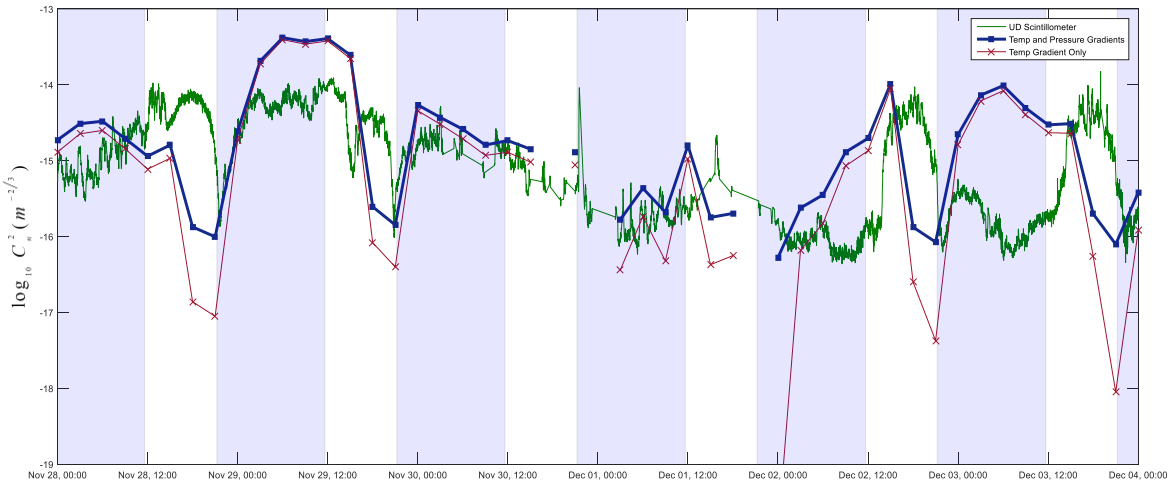

Figure 56. Subset of Figure 54 data. 28 Nov 2010-4 Dec 2010 [66].

Throughout this range of dates, it is observed that when the lower atmosphere is well-mixed and neutrally buoyant, the temperature-only C_n^2 value drops by one to three orders of magnitude. At these low values, the pressure term has the potential to become the dominant term, leading to C_n^2 values closer those measured by the scintillometer. For the 33 days that scintillometer data were available, the RMS error for the unmodified

technique result is 0.71 orders of magnitude. With the pressure gradient term added, the RMS error is reduced to 0.65 orders of magnitude. The most significant improvement is seen during the quiescent periods in turbulent activity, conditions that are of particular interest to directed energy research efforts as their favorable conditions are often targeted for system testing and evaluation.

5 Conclusions

5.1 Summary of Findings

This research develops a method to exploit AIRS temperature retrievals to obtain wind fields and other atmospheric parameters (C_T^2 and C_n^2) of importance for the directed energy community. AIRS data takes advantage of the 4.3 μm carbon dioxide absorption feature to obtain excellent vertical resolution and accurate temperature retrieval. These techniques are not documented elsewhere, and can be applied to temperature soundings from other satellite-based infrared sounders.

One of the conclusions of this research is that, even though the AIRS windfinding technique has some proven skill to determine trends in wind speed and direction, it does not match the performance of modern NWP models. The volume of sounder temperatures from several satellite-based instruments is assimilated into the weather models, so the AIRS-based technique does not start with any information not included in the NWP models. The reason the NWP winds are more reliable is that NWP models are updated with more than just temperature values. Many additional sources of data, such as surface and upper-air observations, are also assimilated by the model, the dynamics of which eliminate many of the measurement errors from individual observational data points. After the comparisons detailed in this document it is clear that, even when remotely-sensed observations of the needed atmospheric parameter are available, NWP data should be utilized.

An application for which the AIRS windfinding technique is still well-suited is generating first guess winds at altitudes where NWP model data is not available or easily

accessed and no observations are available. It is currently difficult (or expensive) to access forecast data for the upper stratosphere, and since rocketsonde campaigns are infrequent, direct wind observations are rare. The AIRS windfinding technique, building wind profiles upward from the top pressure level of GFS or another NWP model, can provide some insight into wind speed and direction at altitudes where no other information is easily accessible.

The modification to the gradient Richardson number is not found to be of significant benefit to estimating C_n^2. In atmospheric layers where the horizontal wind components do not change between the bottom of the layer to the top, the inclusion of the additional wind shear components leads to a decrease in Richardson number and a corresponding increase in calculated C_n^2. The additional terms are very small, however, and the modification does not lead to a meaningful increase in the final C_n^2 value.

A significant technique developed in this research is the process to exploit a non-hydrostatic model, using local deviations from hydrostatic equilibrium to estimate the size of the transient pressure fluctuations. This demonstrates the capability to calculate and make use of a source term for optical turbulence that had been previously neglected. The small, but measurable increase in C_n^2 becomes significant in a well-mixed layer, where the traditional Tatarskii approach is likely to underestimate the strength of the optical turbulence.

5.2 Impact on Directed Energy Research Community

The atmospheric characterization techniques and the refinement of existing index of refraction structure function derivation methods can benefit the directed energy research

community. Enhanced knowledge about the strength of optical turbulence and extinction along a path of interest will improve our understanding of how a directed energy system or sensor will perform. The ability to better characterize the atmosphere will allow better, more accurate tests of systems as they are being developed and evaluated. Through the combination of near real-time satellite measurements and numerical weather model output, the research paves the way to a critical predictive capability, arming a user with more knowledge of how an operational system would perform for a specified path and time. These techniques can allow an operator a passive means to know the expected effective range of a laser weapon system, as determined by the current state of the atmosphere. Optical turbulence and extinction vary by path, so the ability to compare system performance for several engagement geometries would provide a tactical advantage and enable an informed decision prior to system employment.

The ability to passively obtain expected bounds of C_n^2 values for a path of interest would be valuable to an operational high-altitude HEL system. Actual characterization of the atmosphere at the time of the engagement would be performed by a laser beacon, but prior to the engagement, the AIRS/NWP-based characterization could inform decisions on best altitude for engagement or optimum engagement order for multiple targets. In the possible case where it is necessary to engage a target that is beyond the range of the beacon (but not beyond the range of the HEL) the AIRS/NWP-derived C_n^2 values would provide characterization of the strength of the optical turbulence for the far end of the path, providing an estimate of required dwell time for the engagement.

5.3 Recommendations for Future Work

The techniques developed to generate standard C_n^2 models for polar and tropical maritime locations could be used to create additional, more specialized standard models. By narrowing the geographic region, or selecting only soundings during a specific time of day or time of year, the envelope of expected C_n^2 values for a more narrow set of conditions could be established. The use of AIRS data limits time of day investigation to the overpass time (around 0130 and 1330 local time) but by using NWP model data, standard models could be created for any time of day (limited only by the temporal resolution of the model selected).

Another interesting area for future research with the AIRS data is an extension of the temperature accuracy study detailed in Section 4.1. For the two Alaska locations, the study found that the temperature error above 100 hPa was greater for cloud-free soundings than soundings with high cloud fraction. This may indicate a problem in the AIRS algorithm detecting high-altitude clouds. Additional study, including more locations, and making comparison to cloud cover observations from other sources could determine the source of this unexpected result.

There are opportunities to continue the pressure gradient research, coupling it with AFIT's on-going radar research. The ability to directly measure pressure gradients with the radar while simultaneously calculating the pressure fluctuations from a non-hydrostatic weather model would allow calculation of the group of coefficients $\left(a^2 K_H \middle/ K_M \; L_0^{4/3} \right)$ which prove very difficult to derive from easily measured parameters. This would require access to current non-hydrostatic model data, and a good choice would be the WRF model.

Running a customized WRF model would allow control of the model resolution and better study of the effects of changes to initialization data, but will come with the computational expense of running a high-resolution, non-hydrostatic NWP model and the corresponding lengthy processing times.

6 References

[1] D. C. Meier, "Application of Satellite-Derived Wind Profiles to Joint Precision Airdrop Systems (JPADS) Operations," Air Force Institute of Technology, Wright-Patterson Air Force Base, OH, M.S. Thesis 2010.

[2] G. W. Petty, *A First Course in Atmospheric Radiation*. Madison, WI: Sun Dog Publishing, 2006.

[3] S. Q. Kidder and T. H. VonderHaar, *Satellite Meteorology*. San Diego, CA: Academic Press, Inc., 1995.

[4] L. D. Kaplan, M. T. Chahine, J. Susskind, and J. E. Searl, "Spectral band passes for a high precision satellite sounder," *Applied Optics*, vol. 16, no. 2, pp. 322-325, February 1977.

[5] G. W. Petty, *A First Course in Atmospheric Thermodynamics*. Madison, WI: Sundog Publishing, 2008.

[6] C. Crevoisier, A. Chedin, and N. A. Scott, "AIRS channel selection for CO2 and other trace-gas retrievals," *Q. J. R. Meteorol. Soc.*, vol. 129, pp. 2719-2740, 2003.

[7] S. Cho. (2002, February) GES-DISC - Advanced Microwave Sounding Unit-A (AMSU-A) Instrument Guide. [Online]. http://disc.sci.gsfc.nasa.gov/AIRS/documentation/amsu_instrument_guide.shtml

[8] Y. I. Won, "README Document for AIRS Level-2 Version 5 Support Products," NASA GES DISC, 2008.

[9] S. Cho. (2002, May) GES-DISC Atmospheric Infrared Sounder Instruments. [Online]. http://disc.sci.gsfc.nasa.gov/AIRS/additional/instruments.shtml

[10] NASA. (2015, November) Aqua Project Science, Formation Flying-The A-Train. [Online]. http://aqua.nasa.gov/content/formation-flying

[11] NASA. (2012, March) MODIS Image Gallery. [Online]. http://modis.gsfc.nasa.gov/gallery/index.php#

[12] Land Processes Distributed Active Archive Center. (April, 2014) LP DAAC, MODIS Overview. [Online]. https://lpdaac.usgs.gov/dataset_discovery/modis

[13] P. Lynch and R. Gutro. (2009, August) Hurricanes/Tropical Cyclones, Latest Storm Images and Data from NASA. [Online]. http://www.nasa.gov/mission_pages/hurricanes/archives/2009/h2009_Bill.html

[14] Environmental Modeling Center. (2015, October) NOAA National Weather Service Environmental Modeling Center. [Online]. http://www.emc.ncep.noaa.gov/GFS/doc.php

[15] E. Kalnay, *Atmospheric Modeling, Data Assimilation and Predictability*. New York, NY: Cambridge University Press, 2003.

[16] S. Saarinen, "ODB User Guide," ECMWF, Reading, U.K., Integrated Forecast System Documentation 2004.

[17] L. Xu, S. Raman, and R. V. Madala, "A review of non-hydrostatic numerical models for the atmosphere," in *Proc. of the first world congr. on nonlinear analysts '92, vol. IV*, Tampa, FL, 1992, pp. 3595-3609.

[18] A. Tunick, "The Refractive Index Structure Parameter / Atmospheric Optical Turbulence Model: Cn2," Army Research Lab, Adelphi, MD, April 1998.

[19] D. L. Fried, "Statistics of a Geometric Representation of Wavefront Distortion," *Journal of the Optical Society of America*, vol. 55, no. 11, pp. 1427-1435, 1965.

[20] N. Ageorges and C. Dainty, *Laser Guide Star Adaptive Optics for Astronomy*. Dordrecht, The Netherlands: Kluwer Academic Publishers, 2000.

[21] J. C. Wyngaard, *Turbulence in the Atmosphere*. New York, NY: Cambridge University Press, 2010.

[22] C. A. Friehe, J. C. La Rue, F. H. Champagne, C. H. Gibson, and G. F. Dreyer, "Effects of temperature and humidity fluctuations on the optical refractive index in the marine boundary layer," *Journal of the Optical Society of America*, vol. 65, no. 12, pp. 1502-1511, 1975.

[23] L. C. Andrews, *Field Guide to Atmospheric Optics*. Bellingham, WA: SPIE-The International Society for Optical Engineering, 2004.

[24] S. Raghavan, *Radar Meteorology*. Dordrecht, The Netherlands: Kluwer Academic Publishers, 2003.

[25] A. Tunick, N. Tikhonov, M. Vorontsov, and G. Carhart, "Characterization of optical turbulence (Cn2) data measured at the ARL A_LOT facility," Army Research Lab, Adelphi, MD, 2005.

[26] J. M. Wallace and P. V. Hobbs, *Atmospheric Science: An Introductory Survey*, 2nd ed. Burlington, MA, MA: Elsevier Academic Press, 2006.

[27] J. A. Dutton, *The Ceaseless Wind*. New York, NY: Dover Publications, Inc., 1986.

[28] G. P. Perram, S. J. Cusumano, R. L. Hengehold, and S. T. Fiorino, *An Introduction to Laser Weapon Systems*. Albuquerque, NM: The Directed Energy Professional Society, 2010.

[29] J. T. Houghton, *The Physics of Atmospheres*, 2nd ed. Cambridge, United Kingdom: Cambridge University Press, 1986.

[30] D. H. Tofsted, S. G. O'Brien, and G. T. Vaucher, "An Atmospheric Turbulence Profile Model for Use in Army Wargaming Applications I," White Sands Missile Range, NM, 2006.

[31] R. K. Tyson and B. W. Frazier, *Field Guide to Adaptive Optics*, 2nd ed. Bellingham, WA: SPIE-The International Society for Optical Engineering, 2012.

[32] G. C. Valley and S. M. Wandzura, "Spatial correlation of phase-expansion coefficients for propagation through atmospheric turbulence ," *Journal of the Optical Society of America*, vol. 69, no. 5, pp. 712-717, 1979.

[33] R. R. Beland, "Propagation through atmospheric optical turbulence," in *The Infrared and Electro-Optical Systems Handbook, vol 2*. Bellingham, WA: SPIE Optical Engineering Press, 1993.

[34] R. Avila and J. Vernin, "Mechanism of Formation of Atmospheric Turbulence Relevant for Optical Astronomy," in *Interstellar Turbulence*. Cambridge, U.K.: Cambridge University Press, 1999, pp. 5-11.

[35] V. I. Tatarskii, *The Effects of the Turbulent Atmosphere on Wave Propagation*. Springfield, VA: U.S. Department of Commerce, 1971.

[36] AIRS Science Team/Joao Texeira (2013), Aqua AIRS Level 2 Support Retrieval (AIRS+AMSU), version 006, Greenbelt, MD, USA:NASA Goddard Earth Science Data and Information Services Center (GES DISC), Accessed 1 Jan 2014-15 Nov 2015, doi:10.5067/AQUA/AIRS/DA.

[37] Office of the Federal Coordinator for Meteorological Services and Supporting Research (US). (1997) Federal Meteorological Handbook No. 3: Rawinsonde and Pibal Observations. FCMH3-1997. [Online]. http://www.ofcm.gov/fmh3/fmh3.htm

[38] College of Engineering, Department of Atmospheric Science University of Wyoming. (2015) Worldwide Radiosonde Soundings of the Atmosphere. [Online]. http://weather.uwyo.edu/upperair/sounding.html

[39] MathWorks, Curve Fitting Toolbox User's Guide, Release R2015b, 2015.

[40] H. B. Bluestein, *Synoptic-Dynamic Meteorology in Midlatitudes, vol. 1*. New York, NY: Oxford University Press, 1992.

[41] D. C. Meier and S. T. Fiorino, "Correlated Satellite-derived Turbulence, Clouds & Aerosol Data," in *Propagation Through and Characterization of Distributed Volume Turbulence*, Seattle, WA, 2014.

[42] D. C. Meier and S. T. Fiorino, "Comparison of Index of Refraction Structure Function (Cn2) Profiles Derived from Polar-orbiting Satellite Data and Numerical Weather Prediction Models," in *Propagation Through and Characterization of Distributed Volume Turbulence*, Arlington, VA, 2015.

[43] T. E. VanZandt, J. L. Green, K. S. Gage, and W. L. Clark, "Vertical profiles of refractifity turbulence structure constant: Comparison of observations by the Sunset Radar with a new theoretical model," *Radio Science*, vol. 13, no. 5, pp. 819-829, Sep-Oct 1978.

[44] R. J. Alliss and B. D. Felton, "Numerical Simulations of Optical Turbulence Using an Advanced Atmospheric Prediction Model: Implications for Adaptive Optics Design," in *Proceedings of the Advanced Maui Optical and Space Surveillance Technologies Conference*, Wailea, Maui, HI, 2014.

[45] R. J. Alliss and B. D. Felton, "Validation of Optical Turbulence Simulations from a Numerical Weather Prediction Model in Support of Adaptive Optics Design," in *Proceedings of the Advanced Maui Optical and Space Surveillance Technologies Conference*, Wailea, Maui, HI, 2009.

[46] M. G. Sterenborg, "Determining the refractive index structure constant using high-resolution radiosonde data," *Journal of the Atmospheric Science*, vol. 61, 2004.

[47] G. d'Auria, F. S. Marzano, and U. Merlo, "Model for estimating the refractive-index structure constant in clear-air intermittent turbulence," *Applied Optics*, vol. 32, no. 15, pp. 2674-2680, May 1993.

[48] H. A. Panofsky and J. A. Dutton, *Atmospheric Turbulence: Models and Methods for Engineering Applications*. New York, NY: John Wiley & Sons, 1984.

[49] H. B. Bluestein, *Synoptic-Dynamic Meteorology in Midlatitudes, vol. 2*. New York, NY: Oxford University Press, 1993.

[50] L. C. Roberts and L. W. Bradford, "Improved models of upper-level wind for," *Optics Express*, vol. 19, no. 2, pp. 820-837, January 2011.

[51] J. O. Kondo, O. Kanechika, and N. Yasuda, "Heat and momentum transfers under strong stability in the atmospheric surface layer," *Journal Atmos. Sci.*, vol. 35, pp. 1012-1021, 1978.

[52] M. J. Post, "Effects of the earth's atmosphere on a spaceborne IR Doppler wind-sensing system ," *Applied Optics*, vol. 18, no. 15, pp. 2645-2653, 1979.

[53] NOAA. (2014, January) Geostationary Satellite Server. [Online]. http://www.goes.noaa.gov

[54] B. H. Kahn et al., "The Atmospheric Infrared Sounder version 6 cloud products," *Atmospheric Chemistry and Physics*, vol. 14, pp. 399-426, 2014.

[55] S. Platnick et al. (2015) MODIS Atmosphere L2 Cloud Product (06_L2). [Online]. http://dx.doi.org/10.5067/MODIS/MOD06_L2.006

[56] J. Susskind, J. Blaisdell, P. Rosenkranz, and E. T. Olsen, "AIRS/AMSU/HSB Version 5 Level 2 Quality Control and Error Estimation," Jet Propulsion Laboratory (JPL), California Institute of Technology, Pasadena, CA, 2010.

[57] S. M. Bourne, U. S. Bhatt, J. Zhang, and R. Thoman, "Surface-based temperature inversions in Alaska from a climate perspective," *Atmospheric Research*, vol. 95, pp. 353-366, February 2010.

[58] E. M. Manning, "AIRS Version 6.1 Processing Files Description," Jet Propulsion Laboratory (JPL), California Institute of Technology, Pasadena, CA, 2015.

[59] J. Susskind, C. D. Barnet, and J. M. Blaisdell, "Retrieval of atmospheric and surface parameters from AIRS/AMSU/HSB data in the presence of clouds," *IEEE Transactions on Geoscience and Remote Sensing*, vol. 41, no. 2, pp. 390-409, Feb 2003.

[60] A. E. Cole, "Review of Data and Models of the Middle Atmosphere," in *Proceedings of the Open Meetings of the Working Groups on Physical Sciences of the Twenty-first Plemary Meeting of COSPAR*, Innsbruck, Austria, 1978, pp. 153-164.

[61] B. Morrison, Final ROBIN Sphere Data Results from 20150608, 2015.

[62] G. M. Anderson, "Development of a Standard Maritime Cn2 Profile Using Satellite Measurements," Air Force Institute of Technology, Wright-Patterson Air Force Base, OH, M.S. Thesis 2014.

[63] J. R. Holton and G. J. Hakin, *An Introduction to Dynamic Meteorology*, 5th ed. Waltham, MA: Elsevier-Academic Press, 2013.

[64] L. R. Burchett, S. T. Fiorino, and D. C. Meier, "Method for Estimating Optical Cn2 From Weather Radar and Numerical Weather Prediction," *unpublished*, 2015.

[65] H. Barrell and J. E. Sears, "The Refraction and Dispersion of Air for the Visible Spectrum," *Philosophical Transactions of the Royal Society*, vol. 238, no. 786, pp. 1-64, February 1939.

[66] M. T. Velluet et al., "Turbulence characterization and image processing data sets from a NATO RTO SET 165 trial in Dayton (OH)," in *Proc. SPIE, Vol. 8380, Atmospheric Propagation IX*, Baltimore, MD, 2012.

[67] Google Earth, Dayton Map and Imagery, 13 Jun 2014, Accessed: 21 Nov 2015.

REPORT DOCUMENTATION PAGE

Form Approved
OMB No. 0704–0188

1. REPORT DATE (DD–MM–YYYY)	2. REPORT TYPE	3. DATES COVERED *(From — To)*
24-12-2015	Doctoral Dissertation	August 2012 – December 2015

4. TITLE AND SUBTITLE

Operational Exploitation of Satellite-Based Sounding Data and Numerical Weather Prediction Models for Directed Energy Applications

5a. CONTRACT NUMBER

5b. GRANT NUMBER

5c. PROGRAM ELEMENT NUMBER

6. AUTHOR(S)

Meier, David C., Lieutenant Colonel, USAF

5d. PROJECT NUMBER

5e. TASK NUMBER

5f. WORK UNIT NUMBER

7. PERFORMING ORGANIZATION NAME(S) AND ADDRESS(ES)
Air Force Institute of Technology
Graduate School of
2950 Hobson Way
WPAFB OH 45433-7765

8. PERFORMING ORGANIZATION REPORT NUMBER

AFIT-ENP-DS-15-D-009

9. SPONSORING / MONITORING AGENCY NAME(S) AND ADDRESS(ES)

MZA Associates Corporation
2021 Girard Blvd. SE – Suite 150
Albuquerque, NM 87106

Air Force Office of Scientific Research
Deep Turbulence MURI
875 N. Randolph, Ste.325
Arlington Virginia, 22203

10. SPONSOR/MONITOR'S ACRONYM(S)
MZA, AFOSR

11. SPONSOR/MONITOR'S REPORT NUMBER(S)

12. DISTRIBUTION / AVAILABILITY STATEMENT

DISTRIBUTION STATEMENT A:
APPROVED FOR PUBLIC RELEASE; DISTRIBUTION UNLIMITED.

13. SUPPLEMENTARY NOTES

14. ABSTRACT

The wealth of available scientific data collected by the modern constellation of meteorological satellites can be exploited in new and innovative ways, with direct benefit to directed energy applications. The Atmospheric Infrared Sounder (AIRS) provides accurate, geolocated temperature data, which are used as the starting point for the derivation of atmospheric parameters critical to prediction of sensor or directed energy system performance. Twenty-four hour data coverage is achieved by extending the atmospheric characterization between satellite observations using Numerical Weather Prediction (NWP) models. A technique is developed to derive wind profiles using AIRS temperature data and the accuracy of these winds is evaluated. These winds are not found to be as accurate as the winds available from modern NWP models, but their usefulness is demonstrated for the stratosphere and lower mesosphere where NWP model data are not readily available. Techniques to derive optical turbulence strength, as modeled by index of the refraction structure function C_n^2, are applied to integrated meteorological satellite data and NWP data. The existing technique, which bases the derivation of C_n^2 for optical wavelengths on vertical atmospheric temperature gradients, is improved by including additional wind shear components and local pressure gradient deviations from the traditionally assumed hydrostatic balance.

15. SUBJECT TERMS

Atmospheric Optical Turbulence, Atmospheric IR Sounder (AIRS) , Satellite-Based Temperature Retrieval, Satellite-Based Windfinding

16. SECURITY CLASSIFICATION OF:			17. LIMITATION OF ABSTRACT	18. NUMBER OF PAGES	19a. NAME OF RESPONSIBLE PERSON
a. REPORT	b. ABSTRACT	c. THIS PAGE			Dr. Steven T. Fiorino, AFIT/ENP
U	U	U	UU	122	19b. TELEPHONE NUMBER (Include Area Code) (937) 255-3636 x4506 steven.fiorino@afit.edu